

NANOMETER TIP-BASED ULTRAFAST ELECTRON SOURCES:
EMISSION PROCESSES AND DIRECT PULSE
CHARACTERIZATION TECHNIQUES

A DISSERTATION
SUBMITTED TO THE DEPARTMENT OF PHYSICS
AND THE COMMITTEE ON GRADUATE STUDIES
OF STANFORD UNIVERSITY
IN PARTIAL FULFILLMENT OF THE REQUIREMENTS
FOR THE DEGREE OF
DOCTOR OF PHILOSOPHY

Catherine Kealhofer
August 2013

Abstract

Since the first half of the 20th century, metal tips ending in hemispheres with a radius of curvature of hundreds of nanometers or less have been used as stochastic field emission electron sources because the small radius of curvature allows the application of very strong electric fields to the tip apex. These tips are high brightness electron sources because they have very small virtual source sizes-typically smaller than the tip radius. In this work, field emission tips are operated as pulsed electron sources triggered by a femtosecond laser; thus, the temporal profile of the electron emission is determined by the laser pulse, but the source size is much smaller than the diffraction-limited laser focal spot. Furthermore, due to optical field enhancement at the tip apex, it is possible to get into the strong field regime, where electron emission happens on a time-scale shorter than the optical period. Possible applications of these sources include ultrafast x-ray tubes, improved ultrafast time-resolved electron microscopy and diffraction, injectors for laser accelerators, and quantum optics experiments with time-tagged electrons.

The first part of this thesis presents a unified picture of the ultrafast laser-induced emission processes (photo-assisted field emission, multiphoton emission and strong field photoemission, thermally enhanced field emission) and experimental characterization of these processes. The second half describes two ongoing experiments that seek to directly characterize the electron pulses in time. The first is based on streaking the bias field of the tip, which maps the electron emission time onto electron kinetic energy. The second is a cross-correlator for electrons and photons, where an electron absorbs a photon in the near field created by scattering light from a nanostructure.

These experiments will constitute not only the first direct measurement of the electron pulse duration in this system but will also point the way towards new techniques for manipulating ultrafast electron pulses with optical and microwave fields.

Acknowledgments

Many thanks to my advisor, Mark, for taking me as a student and giving me the opportunity to work on what was at the time an almost brand new project in the group. He has been supportive and patient, and his phenomenal creativity and physical intuition have been a driving force behind the project. Again and again, Mark had an idea that Seth and I resisted but which ultimately turned out to be right. Mark pushed us to go further and seek not only to understand phenomena, but also to ask what we could do with this understanding—build a device that couldn’t be made before? measure something that couldn’t be measured before?

My committee, Jo Stohr, Leo Hollberg, and especially my reading committee members, Phil Bucksbaum, and Bob Byer, have provided valuable feedback.

Several talented physicists have worked with me on this project and taught me most of what I know. Peter Hommelhoff started the original experiment, building its first few incarnations and figuring out how to apply the Keldysh theory to electron emission from sharp tips. More than anyone else I know, he brings a huge sense of fun to doing science, and it is infectious for the people working with him. Seth Foreman practically lived in the lab during his post-doc, and his physicist-fu ranges from ultrafast laser alignment to articulating simple and clear explanations of physical phenomena. He has taught me many technical things, but maybe the most important lesson was that of persistence. After all this time, I think we can call ourselves friends. I also reserve the right in perpetuity to ask him questions about phase noise. Gunnar Skulason can do just about anything in the lab, including FIB nanostructures with me looking anxiously over his shoulder. A generous and patient teacher, he is way too nice for his own good—while I was writing my thesis, he held down the fort at work *and*

brought over delicious dinners. Brannon Klopfer worked on the terahertz sampling experiment and made many improvements to our experiment-control “code”, in the process teaching me the appropriate way to comment said code. His child-like wonder at all things physics-, fourier-transform-, and lab-related bodes well for the QEM project. Christoph Kohstall, Thomas Juffmann, and Josh Francis make up the rest of the QEM team, and even though they have only been here a short time, I have benefited from their insights.

I am indebted to the entire Kasevich group—including Hui Chun Chien, Mike Minar, Nick Cizek, Olaf Mandel, David Berryrieser, Patrick Medley, Geert Vrijzen, Igor Teper, Nils Engelsen, Onur Hosten, Raj Krishnakumar, Jason Hogan, Dave Johnson, Susannah Dickerson, Alex Sugarbaker, Tim Kovachy, Sheng-Wey Chiow, Kaspar Sakmann, Sean Roy—for technical advice and moral support and good fun. Sha Zhang put up with all of our pcard paperwork, and the amazing Ping Feng is something like lab-super-mom (if only she had been running the experiment!). The people in the Physics Shop—Karlheinz Merkle, Scott Barton, Matt Chuck, John Kirk, and Mehmet Solyali—have always been willing to take time to explain something or lend a tool.

Eons ago, I did a few problems sets with Edward Wu, Mike Minar, Dave Press, Nick Cizek, Derek Mackay, and Susan Clark, many of whom are still close friends and who undoubtedly influenced how I think about physics. I’ve managed to live with a bunch of great people while in grad school, which I’m convinced is the best thing to do with your friends. Lynne Rosen, Esther Kim, Laurie Dean, George Burkhard (and, by extension, Liz Schemm), Ari Bensimhon, Graham Anderson, Joe and Christina Cackler, Yuko Amizaki, Paul DiCapua, Davin Anderson, Dan Golden and Rachel Nosheny, Anthony Miller, Yeong Dae Kwon, and Dmitri Pavlichin have supplied friendship and occasional technical advice, not to mention roomie bike rides, triathlons, StarCraft spectating, climbing, backpacking, and really good food. I’ve almost borrowed lab equipment from Mike Armen on several occasions, and I have actually borrowed all kinds of obscure lab equipment and old ortec manuals from Rick Pam. The friendship of Annique Witdoeckt, Jessica Wichser, George Burkhard, John Saunders, Leo Goldmakher, Forrest Collman, Ed Wu, Anthony Miller, and Gunnar

Skulason has sustained me over the harder parts of grad school. The intellectual talent of my brothers David, Robert, and Marc continuously inspires me, and I am grateful for their faith in me and their technical advice (as well as donated desk space and last-minute proofreading of this thesis). I can't say enough how my parents' unflagging support (once they got used to the idea of me studying physics) has mattered—I'm sure I wouldn't have made it this far without their generosity, open-mindedness, and love of learning.

I owe a big debt to Grethe Clarke, my middle school physics teacher, who introduced me to special relativity. I learned from her that (a) you can describe the universe with math, (b) doing so can lead to surprising insights and predictions, and (c) some fun people called experimentalists go out and see if these things are true.

Contents

Abstract	iv
Acknowledgments	vi
1 Introduction	1
1.1 Ultrafast electron sources	1
1.2 Figures of merit	2
1.2.1 Emittance	4
1.2.2 Brightness	5
1.2.3 Transverse coherence length	7
1.2.4 Quantum limits to beam brightness and emittance	8
1.2.5 Pulse duration	10
1.3 Outline	12
2 Electron emission mechanisms	14
2.1 Thermionic emission and field emission	14
2.1.1 The surface potential barrier	17
2.1.2 Derivation of the Fowler-Nordheim equation	22
2.1.3 The Richardson-Dushman equation for thermionic emission . .	25
2.1.4 Thermal-assisted field emission	26
2.2 Laser-triggered electron emission	27
2.2.1 Overview of ultrafast emission processes	28
2.3 Summary	31

3	Laser-induced emission processes	33
3.1	Laser-induced electron emission from field emission tips in the non-adiabatic tunneling regime	33
3.1.1	Experimental setup	35
3.1.2	Interferometric autocorrelation measured with the tip	36
3.1.3	Power non-linearity as a function of bias voltage	39
3.1.4	Carrier-envelope phase dependence	43
3.1.5	Numerical integration of TDSE	46
3.2	Laser-triggered emission from Hafnium Carbide tips: multiphoton emission vs. thermally-assisted field emission	48
3.2.1	Characterization of emission processes	50
3.2.2	Model of heating and thermal conduction in the tip	56
3.2.3	Estimated transient thermal emission from HfC	66
4	Energy-domain streaking	68
4.1	Proof-of-concept: ultrafast oscilloscope and energy-domain streaking without an RF cavity	69
4.1.1	Experimental setup	69
4.1.2	Oscilloscope measurements	71
4.1.3	Streaking measurements	75
4.2	The route to improving time-resolution of the streaking experiments .	77
4.2.1	Technical limits to time-resolution	79
4.2.2	Energy streaking of electrons emitted in a microwave cavity .	81
4.2.3	Simulated electron trajectories	87
4.3	Summary	93
5	Laser-electron cross-correlation	95
5.1	Electron energy gain spectroscopy	96
5.2	Experimental design	97
5.2.1	Apparatus	97
5.2.2	Optical fields in the nanohole target	100
5.2.3	Probability of photon absorption	102

5.2.4	Pulse duration at the interaction region	105
5.2.5	Signal to noise considerations	105
A	Annealing procedure	107
B	Probability of photon absorption by an electron	109
B.1	Monochromatic field	109
B.2	Time-domain expression	111
B.2.1	Classical energy increase	112
	Bibliography	113

List of Tables

1.1	Typical experimental parameters for ultrafast electron sources	3
1.2	Figures of merit for ultrafast electron sources	9
3.1	Materials properties used for modeling	58
3.2	Fit parameters for HfC complex permittivity	60
4.1	Dimensions of apertures in microwave cavity	85
4.2	Sensitivity of resonance frequency to the cavity dimensions	85
5.1	Contributions to pulse broadening at the target	104
A.1	Anneal procedure	107

List of Figures

2.1	Surface barrier potential	18
2.2	Surface dipoles	20
2.3	I - V curves for thermal-assisted field emission	27
2.4	Electron emission processes	32
3.1	Definition of carrier-envelope phase	34
3.2	Laser spectrum and transform-limited pulse	35
3.3	Interferometric autocorrelation traces	38
3.4	Peak-to-baseline ratio of autocorrelation traces vs. bias field	40
3.5	Polarization dependence of emission current (1)	42
3.6	Polarization dependence (2)	43
3.7	Simulated optical field enhancement	44
3.8	f - $2f$ interferometer	45
3.9	1D Schrödinger model	47
3.10	Simulated CE phase modulation	49
3.11	I_{laser} and I_{2f}	51
3.12	Multiphoton and thermal-assisted field emission from HfC	52
3.13	Emission pattern for multiphoton and thermal or DC field emission .	54
3.14	Influence of polarization and mis-alignment on laser-induced emission from HfC	55
3.15	SEM images of HfC tip	56
3.16	Geometry of tip in finite-element simulation	57
3.17	Drude-Lorentz fit to HfC reflectivity	60
3.18	Finite element model of optical fields near tip.	61

3.19	Electromagnetic model results for HfC, W, Au	62
3.20	Two-temperature model (Hafnium carbide).	64
3.21	Two-temperature model (Tungsten and Gold).	65
3.22	Scaling of transient TFE vs. multiphoton emission.	67
4.1	Experimental setup.	70
4.2	Non-linear transmission line oscilloscope trace	72
4.3	Frequency response of the tip	73
4.4	9.28 GHz oscilloscope trace	74
4.5	Energy-domain streaking	76
4.6	Simulated effect of energy streaking on the measured spectrum	78
4.7	Phase-noise measurement setup.	82
4.8	Jitter spectral density for amplified 9 GHz repetition rate harmonic applied to tip.	83
4.9	Re-entrant cavity dimensions	84
4.10	Re-entrant microwave cavity	86
4.11	Photograph of microwave cavity	86
4.12	Measured cavity resonance	87
4.13	Field profiles used for determining the electron trajectories	88
4.14	Simulated energy-domain streaking with a microwave cavity	89
4.15	Ensemble of electron trajectories in the microwave cavity	91
4.16	Energy modulation vs. time	92
4.17	Maximum streaking slope vs. DC tip voltage	93
5.1	Electron-optical cross correlation setup.	98
5.2	SEM image of nanohole target.	99
5.3	Nanohole as waveguide.	100
5.4	Transverse profiles of nanohole modes	102
5.5	Interaction length for electron energy gain	103
5.6	Probability of photon absorption vs. time delay	104
5.7	Energy resolution and signal-to-noise.	106

Chapter 1

Introduction

1.1 Ultrafast electron sources

In 1982, Mourou and Williamson built an electron diffraction apparatus using 100 picosecond electron pulses [1]. Their electron source was a modified streak tube, with an aluminum photocathode. This—a pulsed electron source synchronized with a laser source that could act as a pump—led to the field of time-resolved electron diffraction, with modern experiments using 100–500 fs electron pulses generated from flat photocathodes [2, 3]. At almost the same time, starting in the 70’s, Lee and coworkers had investigated using lasers to generate electrons from field emission tips [4, 5]. Using cw lasers, they observed thermally-induced emission processes and photofield emission. Our group [6] and another group [7] independently had the idea of combining ultrafast lasers with field emission tips and studying ultrafast electron emission from these sources.

Field-emitter based ultrafast electron sources have unique properties that could enable a wide range of new technologies. Field-emitters have small source sizes, which leads to greater transverse coherence and lower emittance than planar cathode sources. For this reason, they are used as electron sources in high-resolution transmission electron microscopes and in electron interferometers [8]. Due to optical field enhancement, they may be operated in the non-adiabatic tunnel regime [9, 10], which results in sub-optical cycle electron emission. Besides their potential as sources for

ultrafast electron diffraction and microscopy, the small source size of ultrafast laser-triggered field-emitters makes them attractive sources for dielectric laser acceleration [11] and ultrafast microfocus x-ray tubes [12]. Their expected large transverse coherence length opens up the possibility of ultrafast time-resolved electron interferometry [13] and holography. A femtosecond electron source with high transverse coherence could make it easier to implement electron beamsplitters from standing light waves; the requisite high laser intensities [14] could be reached using ultrafast optical pulses because the electron source can be synchronized with the beamsplitter.

1.2 Figures of merit

To make a formal comparison between the tip-based ultrafast electron source and planar photocathode-based sources, it is helpful to consider some figures of merit. The improved emittance, brightness and transverse coherence figures for tip-based sources follow because the source size is smaller than for planar photocathodes.

Three interrelated figures of merit are used in electron optics to quantify beam quality. The emittance of a beam is a measure of how parallel the trajectories in a collimated beam are. The smaller the emittance, the more parallel a collimated beam, the less blurring of diffraction spots will occur in a diffraction measurement, and the smaller a spot can be produced by focusing the beam with a lens of a given focal length. The brightness is proportional to the current in the beam divided by the emittance; since in practice, diffraction and imaging experiments must use finite integration times, the amount of current available in a high quality beam determines what signal to noise can reasonably be achieved. Finally, the coherence of the beam is related to the visibility of fringes that would be obtained by performing an interference experiment between two different parts of the beam and is evidently important for interferometers, but can also lead to enhanced signal to noise in diffraction experiments.¹

¹The definitions of emittance, brightness, and coherence used here are based on references [17] and [18]; the first reference gives a practical introduction to emittance and brightness of electron beams, and the second gives a phase-space treatment for synchrotron radiation, including a discussion of coherence.

Table 1.1: Typical experimental parameters for ultrafast electron sources

Parameter	Flat photocathode [2]	Field-emitter photocathode
Effective source size	150 μm	1-2 nm
Pulse duration	100 fs	1-10 fs [9]
Beam size at sample	100 μm	
Beam energy	300 keV	
Initial energy spread	0.2 eV	0.2-0.3 eV (DC emission)
Number of electrons per pulse	$10^4 - 10^5$	$10^3 - 10^4$ [15, 16]

Field emission tip sources have temporal advantages over flat photocathodes as well. Optical field enhancement enables multiphoton emission from tips in a sub-optical-cycle emission regime [19], and the high DC fields at the surface of a tip rapidly accelerate the electrons from rest, mitigating kinematic broadening of the electron pulse [20].

1.2.1 Emittance

Consider a beam propagating in the z -direction. Assuming that there are no correlations between the x and y co-ordinates in the particle distribution, we can define the root-mean-square (RMS) emittance in the x -coordinate as

$$\epsilon_x = 4 \left[(x - \langle x \rangle)^2 (x' - \langle x' \rangle)^2 - \langle (x - \langle x \rangle)(x' - \langle x' \rangle) \rangle^2 \right]^{1/2} \quad (1.1)$$

$$= 4 \left[\sigma_x^2 \sigma_{x'}^2 - \langle (x - \langle x \rangle)(x' - \langle x' \rangle) \rangle^2 \right]^{1/2}, \quad (1.2)$$

where x' is dx/dz (the angle the electron trajectory makes relative to the z axis in the xz plane), and σ_x and $\sigma_{x'}$ are the RMS widths of the x and x' distributions. Thus, if there are no correlations between the angle of the particles and the position in the beam the emittance is simply

$$\epsilon_x = 4\sigma_x\sigma_{x'}. \quad (1.3)$$

We expect this kind of situation at, for example, a photocathode, where each point in the extended source emits with the same angular distribution, set by properties of the emission process. In photocathodes used for ultrafast electron diffraction, it is important to generate a beam with a small energy spread. To accomplish this, the photon energy must be tuned to match the photocathode work function, resulting in energy spreads of 0.2-0.3 eV [2]. On the other hand, if a collimated beam is acted on by an ideal lens, its net RMS angular spread will increase significantly, but this is offset by the correlation between position and angle of the particles' trajectories.

If we imagine accelerating a collimated beam in the z direction, even though its transverse momentum spread remains constant, $\sigma_{x'}$ must decrease trivially because

the momentum in the z direction is increasing. The same argument holds for converging and diverging beams. The volume of the particle distribution in phase space is conserved, however. It is useful to define the normalized emittance, which will be conserved in ideal optical systems and could be thought of as an intrinsic property of the source:

$$\epsilon_{n,x} = \beta\gamma\epsilon_x \simeq \beta\epsilon_x \text{ (for non-relativistic beams).} \quad (1.4)$$

Here, $\beta = v/c$ and $\gamma = 1/\sqrt{1 - \beta^2}$, with v the electron speed.

From equation 1.3, it is evident that decreasing the size of the extended source decreases the normalized emittance of the source. In this regard, field-emitter-based sources represent an improvement of orders of magnitude over flat photocathode sources. For a tip with a radius of curvature of ~ 100 nm, the emission area has a radius of at most tens of nanometers. The effective source size is even smaller than this, because electrons initially follow the field lines at the surface of the tip, so that if one backtracks the trajectories of the electrons, they form a virtual crossover at a location inside the tip. The radius of the effective emission area for a hemispherical field-emitter of radius r is

$$r_{\text{eff}} \approx \left[\frac{\hbar r}{2\sqrt{2m\phi}} \right]^{1/2}, \quad (1.5)$$

where ϕ is the work function of the tip and m is the mass of the electron [21]. For a 100 nm radius tip with a work function of 4.5 eV, the effective source size is $r_{\text{eff}} = 2$ nm.

In the case of flat photocathodes, the source size is fundamentally limited by the diffraction limit for focusing the ultrafast triggering pulse onto the cathode, which should be on the order of hundreds of nanometers. In practice, experimenters are limited by the quantum efficiency of the photocathode and must use source sizes on the order of 100 μm in order to obtain enough electrons per pulse [22].

1.2.2 Brightness

The above fact raises the question of whether laser-triggered field-emission tips can generate pulses with enough electrons to be used in diffraction experiments. One

perspective is that to observe interesting chemical and physical transformations in solid-state systems, the pump pulse must be so intense that the sample is destroyed, though not before useful structural information at short time delays has been observed [2]. In this case, the electron probe pulse must have enough electrons to permit single-shot imaging (or, perhaps, imaging in several shots, by moving to a new position on the sample); in practice, the number of electrons required to build up a useful diffraction pattern is roughly 10^6 for this type of experiment [23]. For diffraction targets in a molecular beam, this is a lesser issue, as the sample is continuously replaced. Somewhat surprisingly, the field-emitter based electron sources are not that far off planar cathode sources in terms of numbers of electrons per pulse, with a few thousand electrons emitted from 50-100 nm tips with only (~ 10 fs) laser excitation [15, 16]. This reaches towards the lower end of the values given in Table 1.1 for state-of-the-art ultrafast electron diffraction sources, and it is not clear that this number is a physical upper bound to how many electrons could be produced. Furthermore, as the tip-based sources have a much larger degree of transverse coherence than planar sources, one would expect an enhancement of the signal-to-noise of the diffraction pattern. There may be applications where it is desirable to trade numbers of electrons per pulse for greater coherence.

This trade-off is evident in a comparison of the brightness of the two sources (Table 1.2). The source brightness can be thought of as the current density emitted by the source divided by the solid angle of emission² and is proportional to the total current, I , in the beam divided by its transverse emittance:

$$B = \frac{I}{\pi^2 \epsilon_x \epsilon_y}. \quad (1.7)$$

²Another intuitive way to think about brightness: if we focus the beam with an ideal lens, the maximum current density in the focus (neglecting space charge) is approximately

$$j_{\max} \approx \frac{B}{f\#} \quad (1.6)$$

[17].

The normalized brightness, defined in terms of normalized emittance, permits comparison of beams at different energies:

$$B_n = \frac{I}{\pi^2 \epsilon_{n,x} \epsilon_{n,y}} = \frac{B}{(\beta\gamma)^2}. \quad (1.8)$$

Table 1.2 lists the peak brightness of the sources.

Based on the preceding discussion, two additional quantities of interest are the peak brightness multiplied by the pulse duration (note that the field emission source is still superior to the planar source), and the average brightness (this latter quantity multiplied by the repetition rate). The repetition rate of the field-emitter based sources discussed is ~ 100 MHz, higher than is typically used for ultrafast electron diffraction, but the limiting factor in these experiments might be the repetition rate of the pump rather than that of the probe.

It should be noted that there are some discrepancies in the literature between quoted values of the brightness for cold field-emitters (for example, compare Refs. [24] and [25]). A possible cause is emittance growth from statistical Coulomb fluctuations [26]. It should be possible to test this by comparing emittance measurements for laser-induced emission with large numbers of electrons per pulse versus less than one electron per pulse.

1.2.3 Transverse coherence length

In a diffraction experiment, a rule of thumb is that the coherence length of the beam should exceed three times the lattice parameter [2]. To image large objects, such as proteins, with a typical size scale of nanometers would require larger coherence lengths than are obtained with flat photocathode sources. The normalized mutual coherence function for electrons in the beam at a position z is given by³

$$\gamma(\mathbf{x}_1, \mathbf{x}_2, t_1, t_2) = \frac{\langle \psi(\mathbf{x}_1, t_1) \psi^*(\mathbf{x}_2, t_2) \rangle}{\sqrt{\langle |\psi(\mathbf{x}_1, t_1)|^2 \rangle \langle |\psi(\mathbf{x}_2, t_2)|^2 \rangle}}, \quad (1.9)$$

³By using a single-electron wavefunction, we implicitly assume that there are no important effects involving correlations between the electrons, i.e. the beam degeneracy is low.

where $\mathbf{x} = (x, y)$ is the transverse position, $\psi(\mathbf{x}, t)$ is the wavefunction of an individual electron and the brackets indicate an ensemble average. The mutual coherence function quantifies the visibility of fringes that would be obtained in a hypothetical interference experiment between two points \mathbf{x}_1 and \mathbf{x}_2 . Assuming the system is cylindrically symmetric, the transverse coherence length at some reference location and time (x_0, t_0) is

$$\xi_T(x_0, t_0) = \int_{-\infty}^{\infty} dx |\gamma(x_0 - (x/2), x_0 + (x/2), t_0, t_0)|^2 \quad (1.10)$$

The van Cittert-Zernike theorem relates the transverse coherence length at a distance l from an incoherent source to size of the source, r_{eff} :

$$\xi_T = \frac{\lambda l}{\pi r_{\text{eff}}}, \quad (1.11)$$

where λ is the wavelength of the electron. Using a biprism interferometer, Cho et al. [27] directly measure ξ_T at a fixed distance away from a DC tungsten field-emitter and infer effective source sizes of less than 1 nm for 50-100 nm tips at room temperature. They attribute this in part to the fact that the coherence length of the electrons in the metal is 5-10 nm, on the order of the emission area. This suggests that in the limit of single atom tips (or even ultra-sharp tips with emission spots of radius $\lesssim 5$ nm it should be possible to generate fully coherent electron beams. However, so far, there have not been any experimental studies of the coherence of ultrafast laser-induced electron emission from such tips.

1.2.4 Quantum limits to beam brightness and emittance

The uncertainty principle puts limits on the emittance of a source: for a single electron state, we must have

$$\Delta x \Delta p \geq \frac{\hbar}{2}, \quad (1.12)$$

which results in a normalized emittance of

$$\epsilon_n = \frac{4 \Delta x \Delta p}{mc} \geq \frac{2\hbar}{mc}. \quad (1.13)$$

Table 1.2: Figures of merit for ultrafast electron sources

Figure of merit	Flat photocathode [2]	Field-emitter photocathode
Transverse normalized emittance	$0.3 \pi \text{ mm mrad}$	$\lesssim 10^{-2} \pi \text{ mm mrad}$ [28, 24]
Peak brightness	$2 \times 10^7 \text{ A}/(\text{cm}^2 \text{ sr})$	$5 \times 10^9 \text{ A}/(\text{cm}^2 \text{ sr})$, assuming a 10 fs pulse
Transverse coherence length at diffraction target	$\sim 2 \text{ nm}$	$\sim 5 \mu\text{m}$ for geometry in [2] with $r_{\text{eff}} = 2 \text{ nm}$

In the z -direction, applying this criterion in the rest frame of the electron and then returning to the lab frame, we get

$$\Delta t \Delta E \geq \frac{\hbar}{2}. \quad (1.14)$$

Using the Pauli exclusion principle, for a pulse of length Δt and two electrons (with different spin states) occupying the minimum emittance phase-space “cell”, the maximum normalized brightness that can be obtained for any beam is

$$B_{n,\max} = \frac{8\pi e \Delta E (mc)^2}{h^3}. \quad (1.15)$$

The beam degeneracy, δ , is defined as the ratio of the normalized beam brightness to the maximum normalized brightness allowed by quantum mechanics,

$$\delta = \frac{B_n}{B_{n,\max}}. \quad (1.16)$$

For an energy spread of 0.3 eV, $B_{n,\max} \approx 5 \times 10^{15}$ A/(cm² sr). Inspection of Table 1.2 shows that the typical degeneracy for the sources discussed is less than 10^{-5} ; in fact, even for extremely high brightness sources such as carbon nanotube and single-atom field-emitters, the degeneracy is usually 10^{-4} – 10^{-3} , and efforts to achieve quantum degeneracy are based on more exotic electron sources, such as optical excitation of cold atomic gases, or field emission from stable single molecules adsorbed on sharp tips [29].

1.2.5 Pulse duration

The inherent energy spread of an electron source transforms to a temporal spread after the pulses have propagated some distance, since electrons with different energies travel at different speeds. The difference in speeds becomes smaller as the electron energy increases. For this reason, the ultrafast planar photocathode sources are operated with the maximum practical field strengths (~ 10 MV/m for DC fields) [22, 2], with proposals to use RF cavities to achieve higher accelerating gradients [2]. The field

strength at the surface of a sharp tip, however, can be as large as a few GV/m in typical ultrafast operation, limited, of course, by the onset of DC tunneling.

The approximate pulse broadening for electrons accelerated from rest in a constant field is

$$\Delta t \approx \frac{\sqrt{2m\Delta E_0}}{eF}, \quad \text{≡} \quad (1.17)$$

with ΔE_0 the initial energy spread, F the field, and e and m the charge and mass of the electron, respectively. With $F \sim 10$ MV/m and $\Delta E_0 \sim 0.3$ eV, the pulse broadens to 180 fs. So, even if shorter triggering laser pulses were used with flat photocathodes, it would not improve the time resolution. By contrast, even though the field of a field emission tip decreases rapidly away from the tip, it is strongest for the electrons' initial acceleration, where it can have the largest effect in mitigating broadening. Simulating electron propagation in one of our experimental configurations (4000 V applied between a 500 nm tip and an electrode 1.5 mm away), an initial energy spread of 0.3 V leads to only 3.3 fs of broadening as the electrons reach the electrode.

The possibility of suppressing kinematic broadening in this way makes it interesting to consider shorter emission times than those used with flat photocathodes—the shortest demonstrated pulse thus far is shorter than 500 attoseconds, triggered by a 6 fs pulse at 800 nm [10]. This was achieved at high laser intensity in the non-adiabatic tunnel regime. At lower intensity, in the multiphoton regime, the initial electron pulse duration should be comparable to the duration of the exciting laser pulse.

There is considerable interest in generating sub-100 fs pulses with enough electrons for single-shot imaging, which is being pursued via pulse compression in microwave cavities [30, 31, 32] but so far is limited by jitter in the synchronization of the pulse with the microwaves [2, 32]. Baum and Zewail have proposed exploiting the ponderomotive force of a standing light wave for pulse compression down to the attosecond level [33]. Dielectric laser accelerator structures could provide means to compress pulses on these time-scales as well [34]. All of these techniques must be optimized to work at electron energies below about 300 keV to maintain large enough probe wavelength and scattering cross section [30].

Significant work remains to be done on propagation dynamics of ultrafast pulses

with high charge derived from field emission tips. Due to the initially very high spatial localization, the aspect ratio of the electron packet is qualitatively different from those derived from flat photocathode sources [35].

1.3 Outline

The chapters that follow focus on two major questions: (1) what are the mechanisms responsible for laser-induced electron emission from field emission tips? and (2) can we develop practical methods for direct, in-situ measurement of electron pulse durations?

Chapter 2 provides a brief theoretical background for DC and laser-induced emission processes from nanometer tips. Chapter 3 describes studies of ultrafast laser-induced emission from tungsten and hafnium carbide field emission tips. In both cases, we observe multiphoton absorption and emission either over or through the tunnel barrier (photofield emission). In tungsten, laser intensities approached the intermediate Keldysh regime, where emission may not be cleanly described as multiphoton or tunneling in the optical field. Although we did not observe field-dependent effects, numerical modeling of emission in this regime shows that emission is sub-optical cycle. The low thermal conductivity of hafnium carbide prevented us from working at high peak laser intensities. Instead, we studied the crossover between multiphoton emission and thermal-assisted field emission, finding that even though the average temperature of the tip rose substantially due to laser illumination, transient thermal emission before the electron and lattice temperatures equilibrate is undetectable in comparison with multiphoton emission.

Although the identification of emission mechanisms provides indirect evidence that the emission time is short, we would like to directly characterize the emission time. Chapter 4 describes “energy-domain streaking” of the electron emission, where we use a rapidly varying tip voltage to map the electron emission time onto the electron’s energy. Approached with a different perspective, the same experiment represents an ultrafast sampling oscilloscope with a temporal resolution set by the 10 fs laser pulse duration. Finally, Chapter 5 proposes a method of studying pulse duration at a hypothetical experimental target (for example, an ultrafast beamsplitter or a target

for electron diffraction) based on electron energy gain in an evanescent optical field.

Chapter 2

Electron emission mechanisms

The first part of this chapter summarizes the physics of DC electron emission processes from sharp tips, which is useful for understanding laser-induced emission processes. The second part summarizes laser-induced emission processes.

2.1 Thermionic emission and field emission

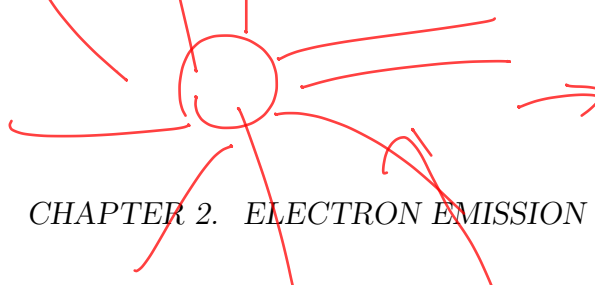
Before considering (ultrafast) laser-induced electron emission processes, it is helpful to understand electron emission that occurs as a result of an electric field bias and/or heating of a sharp metal cathode. The laser-induced emission processes can be understood as modifications of these processes by adding energy to the electron gas in a controlled way.

Just as a certain minimum ionization energy is required to remove an electron from an atom or molecule, a certain amount of energy is required to remove an electron from a metal. This energy is called the work function.

Thermionic emission occurs when the metal is heated enough that some thermally excited electrons have enough energy to overcome the work function and escape. The emitted current as a function of temperature is described by the Richardson-Dushman equation,

$$J = \lambda_R A_0 T^2 e^{-\phi/(k_B T)}, \quad (2.1)$$

a function
of # of
atoms
being emitted, size of
tip?



To which direction does it decrease

CHAPTER 2. ELECTRON EMISSION MECHANISMS

15

where

$$A_0 \equiv \frac{4\pi m k_B^2 e}{h^3} = 1.2 \times 10^6 \text{ A/(m}^2\text{K}^2\text{)} \quad (2.2)$$

is the Richardson constant, J is the emitted current density, ϕ is the work function, T is the temperature, k_B the Boltzmann constant, and λ_R is an empirical pre-factor that varies slightly from one material to another [36]. Often, a bias field is applied to thermionic emitters, which, besides accelerating the emitted electrons, has the effect of reducing the surface potential barrier to a value smaller than ϕ (this is called the Schottky effect). Note that thermionic emission depends strongly on electron temperature, with the exponential dependence suggesting a Boltzmann factor for the population of electrons with energy equal to the potential barrier height.

Field emission refers to electron emission at an interface between a conductor and a non-conductor due to the application of a strong electric field (typically 1-10 GV/m). The most common situation is electron emission from a sharpened metal tip (called a field-emission tip) into vacuum. The strong applied electric field creates a finite potential barrier which the electrons may tunnel through quantum mechanically (Fig. 2.1).

The Fowler-Nordheim equation [37] describes the relationship between applied field, F , work function, ϕ , and emitted current density, J :

$$J = \frac{e^3 F^2}{18\pi^2 \hbar \phi} \exp \left[-\frac{8\pi\sqrt{2m}\phi^{3/2}}{3heF} v(f) \right], \quad (2.3)$$

Here, e and m are the electron charge and mass, respectively. The form of $v(f)$ will be discussed later; it is a function of a dimensionless parameter, f , and is related to the evaluation of an elliptic integral, but its value is typically close to 1. The equation is valid at 0 K; however, as will be discussed below, the correction to this equation at room temperature is quite small.

The derivation of the Fowler-Nordheim equation will be sketched in the next sections. For now, note the following things:

1. To achieve the requisite field strengths while applying reasonable voltages to the metal, etched field emission tips, which terminate in half spheres of radius

$r \approx 50\text{-}500 \text{ nm}$ are used as field emitters. The field at the apex of the tip is given by

$$F = \frac{V}{k r}, \quad (2.4)$$

with V the potential difference between the tip and extraction electrode and k a geometrical factor that depends on the shape of the field emitter (for example, cone angle near the apex) and distance to the extraction electrode. In practice, one measures the emitted current, I as a function of V (rather than J as a function of F); I is proportional to J , and the proportionality factor is the emission area.

2. The current is approximately proportional to $\exp(-a/F)$, where a is some factor. This is roughly what one should anticipate given that the physical process behind emission is tunneling through a barrier, and the “width” of that barrier has something to do with $1/F$. Arguing very loosely, if we imagine for a moment that the triangular barrier shown in Figure 2.1(b) is instead a rectangular barrier of width $\phi/(e|F|)$, and a plane wave electron wave function with energy ϕ below the top of the barrier is incident upon it, we would expect the wave function to decay as an exponential in the barrier, with decay length

$$\alpha = \sqrt{\frac{\hbar^2}{2m\phi}}, \quad (2.5)$$

so that the probability of transmission should be something like

$$P \sim \exp \left[\frac{2}{e} \left(\frac{2m}{\hbar^2} \right)^{1/2} \frac{\phi^{3/2}}{|F|} \right]. \quad (2.6)$$

This gets remarkably close to the “right” answer for how the emitted current should depend on applied field and work function. To get the full Fowler-Nordheim equation, one needs to more accurately treat the shape of the potential barrier and note that electrons are incident also at energies below the Fermi level (and, at non-zero temperature, a little above it).

2.1.1 The surface potential barrier

Schottky effect

We need a basic model for the potential seen by an electron at the metal vacuum interface to derive the equations describing electron emission from the metal surface. Suppose that the metal fills the region of space $x < 0$, and choose the zero of potential energy to be the zero of the conduction band so that the potential energy is zero inside the conductor. Then in the vacuum region ($x > 0$), we expect the potential energy of an electron as a function of x to be something like

$$U(x) = \mu + \phi - eFx, \quad (2.7)$$

where μ is the Fermi energy, ϕ the work function, and F the applied electric field. If the electronic states of the metal are full up to the Fermi energy, μ , then an energy ϕ is required to remove an electron from the metal. The atomic corrugation of the potential inside the metal is ignored. Since the metal is a good conductor, the field does not penetrate the metal and $U(x) = 0$ for $x < 0$. Note that this is not the case for semiconductors, and the resulting surface potential barrier is qualitatively different from that described here [38].

As an electron leaves the metal, the potential of equation 2.7 is modified, because the conduction electrons move to shield the interior of the metal from the field of the free electron. As a result, we must add a term to the potential energy function, which is typically called the image potential or image correction. Using the classical image potential for an electron at a distance x from an infinite conducting plane yields (for the full surface barrier)

$$U(x) = \mu + \phi - eFx - \frac{e^2}{16\pi\epsilon_0 x}. \quad (2.8)$$

Clearly, for sufficiently small x , when the electron is very close to the surface, it seems like a many-body quantum mechanical description will be required. For the calculations that follow, the expression for the potential is most important in the barrier region, where $U(x) \gtrsim \mu$. It has been shown that the details of the potential at

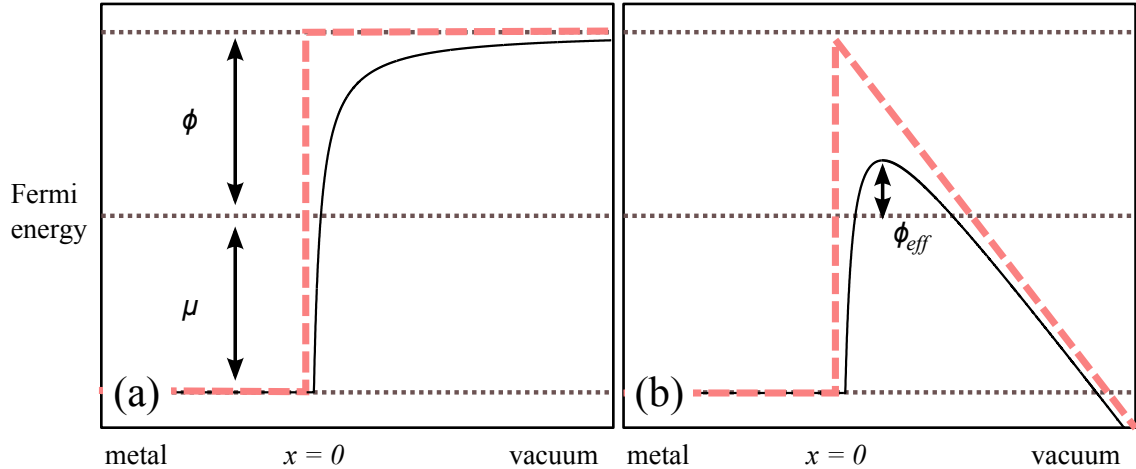


Figure 2.1: (a) Potential energy for an electron near the surface of a metal, with no applied field. Solid curve includes the image correction, dashed curve is without. The potential has been modified near $x = 0$ as in Ref. [39] to remove the singularity in the image correction. (b) Same, but with an applied field. Note that the image correction leads to a reduction in the barrier height to $\phi_{\text{eff}} < \phi$ (the Schottky effect).

very small x do not significantly affect the probability that an electron tunnels through the barrier [39], and for the calculation of tunneling coefficients, the divergence of the image potential is removed within some distance ϵ of the origin, and the potential is made to smoothly connect with the expression for $x < 0$.

The inclusion of the image potential in Eq. 2.8 means that, when a bias field is applied, the height of the potential barrier is less than the work function. The barrier reduction is called the Schottky effect, and it is important for thermionic and photo-emission, as well as field emission.

The effective potential barrier is given by

$$\phi_{\text{eff}} = \phi - \sqrt{\frac{e^3 F}{4\pi\epsilon_0}}. \quad (2.9)$$

Surface dipole contribution to the work function

An electrostatic double layer or surface dipole arises at the metal-vacuum interface, even for clean metal surfaces. This dipole contributes to the work function and can cause different surface orientations of the same material to have different work functions. Adsorbed atoms and molecules can change the surface dipole and therefore the work function. This is the physical origin of patch fields on electrodes.

The work function can be written as the sum of two contributions, a volume contribution and a surface contribution:

$$\phi = \phi_{\text{bulk}} - \frac{ep}{\epsilon_0}. \quad (2.10)$$

ϕ_{bulk} is the work function calculated for a hypothetical infinite crystal (or, alternatively, one can think of it as the energy required to remove a single electron from a finite crystal and place it infinitely far away), and p is the dipole moment per unit area, defined with positive dipole pointing away from the surface. The total work function, ϕ , is the energy required to remove an electron to a point just outside the crystal; specifically, to some distance x that is much greater than the inter-atomic spacing, but smaller than the overall dimensions of the crystal.

Smoluchowski effect and the field emission microscope. Researchers in the early days of field emission quickly realized that the work function of a crystal varies with surface orientation, and that the variations in work function between the different crystal faces are similar for metals with the same crystal lattice [40]. This variation in work function is due to differences in the size of the surface dipole for different crystal orientations.

If one imagines taking an infinite crystal and cutting it to form a surface, the electron density at the surface will change due to the created asymmetry. To maintain charge neutrality in this thought experiment, we cut the full charge distribution along the edge of the Wigner-Seitz cell—if the electron distribution within the cells at the surface stayed the same as those in the bulk crystal, then there would be no surface dipole. However, electrons leak out of the cell in the direction perpendicular to the

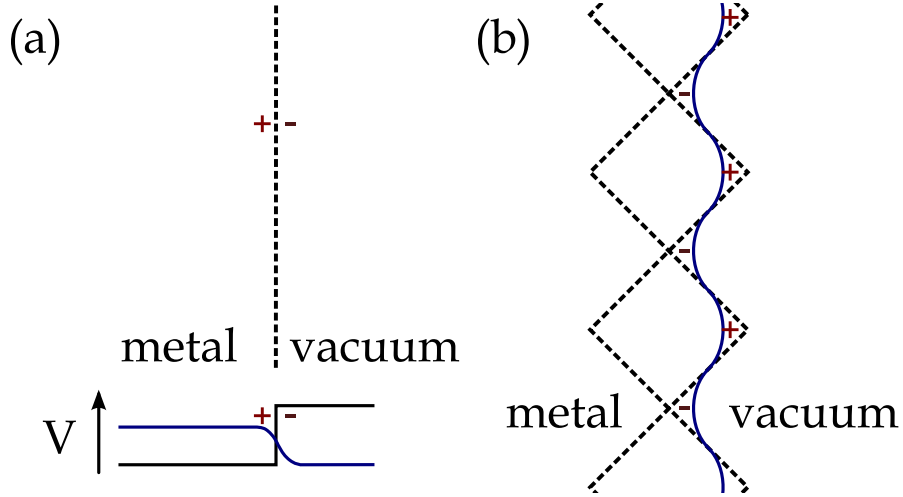


Figure 2.2: Surface dipoles. (a) At the surface of the metal, a dipole can form from electrons leaking into the vacuum. The electron density (blue curve) is superimposed on the potential created by the ions. (b) Smoluchowski effect. The surface of constant charge density (blue curve) is smoothed relative to the boundaries of the Wigner-Seitz cell.

surface (Fig. 2.2(a)), and they also leak out *along* the surface. Since the momentum operator is the spatial derivative of the wavefunction, rapid changes in electron density require high values of kinetic energy for a state, which encourages electron wavefunctions to smooth out. The true surfaces of constant electron density form smooth curves rather than following the boundaries of the Wigner-Seitz cell. This creates a positive surface dipole (Fig. 2.2(b)), counteracting the negative dipole due to leakage of electrons normal to the surface. This effect is named for Smoluchowski, who first proposed it [40]. Close-packed crystal planes have less corrugation and a smaller positive contribution to the dipole, resulting in a larger work function. Thus the variation of the surface dipole with crystal orientation at the surface gives rise to a variation in emission current over the surface of the emitter, because certain atomic sites have lower work function and thus higher current for a given bias field.

The small radius of curvature of the tip, necessary for achieving strong bias fields, also provides a mechanism for imaging the work function variations over the surface of the tip, with a resolution approaching the atomic scale. As electrons leave the tip, they follow the field lines near its surface, projecting the emission pattern (i.e.

variation in emission current over the surface of the emitter) onto the detector. The magnification (in the absence of electron lenses) is $d/(\beta_F r)$, where d is the distance from the tip to the detector, r is the tip radius, and β_F is due to the field lines and electron trajectories bending over some distance from the tip instead of being perfectly radial. The spatial resolution is limited by the transverse velocities of the emitted electrons to about 2 nm [38].

Effect of surface adsorption. Adsorbed gases on the surface can change the surface dipole, as charges are transferred to or from the adsorbate. One can guess the sign of the induced dipole and concomitant work function change based on the electronegativity of the adsorbate relative to the electronegativity of the metal, although there are exceptions to this rule [41]¹. Surface adsorption can affect the relaxation of the metal surface (adjustment of the lattice parameter near the surface), but this is usually much smaller than the dipole change due to charge transfer [41]. The change in work function due to surface contamination is typically ~ 0.1 eV but can be as large as 2 eV [38].

From the above considerations, it is clear that the surface cleanliness has a strong impact on the work function and therefore the behavior of electron emission from metal surfaces. For our work on ultrafast electron emission, the field-emission tip is maintained in ultra-high vacuum (UHV), at a pressure below the measurement limit of the ion gauge on the system, which is 3×10^{-10} torr. If the tip is sufficiently sharp ($r < 150$ nm), an atomically clean surface can be obtained via field evaporation [38]. With blunter tips, voltages in excess of 20 kV are required to achieve sufficiently high fields, which exceeds the rating of the electrical feedthroughs currently in use. In place of field evaporation, tips may be cleaned at the start of data taking by “flashing,” or heating to a predetermined temperature for 2–4 seconds to desorb gases (the detailed anneal procedure is described in Appendix A). It is important to recognize, however, that the degree of surface contamination can easily change during operation of the experiment. For example, when the laser beam is focused on the tip, it can induce desorption, especially if the beam is mis-aligned up the shank of the tip at high power,

¹For example, for an adsorbate with high electronegativity, if there is some degree of chemical bonding with the surface, electrons from the adsorbate may become more concentrated in the region between the surface and adsorbate, countering the expected surface dipole.

which has the effect of heating the tip. On the other hand, the microchannel plate used for electron detection has significant outgassing if the current flowing in it is large, which temporarily raises the background pressure in the chamber and can lead to contamination of the tip.

2.1.2 Derivation of the Fowler-Nordheim equation

Under the WKB approximation, it is straightforward to calculate the probability that an electron tunnels through a one-dimensional barrier as a function of the incident electron's energy. The electrons of the metal have a distribution of kinetic energies, and by integrating over the distribution of kinetic energies normal to the barrier multiplied by the tunnel probability, we can obtain an expression for field emitted current density as a function of temperature and applied field:

$$J(F, T) = e \int D(E_{\perp}, F) N(E_{\perp}, T) dE_{\perp}, \quad (2.11)$$

where e is the elementary charge, F is the applied field, T the temperature, and E_{\perp} the energy normal to the barrier. $D(E_{\perp}, F)$ is the probability that an electron is transmitted through the barrier and $N(E_{\perp}, T)dE_{\perp}$ is the number of electrons per unit time per unit area incident upon the barrier with energy between E_{\perp} and $E_{\perp} + dE_{\perp}$. For the Sommerfeld model (i.e. taking the potential inside the metal to be constant, which results in the simplest possible electronic structure for the metal),

$$N(E_{\perp}, T)dE_{\perp} = \frac{4\pi m k_B T}{h^3} \log(1 + e^{(\mu - E_{\perp})/(k_B T)}) dE_{\perp}, \quad (2.12)$$

with m the mass of the electron, and k_B the Boltzmann constant. For a one-dimensional potential $U(x)$, the transmission coefficient in the WKB approximation is given by

$$D(E_{\perp}) \approx \exp\left(-2\frac{\sqrt{2m}}{\hbar} \int_{x_-}^{x_+} \sqrt{U(x) - E_{\perp}} dx\right), \quad (2.13)$$

where x_+ and x_- are the classical turning points. For a free electron metal,

$$N(E_\perp, T_{\text{el}}) dE_\perp = \frac{4\pi m k_B T_{\text{el}}}{h^3} \ln(1 + e^{(\mu - E_\perp)/k_B T_{\text{el}}}) dE_\perp, \quad (2.14)$$

with h the Planck constant and k_B the Boltzmann constant. At 0 K, the integral can be evaluated to obtain the Fowler-Nordheim equation which, written in a modern form [42], is

$$J = \frac{e^3 F^2}{18\pi^2 \hbar \phi} \exp \left[-\frac{8\pi\sqrt{2m}\phi^{3/2}}{3heF} v(f) \right], \quad (2.15)$$

where

$$v(f) \approx 1 - f + \frac{1}{6}f \log f, \quad (2.16)$$

and

$$f \equiv \frac{e^3}{4\pi\epsilon_0} \frac{F}{\phi^2}. \quad (2.17)$$

As it is written, Equation 2.15 relates the current density to the applied field. Experimentally, we apply voltages and measure currents. Recall that the field at the surface of the tip is related to the voltage applied between the tip and an extraction electrode by the equation

$$F = \frac{V}{kr_{\text{tip}}}. \quad (2.18)$$

Here, r_{tip} is the radius of curvature of the tip, and k is a geometrical factor that depends on factors such as the cone angle of the tip and the distance to the extractor. The value of k is $\sim 4\text{--}5$, and it can be determined by numerical simulation of the experimental geometry (there are also some analytic approximations, see [38]). To make the conversion from current density to total current, we typically multiply by an effective emission area, A_{eff}

$$I = A_{\text{eff}} J. \quad (2.19)$$

The concept of effective emission area is mainly for convenience; in reality, since the work function and local field vary over the surface of the tip, the total current is the integral of the field emission current density over the tip surface.

Width of energy distribution

The barrier transmission coefficient can be expanded for electron energies near the Fermi energy as

$$D(E_{\perp}, F) \approx D(\mu, F) \exp((E_{\perp} - \mu)/d_F), \quad (2.20)$$

where

$$d_F(F) \equiv \left(\left[\frac{d \log D(E_{\perp}, F)}{d E_{\perp}} \right]_{E_{\perp}=\mu} \right)^{-1} \approx \frac{e\hbar F}{2\sqrt{2m\phi}}. \quad (2.21)$$

Since the total energy is just the sum of the kinetic energy perpendicular and parallel to the barrier, we have

$$E = E_{\perp} + E_{\parallel}. \quad (2.22)$$

The current density at energy E can now be written as an integral over E_{\parallel} .²

$$\begin{aligned} j(E)dE &= \int \frac{4\pi em}{h^3} f_{\text{F-D}}(T, E) D(E_{\perp}, F) dE_{\parallel} \\ &= \frac{4\pi em}{h^3} f_{\text{F-D}}(T, E) D(\mu, F) \exp((E - \mu)/d_F) \int_0^E \exp(-E_{\parallel}/d_F) dE_{\parallel}, \end{aligned} \quad (2.23)$$

where $f_{\text{F-D}}(T, E)$ is the Fermi-Dirac distribution

$$f_{\text{F-D}}(T, E) = \frac{1}{1 + \exp((\mu - E)/k_B T)}. \quad (2.24)$$

The decay constant d_F is usually small enough that upper limit of the integral can be taken as infinity. The result is that the energy distribution is

$$j(E)dE = \frac{4\pi emd_F}{h^3} f_{\text{F-D}}(T, E) D(\mu, F) \exp((E - \mu)/d_F). \quad (2.25)$$

At low temperatures, $f_{\text{F-D}}$ cuts off sharply at the Fermi energy; thus the full-width

²Note that this differs from the previous section, where total current density was obtained by integrating over E_{\perp} .

half max (FWHM) of the energy distribution can be approximated as

$$\Delta E_{\text{FWHM}} \approx d_F \log 2. \quad (2.26)$$

2.1.3 The Richardson-Dushman equation for thermionic emission

In the thermionic emission regime, the temperature is high enough and the bias field low enough that the majority of emitted electrons escape classically over the barrier. In this limit, the barrier transmission coefficient takes the simple form (to first approximation)

$$D(E_{\perp}, F) = \theta(E_{\perp} - (\mu + \phi_{\text{eff}})). \quad (2.27)$$

θ is the Heaviside function, E_{\perp} is again measured from the bottom of the conduction barrier, and ϕ_{eff} is the Schottky-reduced work function (Eq. 2.9). Using the same free-electron metal approach as for the derivation of the Fowler-Nordheim equation, the emitted current density is given by

$$J(T, F) = \frac{4\pi emk_B T}{h^3} \int_0^{\infty} D(E_{\perp}, F) N(E_{\perp}, T) dE_{\perp} \quad (2.28)$$

$$= \int_{\mu + \phi_{\text{eff}}}^{\infty} N(E_{\perp}, T) dE_{\perp}. \quad (2.29)$$

Field dependence enters only through ϕ_{eff} . The integral can be computed using special functions to obtain

$$J(T, F) = \frac{4\pi em(k_B T)^2}{h^3} \left[\frac{1}{2} \left(\frac{\phi_{\text{eff}}}{k_B T} \right)^2 + \frac{\pi^2}{6} + Li_2(-e^{\phi_{\text{eff}}/k_B T}) \right], \quad (2.30)$$

where Li_2 is the polylogarithm of order 2;

$$Li_s = \sum_{k=1}^{\infty} \frac{z^k}{k^s}. \quad (2.31)$$

For thermionic emission, typically $\phi_{\text{eff}}/k_B T \gg 1$, and this expression becomes approximately³

$$J(T, F) = \frac{4\pi em(k_B T)^2}{h^3} e^{-\phi_{\text{eff}}/k_B T}, \quad (2.32)$$

which is known as the Richardson-Dushman equation. To obtain quantitative agreement between the theory and experiment, it is usually necessary to introduce a prefactor (see Eq. 2.1) that corrects for effects that have been ignored in this elementary derivation such as the true band structure of the material and electron reflection at the metal-vacuum interface, which occurs even when the electrons can escape classically. The FWHM energy spread of the emitted electrons is approximately

$$\Delta E = 2.45k_B T. \quad (2.33)$$

2.1.4 Thermal-assisted field emission

By definition, field emission current is dominated by electrons emitted from near the Fermi level, and thermionic emission current is dominated by electrons from the tail of the Fermi-Dirac distribution whose energies exceed the barrier height. In between these two limits, where thermal excitation is important but the electrons escape predominantly by tunneling, an analytic approach is more difficult. Calculating the emitted current amounts to evaluating the integral of Eq. 2.28 but replacing the step function barrier transmission with the WKB transmission probability (Eq. 2.13). Murphy and Good presented an analytic approximation for what they call the temperature-field intermediate regime, but it is only valid for a limited range of parameters [39]. More recently, Jensen presented a piecewise analytic approximation that can be used over the full range of combinations of T and F . For our work on emission caused by laser-induced heating, we used the term thermal-assisted field emission, and we found that it was reasonable to calculate the current by simply numerically integrating Eq. 2.11. After measuring the I - V (current-voltage) relation for a tip at room temperature, one can determine kr_{tip} and A_{eff} , the parameters necessary to convert between F and V and J and I . With this information, the family of I - V

³In fact, the approximation is accurate to within 10% for $\phi_{\text{eff}}/k_B T > 1.5$ and 1% for $\phi_{\text{eff}}/k_B T > 3$.

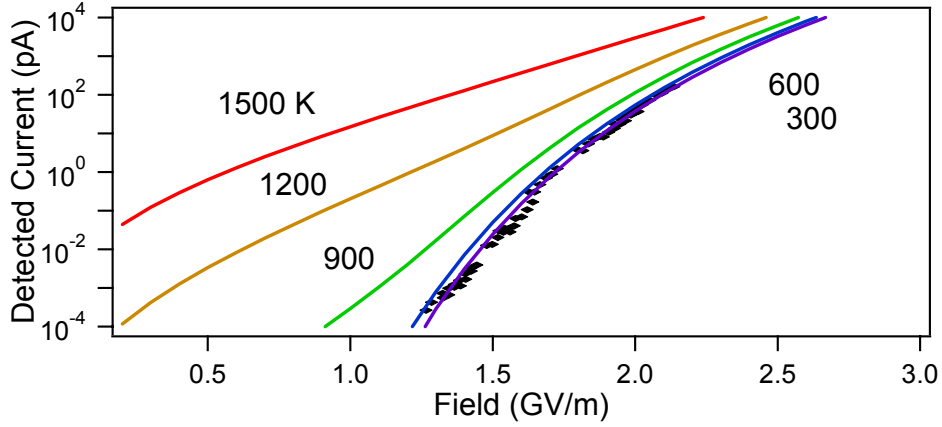


Figure 2.3: Experimental I - V curve for DC emission at 300 K, and theoretical I - V curves for thermal-assisted field emission from the same tip at elevated temperatures. The theory curves are determined by numerical integration, as described in the text. Adapted from [43] ©2012 APS.

for the same tip at higher temperatures can be determined numerically (Fig. 2.3). Note that the I - V curve at 300 K is not substantially different from the 0 K curve, so analytic Fowler-Nordheim equation is a good description.

2.2 Laser-triggered electron emission

The basic physical process is that light deposits energy in the electron gas, freeing electrons from the material. The precise details of this process depend on the nature of the optical absorption, electron gas dynamics, and shape of the surface potential barrier. In terms of emission process, there are two main distinctions between a sharp photocathode and a planar one: first, due to the small radius of curvature of the tip, very strong electric fields can be applied, so that the size and shape of the surface potential barrier becomes a parameter that can be varied experimentally. Second, optical field enhancement at certain locations on the tip apex results in local laser electric fields on the order of GV/m, comparable to the DC field required for field emission. This is (loosely) the criterion for strong-field photoemission.

2.2.1 Overview of ultrafast emission processes

In the 1970's and 80's, experiments on laser-assisted field emission using continuous wave (cw) lasers identified the process of photo-assisted field emission (also called photofield emission) [4, 44]. In this process, electrons in the metal absorb one or more photons, are promoted to a level below the peak of the surface barrier, and tunnel to escape the metal. This process was also identified in ultrafast electron emission from a tungsten field emission tip, using 65 fs pulses at 780 nm [6]. As peak laser intensity increases, multiphoton emission can dominate photofield emission [6, 9, 7], and the components of the current from photofield and multiphoton emission can be distinguished by their relative energies, which are separated by integer steps equal to the photon energy [45]. As peak laser intensity increases further, the emission eventually shows sub-optical cycle modulation [9, 10], and suppression of lower photon orders due to the large ponderomotive potential of the exciting laser (above-threshold photoemission) [19].

For photoelectron emission from a bound system, Keldysh theory defines the limit of validity for a multiphoton emission description as the condition $\gamma_K \gg 1$, with the γ_K the Keldysh parameter:

$$\gamma_K = \frac{\omega\sqrt{2m\phi}}{eE_p}, \quad (2.34)$$

where E_p is the peak electric field of the laser. In the opposite limit ($\gamma_K \ll 1$), the emission can be described as tunneling of electrons from the Fermi level under the influence of the strong laser electric field. In this limit, it is clear that the emission is modulated on the time-scale of the laser optical cycle, as tunneling is suppressed each time the laser electric field reverses direction. In practice, the limit $\gamma_K \ll 1$ has not been achieved in laser-triggered emission from nanometric tips (nor is it typically achieved in gas-phase high harmonic generation experiments [46], which nevertheless rely on laser-field-dependent emission). In references [6], [10], and [19], the Keldysh parameter (γ_K) is of order 1, and yet sub-optical cycle structure is still predicted (and observed, in [10]). Because of this fact, this regime is called the non-adiabatic tunnel regime.

Multiphoton emission

In a simple multiphoton emission model, n -photon absorption is assumed to simply translate a fraction of the Fermi-Dirac distribution by $n\hbar\omega$. The resulting supply function is

$$N_{\text{mp}}(E_{\perp}, T) = \alpha_n I^n N(E_{\perp} - n\hbar\omega, T) \quad (2.35)$$

where $N(E_{\perp}, T)$ is the supply function used before in the derivation of both the Fowler-Nordheim and the Richardson-Dushman equations (Eq. 2.14). The quantity $\alpha_n I^n$ is the proportion of electrons that are excited; it has been written to show its dependence on laser intensity, I [47]. The emitted current density is

$$\begin{aligned} J_{\text{mp}}(T, F) &= e \int_0^{\infty} N_{\text{mp}}(E_{\perp}, T) D(E_{\perp}, F) dE_{\perp} \\ &= e \alpha_n I^n \int_0^{\infty} N(E_{\perp} - n\hbar\omega, T) \theta(E_{\perp} - (\mu + \phi_{\text{eff}})) dE_{\perp} \\ &= e \alpha_n I^n \int_{\mu + \phi_{\text{eff}} - n\hbar\omega}^{\infty} N(E_{\perp}, T) dE_{\perp} \end{aligned}$$

But we evaluated this integral before (with different integration limits) in the derivation of the Richardson-Dushman equation. The result is

$$J_{\text{mp}}(T, F) = \alpha_n I^n \frac{4\pi em(k_B T)^2}{h^3} \left[\frac{1}{2} \frac{(n\hbar\omega - \phi_{\text{eff}})^2}{(k_B T)^2} + \frac{\pi^2}{6} + Li_2(-e^{-(n\hbar\omega - \phi_{\text{eff}})/(k_B T)}) \right]. \quad (2.36)$$

Now, because the argument of the exponential is negative, the contribution of the final term is small as long as $(n\hbar\omega - \phi_{\text{eff}})/k_B T \gg 1$, so that

$$J_{\text{mp}}(T, F) \approx \alpha_n I^n \frac{4\pi em(k_B T)^2}{h^3} \left[\frac{1}{2} \frac{(n\hbar\omega - \phi_{\text{eff}})^2}{(k_B T)^2} + \frac{\pi^2}{6} \right]. \quad (2.37)$$

This approximation has an error of less than 10% when $(n\hbar\omega - \phi_{\text{eff}})/k_B T > 1.51$ and less than 1% when it is greater than three. Note that the field dependence enters through ϕ_{eff} .

The energy spread now depends on the degree of excitation over the barrier; in the simplest model of monochromatic excitation at zero temperature, the energy

distribution is rectangular with a width given by $n\hbar\omega - \phi_{\text{eff}}$. One can evidently create narrower energy distributions at the expense of total emitted current by tuning $n\hbar\omega$ close to the effective barrier height.

The derivation above neglects the fact that electrons excited below the barrier can still escape by tunneling if there is a strong bias applied. Using the tunneling transmission coefficient (Eq. 2.13) for E_{\perp} below the barrier, we can write a theory that includes both tunneling and over-the-barrier emission. If $n\hbar\omega < \phi_{\text{eff}}$, then the tunneling component dominates, and the process is called photo-assisted field emission. The emission in this regime is described by the Fowler-Nordheim equation with work function reduced by $n\hbar\omega$ and an overall prefactor of $\alpha_n I^n$.

Optical field emission

In the quasi-static or optical field-emission regime ($\gamma_K \ll 1$), we expect that the total charge emitted due to a single laser pulse can be calculated by substituting the time-dependent laser field into the Fowler-Nordheim equation.

$$J(F, T, t) = J_{\text{FN}}(F + F_{\text{laser}}(t), T). \quad (2.38)$$

In the non-adiabatic tunnel regime ($\gamma_K \rightarrow 1$), this optical field emission picture is not quantitative, but it can nevertheless be useful in developing intuition about the behavior of the system.

The small radius of curvature of the field emission tip makes it easier to obtain strong optical fields due to the phenomenon of optical field enhancement. Typical enhancement factors at the apex of a ≈ 100 nm radius tip are in the range 2–5. Although I am not aware of a systematic study of field enhancement as a function of the tip geometry (radius, cone angle), one expects that, similar to the behavior of a lightning-rod, as the radius of the tip gets smaller, the field at the apex should be stronger. Field enhancement diminishes as the size of the tip becomes comparable to the wavelength of light and retardation becomes important [48]. Field enhancement values reported in different contexts support this idea: Martin et al. calculate a field enhancement factor of 4.9 for a 10 nm tip [48], Schenk et al. infer a value of 4.2 ± 1.1

from experimental data for a 50 nm tip [19], and Yanagisawa et al. calculate a field enhancement of 2.5 for a 100 nm tip [49].

2.3 Summary

The aim of this chapter has been to present a unified view of the DC and ultrafast laser-induced emission processes as a context for understanding the remainder of this work. These emission processes are summarized graphically in Figure 2.4.

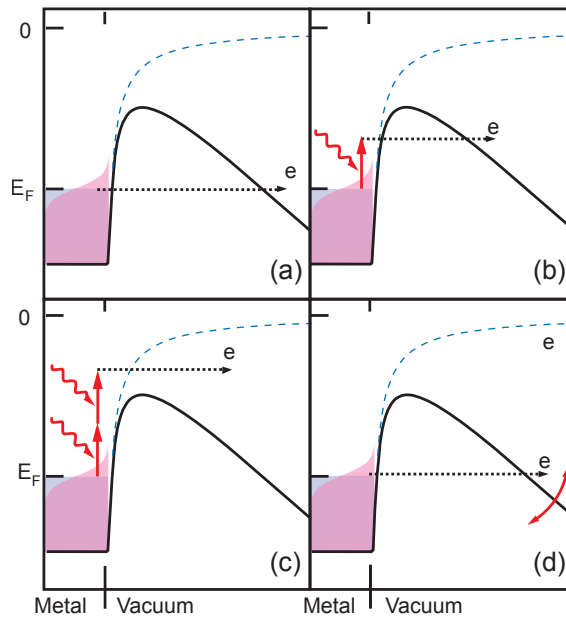


Figure 2.4: Emission processes from a biased tip. (a) DC emission. (b) Photo-assisted field emission. (c) Over-the-barrier emission. (d) Optical field emission. In all panels, the dotted blue line shows the potential seen by the electron in the absence of a bias field; the black line is the potential with a bias field, including the image potential and resulting barrier reduction. Increasing the field increases the magnitude of the slope of the linear part. The Fermi-Dirac distribution is illustrated schematically at $T = 0$ (dark purple) and $T > 0$ (light purple). In part (a), as the temperature increases, states with a higher tunnel probability are populated, leading to thermal-assisted field emission and eventually to thermionic emission, as the proportion of current due to electrons coming classically over the barrier increases. Parts (b)-(d) show laser-induced emission processes that occur in order of increasing laser intensity. Adapted from [43] ©2012 APS.

Chapter 3

Laser-induced emission from nanometrically sharp tips

This chapter will describe two experiments on ultrafast emission processes. The first is a study of electron emission from tungsten tips in the non-adiabatic tunneling regime. The second is on the tradeoff between two-photon photoemission and thermally-assisted field emission in laser-triggered electron emission from Hafnium Carbide tips.

3.1 Laser-induced electron emission from field emission tips in the non-adiabatic tunneling regime

In [6], it was shown that illumination of tungsten field emitters with 65 fs, 780 nm laser pulses resulted in photofield emission, with a transition to an extremely nonlinear regime as the laser intensity was increased. Building on these results, we proposed to explore whether this extremely nonlinear regime corresponded to the non-adiabatic tunneling regime and if we could measure field (as opposed to intensity) dependence in the emitted current.

How can we look for dependence of the electron emission on the laser field when this field oscillates at an optical frequency? One method is to look for a dependence of the emitted current on the carrier-envelope offset (CE or CEO) phase. As suggested

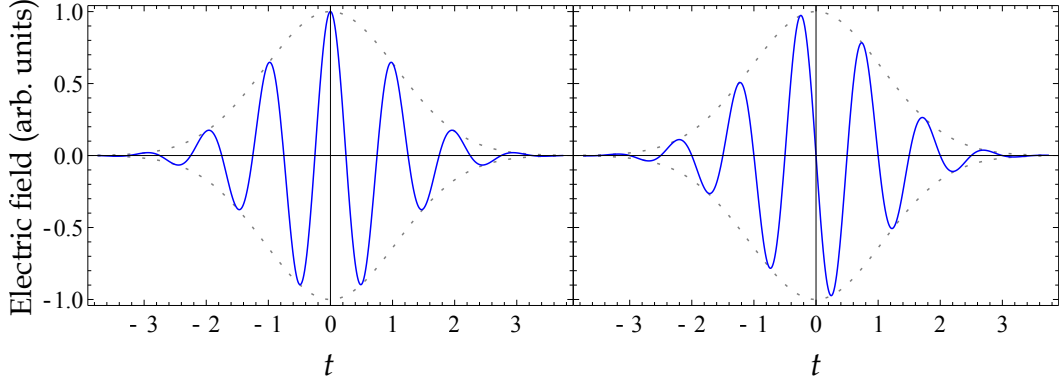


Figure 3.1: The electric field for two pulses with different carrier-envelope phase (the phase difference between the two pulses is $\pi/2$). The electric field envelope of the pulse is shown as a dotted gray line, and the horizontal axis is in units of the optical period. A pulse with $1/e^2$ intensity full width of 3 times the optical period is shown.

by its name, the carrier-envelope phase is simply the phase of the carrier at a reference point of the envelope of the intensity envelope of an optical pulse. For example, the gaussian pulses of Figure 3.1 have CE phases that differ by $\pi/2$. Note that the peak electric field is different for these two pulses (one may also note that this difference becomes larger as the pulses get shorter).

If we naively take the current emitted from the tip to be a function of instantaneous field, i.e. $I = f(F)$, then the total charge emitted due to a single laser pulse will be

$$Q = \int f(F(t))dt. \quad (3.1)$$

If f is a highly non-linear function of field (as is the Fowler-Nordheim equation), then there should be a difference in the integrated current for pulses of different carrier-envelope phase. For this reason, the $\gamma_K \ll 1$ limit (optical field emission) was proposed as a simple sensor for the carrier-envelope phase [50].

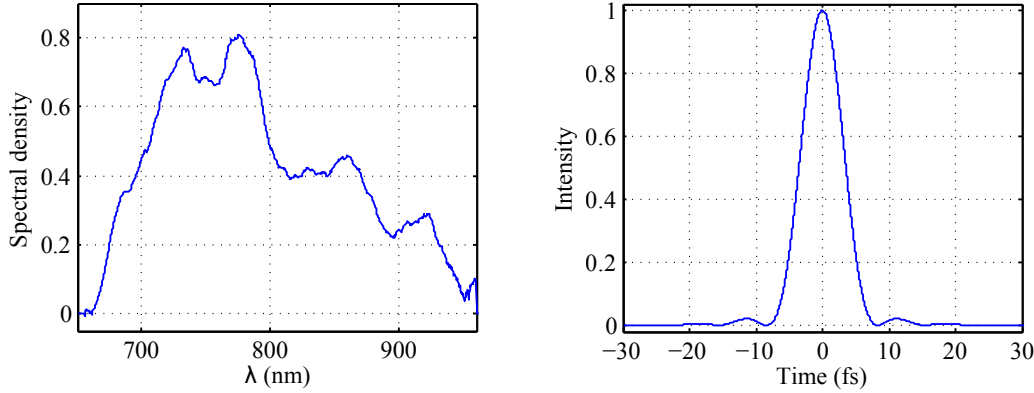


Figure 3.2: On the left side, the spectrum of the laser is shown. On the right side, the transform-limited pulse (obtained by Fourier transform of the spectrum with a flat spectral phase) is shown. The FWHM of the transform-limited pulse is 7.1 fs.

3.1.1 Experimental setup

In order to resolve carrier-envelope dependence, it is clear (from even the above simplified picture) that the pulse duration cannot be longer than a few optical cycles. For this work, therefore, we used an 8 fs Titanium:Sapphire laser (Nanolayers Ven-teon), which is pumped with 6 W from a solid-state diode-pumped, frequency doubled Nd:YVO₄ laser (Coherent Verdi V-10). Replacing the output coupler, the output power is typically 750 mW at a repetition rate of 150 MHz, so that the pulse energy is 5 nJ. The spectrum of the pulse is shown in Figure 3.2, with the transform limited pulse obtained from a Fourier transform of the spectrum with flat spectral phase. In reality, the pulses cannot be transform limited, as they acquire higher order spectral phase as they propagate through media (air, glass) due to dispersion. Negative dispersion is introduced into the beam path with double-chirped mirrors (Nanolayers), chosen so that the pulses are short at the location of the tip, as measured by interferometric autocorrelation.

The tip and microchannel plate electron detector are inside a vacuum chamber at a pressure of $< 3 \times 10^{-10}$ torr. The beam is incident upon the tip at a 90° angle to the tip axis, which allows the polarization to be parallel to the axis. The output of the laser is linearly polarized, and the polarization at the tip is set using an achromatic

half wave plate (Special Optics). Unless specifically noted, the polarization is parallel to the tip axis, because this favors photon absorption at the apex (see Section 3.1.3). The laser power incident on the tip is adjusted with a reflection off of a variable reflective neutral density filter, to avoid introducing extra dispersion.

The tip is negatively biased relative to the front of the dual-chevron microchannel plate-phosphor assembly (Burle/Photonis), and electrons leaving the tip roughly follow the electric field lines coming from the tip, resulting in a magnified image of the emission pattern. A voltage difference of approximately 2 kV is applied between the front and back plates of the MCP and between the back plate and the phosphor. The spatial resolution of the detector is approximately equal to its 10 μm pore size. The image of the electrons on a phosphor screen is seen through a viewport with a camera.

Electrons incident on the microchannel plate (MCP) create secondary electrons when they strike the wall of a pore, resulting in an avalanche process similar to that in a photomultiplier tube. The MCP has very high gain, which depends non-linearly on the the voltage difference between the front and back of the chevron assembly—changes of 100 V correspond to roughly a factor of 2-4 in gain. In addition to recording images of light emitted from the phosphor, the front of the MCP is connected to ground through a bias tee and a current-voltage preamplifier (SR570), which allows direct measurement of the low and high frequency components of the (amplified) current incident upon the detector.

For experiments on the CE phase, approximately 150 mW of the laser power is picked off (using a broad-band beamsplitter), and used to lock the carrier-envelope frequency the laser. For dispersion compensation measurements and studies of the non-linearity of emission, the beam is aligned first through a Michelson interferometer, and the output of one of the interferometer ports is incident on the tip.

3.1.2 Interferometric autocorrelation measured with the tip

With the beam-line configured to include the Michelson interferometer, we can measure interferometric autocorrelations using the tip as the detector. An interferometric

autocorrelation trace (IAC) requires a detection process that depends on the square of the intensity. If a linear detection process is used, the resulting field autocorrelation depends only on the spectrum of the pulse, and cannot be used to test the dispersion compensation. One common non-linear detection scheme is to focus the output of the interferometer into a non-linear crystal to generate light at the second harmonic frequency, which is then detected. For appropriate bias voltages, electron emission from the tip is second-order nonlinear in laser intensity, and so by recording the amount of electron emission as a function of delay between the two arms of the Michelson interferometer, we effectively measure the IAC.

Interferometric autocorrelation traces measured with the tip and with the more conventional second harmonic generation (SHG) are shown in Figure 3.3, and allow us to verify correct dispersion compensation of the beamline to ensure short pulses at the tip (note that the autocorrelation measures the pulse duration at the location of the second-order process—either the tip or the non-linear crystal).

The autocorrelation traces measured with the tip exclude some emission scenarios that imply longer-lasting emission. For example, we can refute the idea that the emission process is thermal-assisted field emission, because the temperature of the tip should stay elevated following the first laser pulse for on the order of 100 fs. Thus, the application of the second laser pulse to the already hot electron gas would lead to enhanced emission relative to the case when the first laser pulse is blocked. However, at time delays greater than the pulse duration, the baseline is flat, and additive (the current resulting from both pulses is simply the sum of the current from each arm individually).

In gold, interferometric autocorrelation traces measured with 3-photon photoemission have larger wings than a theoretical autocorrelation based on an instantaneous third order effect [51]. The distortion was attributed to the excitation of long-lived states by the initial pulse, which are then “probed” by the second pulse. In contrast, the interferometric autocorrelations measured with laser-induced emission from the tungsten tip are similar to the theoretical dispersion-compensated IAC as well as one measured with a crystal autocorrelator.

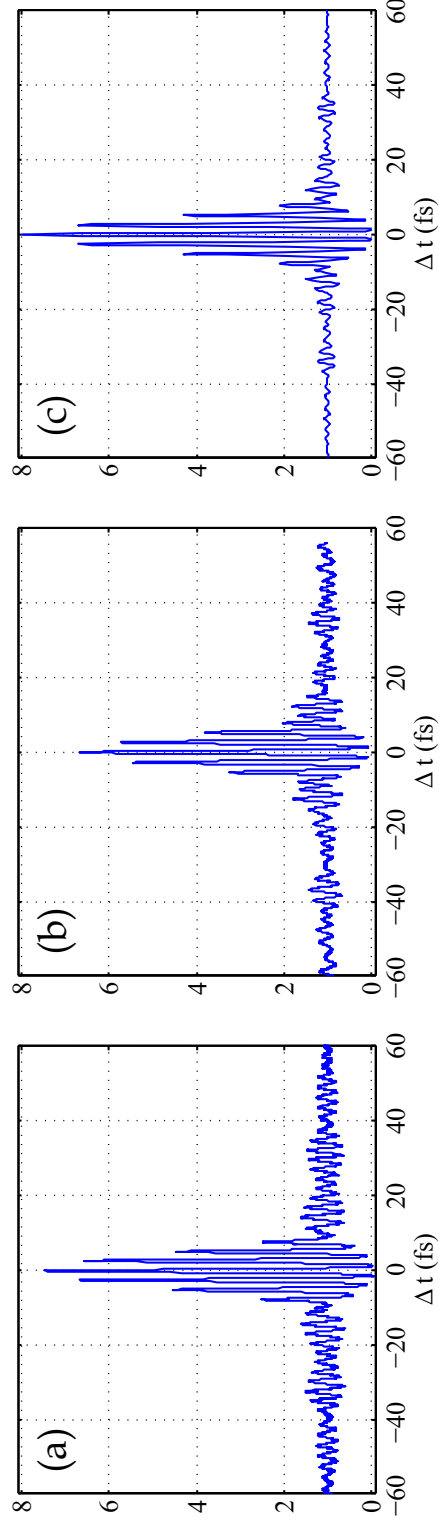


Figure 3.3: (a) Interferometric auto-correlation trace measured using SHG. (b) Interferometric auto-correlation trace measured in current emitted from the tip. (c) Simulated interferometric autocorrelation trace of the transform-limited pulse shown in Fig. 3.2. All of the traces have been scaled to a value of 1 in the base-line; their peak values should be 8, but are somewhat lower due to imperfect alignment of the Michelson interferometer.

3.1.3 Power non-linearity as a function of bias voltage

The non-linearity of the emission process is, however, not always second order! The ratio of the amplitude of the autocorrelation trace at its peak to the value in the baseline (time-delay between the pulses \gg pulse duration) is a proxy for this non-linearity. Consider a pulse with field profile $E_1(t)$ in one arm of the interferometer. The second interferometer arm contains a replica of this pulse at a time delay Δt . If $\Delta t = 0$, then the pulses interfere constructively, and the n-th order autocorrelation signal is maximized

$$A(\Delta t = 0) = A_0 \int |2E_1(t)|^{2n} dt, \quad (3.2)$$

where A_0 is some physical constant relating to the detection process. If, on the other hand Δt is very large so that the pulses no longer overlap in time, then they cannot interfere with one another, and all cross-terms become zero

$$\begin{aligned} A(\Delta t \rightarrow \infty) &= A_0 \int |E_1(t) + E_1(t + \Delta t)|^{2n} dt \\ &= A_0 \int |E_1(t)|^{2n} dt + A_0 \int |E_1(t + \Delta t)|^{2n} dt \\ &= 2A_0 \int |E_1(t)|^{2n} dt. \end{aligned} \quad (3.3)$$

By inspection, the peak-to-baseline ratio is then 2^{2n-1} . Note that we made no assumptions about the shape of the pulses beyond that they go to zero fast enough that we could cancel cross-terms when computing the baseline. Recording the peak-to-baseline ratio of the autocorrelation trace as a function of DC bias voltage (Fig. 3.4), we found that for a DC bias above 1.2 GV/m, the process had a peak-to-baseline ratio of 8, as expected for a two-photon emission process. Below this bias, the peak-to-baseline ratio increases continuously, up to a value of 25 near 0.5 GV/m bias. If the emission has a pure power-law dependence ($J \propto I^n$), this would imply an $n = 2.8$. To interpret this, note that the center wavelength of the laser spectrum corresponds to a photon energy of $\hbar\omega = 1.55\text{eV}$. The electric field required to bring the potential barrier down to $\phi_{\text{eff}} = 2\hbar\omega$ is 1.4 GV/m. The laser power used for this measurement was approximately 100 mW at the peak of the autocorrelation trace (when the pulses

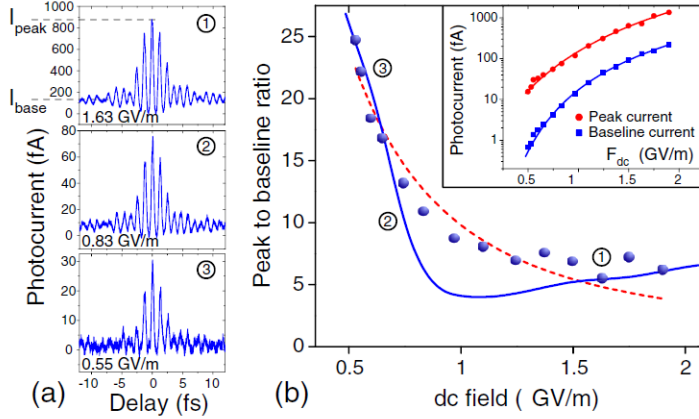


Figure 3.4: (a) Autocorrelation traces for three different DC voltages (laser parameters are the same). (b) Peak to baseline ratio vs. DC tip voltage. Blue points are data. The solid blue line is from numerical integration of the time-dependent Schrödinger equation, and the dashed red line is a quasistatic model fit to the data. The numbers in circles correspond to the traces in part (a). Inset: peak and baseline current vs. DC tip voltage. Reproduced from [9] ©2006 APS.

from the two arms of the interferometer interfere constructively).

Polarization dependence

Two physical effects are responsible for the basic polarization dependence of the laser-induced emission. The first is that the emission is typically dominated by the surface photoeffect [44], which, as will be shown below, depends only on the component of the laser electric field that is normal to the surface. The second is that the sub-wavelength size of the tip leads to optical field enhancement, which is larger for polarization parallel to the tip axis.

Consider, for simplicity, excitation of a (locally) flat metal surface by monochromatic light, with photon energy $\hbar\omega$. The emitted current can be approximated as a sum over the probability of all possible optical transitions multiplied by the barrier

transmission coefficient for the final state, $D(j)$.

$$\begin{aligned} J &\propto \sum_{ij} P(|\phi_i\rangle \rightarrow |\phi_j\rangle) D(j) \\ &\propto \sum_{ij} |M_{ij}|^2 D(j), \end{aligned} \quad (3.4)$$

where

$$M_{ij} \equiv \langle \phi_j | \epsilon^t \cdot \nabla V | \phi_i \rangle \quad (3.5)$$

is the matrix element of the transition, $|\phi_i\rangle$ and $|\phi_j\rangle$ are the initial and final electronic states, with energy E_i and $E_j = E_i + \hbar\omega$, respectively, ϵ^t is the polarization vector of the transmitted light, and V is the potential seen by the electrons [44]. V is given by

$$V(\mathbf{r}) = \begin{cases} -eFz - \frac{e^2}{16\pi\epsilon_0 z} & \text{if } z > 0 \\ V_c(\mathbf{r}) & \text{if } z < 0, \end{cases} \quad (3.6)$$

where $V_c(\mathbf{r})$ is the periodic potential of the crystal lattice. From Equation 3.5, one can see immediately that the absorption of a photon relies on the existence of a non-uniform potential and, more specifically, a potential with a non-zero gradient in the direction of ϵ^t . This reflects the fact that a free electron cannot absorb a photon. If photon absorption happens due to the large gradient in V at the surface, then it is termed the surface photo-effect. Alternatively, the corrugation of the crystal potential in the bulk also allows photon absorption—this is called the (direct) bulk photo-effect.¹

The emission observed from tips is dominated by the surface photo-effect, which has a particularly simple polarization dependence [44]. This effect occurs due to the large gradient in V in the z -direction, and it follows that $M_{ij} \propto \epsilon^t \cdot \hat{z}$ and therefore the emitted current follows

$$J_{\text{surf}} \propto (\epsilon^t \cdot \hat{z})^2. \quad (3.7)$$

¹The term “direct” differentiates this from the “indirect” bulk effect, which includes higher order processes where the condition that energy and momentum be simultaneously conserved is satisfied through interaction with other particles, for example, the emission or absorption of phonons.

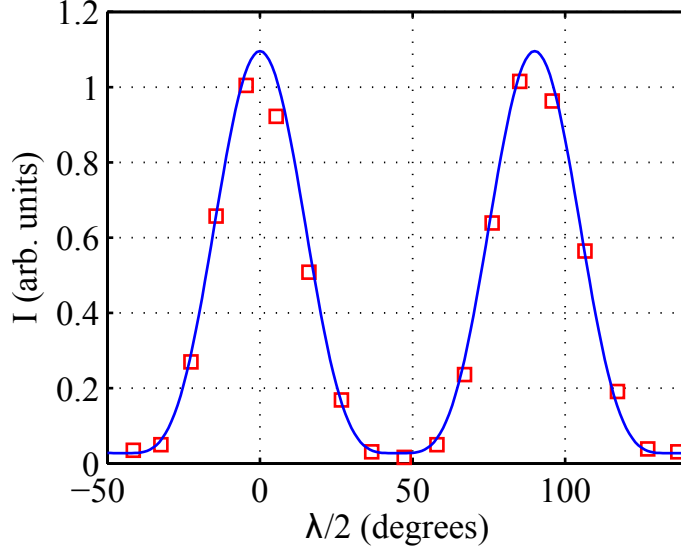


Figure 3.5: Laser-induced current vs. angle of half wave plate. Zero corresponds to polarization parallel to the tip axis. $U_{\text{tip}} = -414$ V, $P_{\text{avg}} = 71$ mW. The equation for the fitted curve is $y = 1.07 (\cos^2(\phi/2))^2 + 0.027$.

Generalizing to n -photon processes,

$$J_{\text{surf, } n} \propto (\epsilon^t \cdot \hat{z})^{2n}. \quad (3.8)$$

The expected polarization dependence of emission due to the bulk photo-effect is much more complex.²

Diffraction of the optical field by the tip leads to locally enhanced electric fields at the tip. Fields simulated by the finite element method [52] are plotted in Figure 3.7, assuming 800 nm light incident on a tungsten tip of radius 120 nm. The maximum field enhancement for this geometry is a factor of 2.1-2.2, depending on polarization. Field enhancement affects the number of electrons that will be excited at a given region of the tip, and can be used to select particular emission sites. A detailed

²To see this, we can write the crystal potential in terms of its fourier components, $V_c(\mathbf{r}) = \sum_{\mathbf{G}} V_{\mathbf{G}} \exp(i\mathbf{G} \cdot \mathbf{r})$. It follows that $M_{ij} = \sum_{\mathbf{G}} iV_{\mathbf{G}} (\epsilon^t \cdot \mathbf{G}) \langle \phi_j | \exp(i\mathbf{G} \cdot \mathbf{r}) | \phi_i \rangle$. Regrouping terms into a prefactor $a_{\mathbf{G}}$ for each reciprocal lattice vector, the direct photocurrent should have the form $J_{\text{bulk}} = \sum_{\mathbf{G}} a_{\mathbf{G}} (\epsilon^t \cdot \mathbf{G})^2$ for a one-photon process.

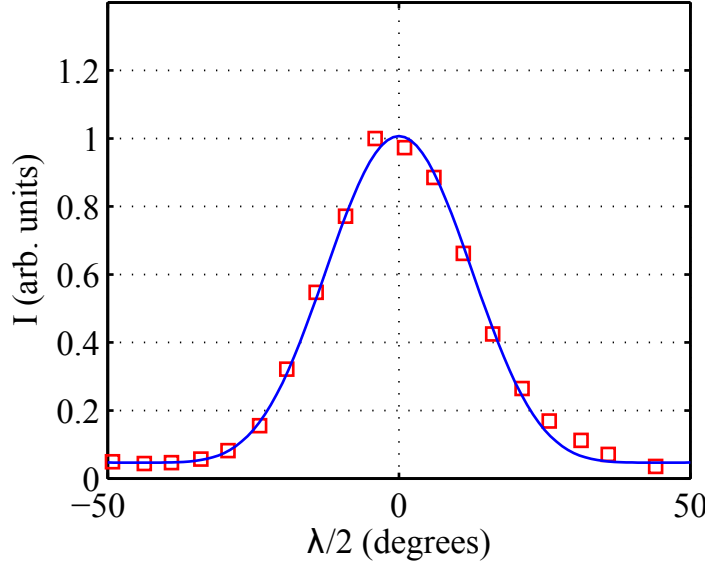


Figure 3.6: Laser-induced current vs. angle of half wave plate. Zero corresponds to polarizations parallel to the tip axis. $U_{\text{tip}} = -400$ V, $P_{\text{avg}} = 174$ mW. The equation for the fitted curve is $y = 0.72 (\cos^2(\phi/2))^3 + 0.3 (\cos^2(\phi/2))^2 + 0.05$.

study of this was performed by Yanagisawa et al. [53, 49], using a (011)-oriented tip, which has four off-axis emission spots. The tungsten tips used in the polarization-dependence measurements discussed above (Figures 3.5 and 3.6) are (111)-oriented, with a central emission spot on-axis and three off-axis emission spots. In cases where there are low work-function crystal planes in the region of the tip where enhancement is strong for perpendicular polarization (Figure 3.7(c)), the polarization dependence might be more complex than that in Figures 3.5 and 3.6.

3.1.4 Carrier-envelope phase dependence

It can be shown that the spectrum of a mode-locked laser takes the form of a frequency comb whose envelope is given by the spectrum of a single laser pulse, with peaks at frequencies

$$f_n = f_{\text{CEO}} + n f_{\text{rep}}, \quad (3.9)$$

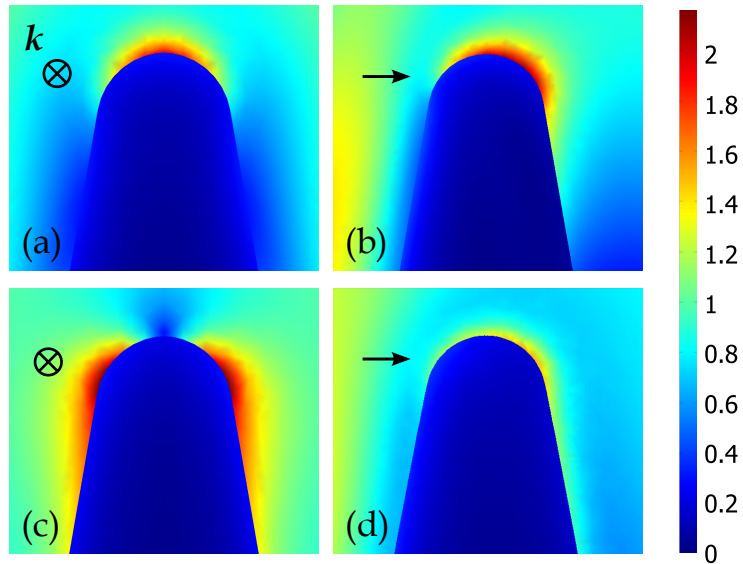


Figure 3.7: Field enhancement (amplitude of the electric field divided by the amplitude of the electric field of the incident wave), simulated by the finite element method. The tip simulated has a radius of curvature $r = 120$ nm, and the complex dielectric constant of tungsten at 800 nm is used. (a) and (b) show field enhancement for polarization parallel to the tip axis, while (c) and (d) show field enhancement for polarization perpendicular to the tip axis. In (a) and (c), the laser is propagating into the page. In (b) and (d), the laser comes from the left hand side (note that due to diffraction, the field amplitude is larger in the geometrical shadow of the tip). The cross sections are taken through the plane of symmetry of the tip, except for (d), where the plane is displaced by 60 nm from the axis of symmetry due to the fact that the strongest field enhancement is off-axis, as seen in (c).

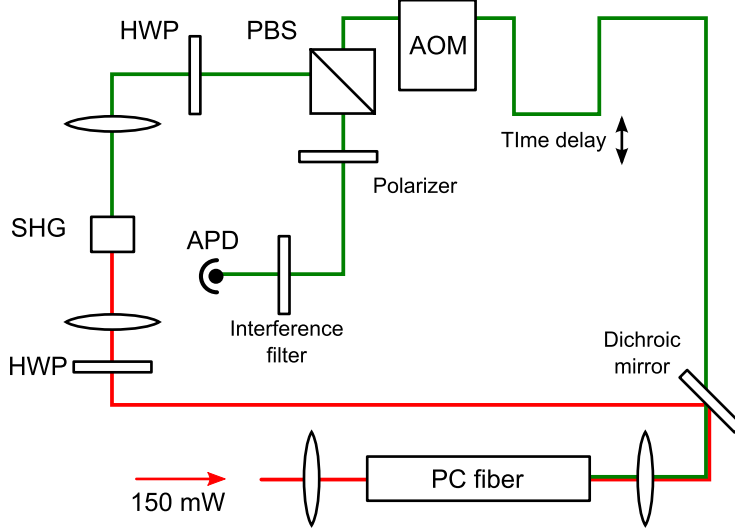


Figure 3.8: $f-2f$ interferometer. The spectrum of the laser is broadened in the photonic crystal (PC) fiber. A dichroic beamsplitter separates the high and low frequency parts of the spectrum. The frequencies in the lower part are doubled in a non-linear crystal. A time-delay in one arm is used to ensure temporal overlap of the two arms. An acousto-optic modulator (AOM) shifts the frequency by 90 MHz, which allows f_{CEO} to be locked to zero. The PBS followed by a polarizer overlaps the two arms on the avalanche photodiode (APD). With the half-wave plate (HWP), PBS, and polarizer, the power of the individual arms can be adjusted. The interference filter removes comb-lines that don't contribute to the beatnote.

where n is an integer and f_{rep} is the repetition rate of the laser, and f_{CE} is the rate of change of the carrier-envelope phase. The carrier-envelope frequency, f_{CEO} can be measured with an $f-2f$ interferometer, which frequency doubles the lower frequency comb lines and interferes them with the higher frequency comb lines. This generates a beat at the frequency f_{CEO} that can be measured with a photodiode (Fig. 3.8). An acousto-optic modulator (AOM) in one arm of the interferometer shifts the frequency of that arm by 90 MHz. This shifts f_{CEO} by the same amount, allowing it to be locked to zero if desired. The beatnote can be phase-locked to a reference frequency by feeding back on the pump power of the Ti:Sapph oscillator. This is accomplished using an AOM in the pump beam. Modulation depth is defined as

$$m_{\text{CE}} \equiv \frac{I_{\max} - I_{\min}}{I_{\max} + I_{\min}} \quad (3.10)$$

With f_{CEO} and f_{rep} locked, we looked for a modulation of the photocurrent at f_{CEO} with the DC bias voltage adjusted from 0.35 GV/m to 2 GV/m. In this range, the experiment should have been sensitive to a 0.1% modulation of the photocurrent, but we were unable to find a signal. We concluded that this number represents an upper bound to m_{CE} in this range.

3.1.5 Numerical integration of TDSE

The optical field emission model predicts that the current will be a function of carrier-envelope phase. A fit based on Eq. 2.38 to the autocorrelation data of Fig. 3.4 yields a laser electric field of 1.8 GV/m. For the parameters of the fit, the predicted CE phase modulation depth is 0.5%. To understand why the modulation depth is actually smaller than this, we needed to develop a model for the intermediate keldysh regime, which is more appropriate to our experiment.

We developed a simple model based on integrating the time-dependent Schrödinger equation in one dimension. The model considers the evolution of a single electron state, which is initialized as a localized wavefunction (something like a surface state). The energy of this state is adjusted to be equal to the Fermi energy for tungsten. Then, the state is numerically evolved under the influence of the time-dependent potential using the Crank-Nicolson method.

Explicitly, the potential is

$$V(z, t) = \begin{cases} \infty, & \text{if } z < -L \\ -13.5 \text{ eV}, & -L < z < \delta \\ -(e^2/(16\pi\epsilon_0 z)) - ez(F_{\text{DC}} + F_{\text{laser}}(t)), & \text{if } z > \delta \end{cases} \quad (3.11)$$

As written, $V = 0$ corresponds to the Fermi level. The number $\delta \gtrsim 0$ is used to avoid the singularity of the image potential at $z = 0$; it's chosen so that $V(z)$ is continuous. An imaginary potential is included near the right hand boundary of the simulation

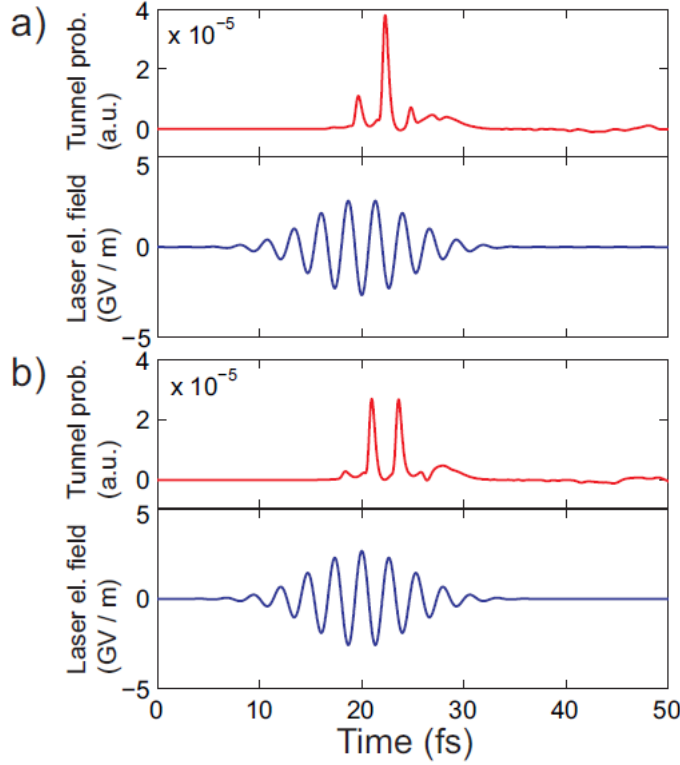


Figure 3.9: Results of 1D Schrödinger model. DC field 0.2 GV/m. The emission profile is qualitatively different for two values of carrier envelope phase: in (a), a single 700 attosecond electron spike occurs, in (b), which was simulated with the CE phase shifted by 180° , the result is two sub-optical cycle spikes. Reproduced from [54] ©2006 IEEE.

to act as an absorber and prevent reflections from the boundary. The laser field is given by

$$F_{\text{laser}}(t) = F_0 \exp(-2 \log(2)t^2/\tau^2) \cos(\omega t + \phi), \quad (3.12)$$

which represents a gaussian pulse with peak field F_0 , CE phase ϕ , and FWHM τ . To determine the initial state, the field is turned off, and imaginary-time integration was used to find the ground state of the potential. The width of the box, L , is chosen so that the energy of the state matches the Fermi energy. The emission probability is determined by calculating the probability flux outside the barrier, at $z = 2$ nm.

The simulation was used to model the peak-to-baseline ratio as a function of tip bias, under the experimental parameters corresponding to the data of Fig. 3.4; the result is the solid blue line plotted in that figure. Given the simplicity of the model, the agreement with the data seems quite good.

Figure 3.10 displays the simulated modulation depth as a function of DC field and laser pulse fluence. The pulse fluence in the experiment was 4 mJ/cm^2 , neglecting optical field enhancement. With optical field enhancement, the effective fluence could be as high as 0.04 J/cm^2 . For a 3-cycle pulse, the simulation predicts that the modulation depth is always below 0.4%. For the range of parameters accessible in the experiment, the modulation depth is below our detection limit of 0.1%, with the exception of very small bias fields. At such low bias fields, the laser-induced current, and therefore the detection limit, is reduced. The results of our numerical model are consistent with theoretical work that has been done in the analogous $\gamma_K \sim 1$ regime in atoms [55]. Ultimately, the picture of sub-optical cycle electron emission from tips was confirmed by the beautiful work of Peter Hommelhoff's group at MPQ [10], which showed that sub-optical spikes similar to the ones predicted in Figure 3.9 can be distinguished in the energy domain: two spikes emitted one period apart interfere in the energy domain, leading to a modulation at the photon energy, whereas a single spike does not [10].

3.2 Laser-triggered emission from Hafnium Carbide tips: multiphoton emission vs. thermally-assisted field emission

The behavior of non-equilibrium electron distributions following optical excitation of a solid has implications for many processes of practical interest, including laser-ablation [56] and ultrafast magnetic switching [57]. Clearly, it also has implications for electron emission and, in particular, the time-scale of emission following photo-excitation. The optical energy absorbed by the material directly excites the electrons, creating a non-equilibrium distribution. Electron-electron scattering leads to thermalization of the

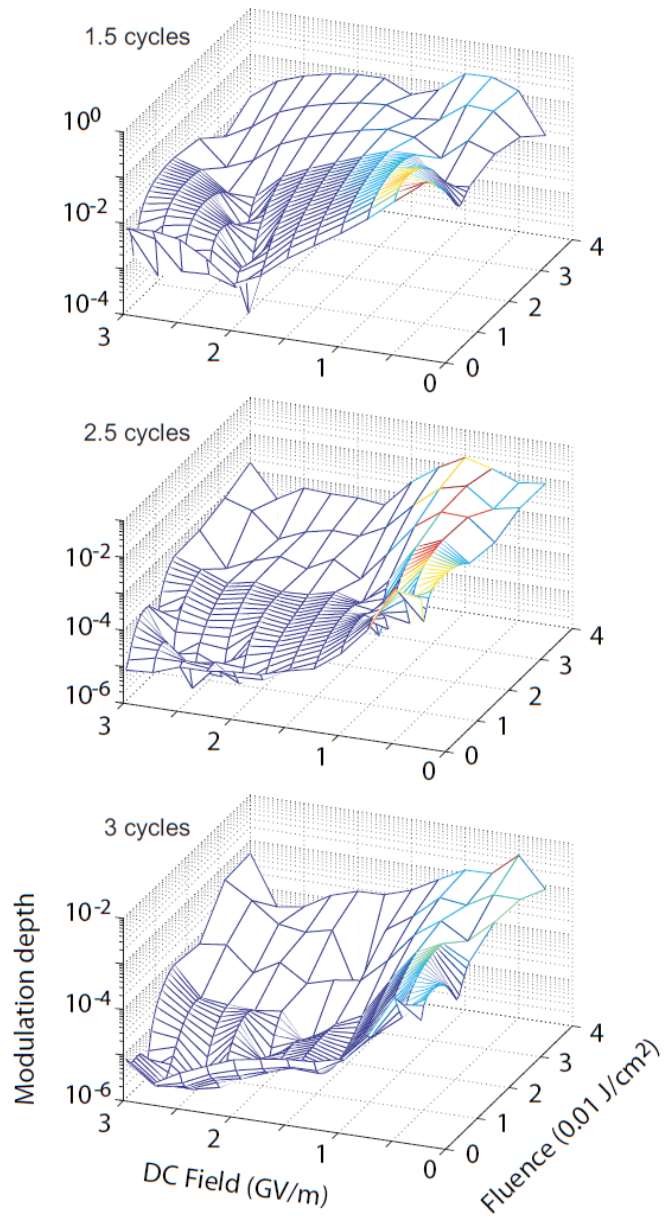


Figure 3.10: Simulated CE phase modulation. The modulation depth is plotted as a function of laser fluence and DC field for three different pulse durations. Reproduced from [54] ©2006 IEEE.

electron gas, while electron-phonon scattering leads to equilibration of the electrons with the lattice. Electron-phonon coupling usually happens on an approximately picosecond time-scale; if this is slower than the electron thermalization, then the electron and lattice can be described by two separate temperatures, in what is known as the two-temperature model [58]. The dynamics of both of these processes are complex, and the thermalization time can depend on the degree of excitation [59].

This section considers the tradeoff between laser-induced heating and multiphoton emission in Hafnium carbide. The low thermal conductivity of Hafnium carbide makes it a good candidate for observing effects of laser-induced heating. However, we found that, though we could obtain thermal-assisted field emission, this led to an increase in the DC current and did not have a measurable pulsed component. By studying the scaling of multiphoton emission and thermal-assisted field emission, we could estimate the range of parameters where transient (or pulsed) thermal-assisted field emission becomes important.

3.2.1 Characterization of emission processes

The current-voltage characteristic of the Hafnium Carbide tip under laser illumination manifests two distinct emission regimes: multiphoton emission, and thermal-assisted field emission. The apparatus used to measure the laser-induced current is similar to that described above (Section 3.1.1). The tip is a commercially manufactured (310)-oriented hafnium carbide tip (Applied Physics Technologies, McMinnville, OR), with a radius of curvature of 120 nm. The work function of (310)-oriented HfC is 3.4 eV [60]. The laser is focused to a $2.7 \mu\text{m}$ waist using a 4.5 mm focal length mirror inside the vacuum chamber, and the beam-line is again dispersion compensated. An extraction aperture is placed 1.5 mm from the tip apex, and a bias voltage (U_{tip}) is applied between the tip and this extractor. Electrons that pass through the extractor are detected with a microchannel plate (MCP).

When an electron strikes the wall of a channel of the MCP, the electron triggers an avalanche process with gain varying from 10^4 to 10^7 depending on the bias voltage applied across the plates (U_{mcp}). This dependence can be measured with respect to

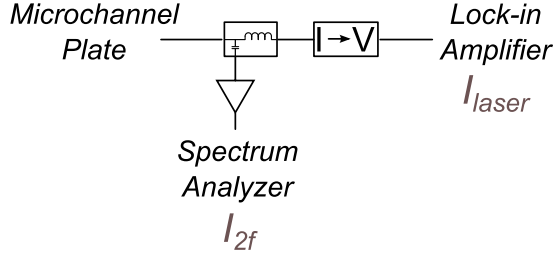


Figure 3.11: I_{laser} and I_{2f} . Current flowing to the front of the MCP is detected. The MCP consists of two plates in a chevron configuration. The front of the MCP is grounded through the current to voltage preamplifier; a bias voltage (not shown) is applied to the back of the second plate and determines the gain of the detector. The laser beam to the tip is chopped at a low frequency (< 400 Hz), and the average laser-induced current (I_{laser}) is detected with a lock-in amplifier. The component of the current at twice the repetition frequency of the laser is detected as a proxy for the pulsed component of the current (I_{2f}).

the gain at a particular value of U_{mcp} , and absolute gain of the MCP was calibrated by counting electron detection events at some value of U_{mcp} . Combining these two measurements, the following calibration of the gain of our MCP as a function of U_{mcp} was determined:

$$G = \exp(92.83 - 0.2737U_{\text{mcp}} + (2.8199 \times 10^{-4})U_{\text{mcp}}^2) \quad (3.13)$$

$$- (1.1708 \times 10^{-7})U_{\text{mcp}}^3 + (1.7447 \times 10^{-11})U_{\text{mcp}}^3). \quad (3.14)$$

A bias tee splits the current from the front of the MCP into high-frequency and low-frequency components. The laser triggering emission from the tip is chopped at a low frequency (< 400 Hz) and the component of the current that was induced by the laser is lock-in detected. The high frequency component consists of harmonics of the laser repetition rate. For the I-V curves shown, we measured both the lock-in detected current, which we call I_{laser} , and the component of the signal at $2f_{\text{rep}}$, which will be referred to as I_{2f} (Fig. 3.11) when converted to an equivalent average current. The former represents average laser-induced current, while the latter loosely represents the pulsed component of the signal (i.e. emission that is short compared

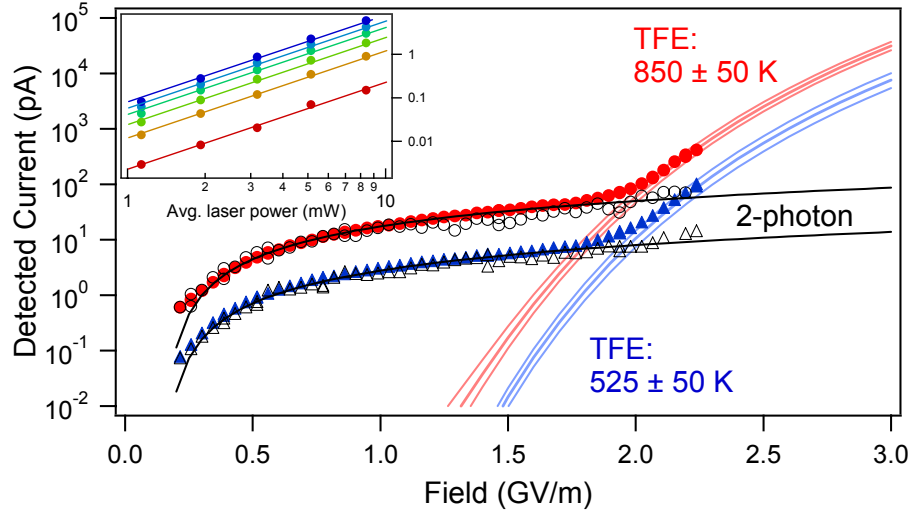


Figure 3.12: Closed symbols are I_{laser} and open symbols are I_{2f} . The laser power is 3.9 mW (triangles) and 9 mW (circles), with corresponding peak intensity in the focus (neglecting field enhancement) 2.1×10^{10} and $4.9 \times 10^{10} \text{ W/cm}^2$. The solid lines show theory curves: light solid lines are thermal-assisted field emission, and dark solid lines are two-photon emission. The inset shows I_{laser} vs. laser power for several bias voltages in the two-photon regime. The current in this regime is always proportional to the square of the laser power. Adapted from [43] ©2012 APS.

with the time between laser pulses).

Figure 3.12 shows the measured I - V relation at two example values for the incident laser power. At low tip voltage, I_{laser} and I_{2f} closely follow one another, showing that the laser-induced current is all modulated at the laser repetition rate. However, at large bias voltages, I_{laser} and I_{2f} diverge, as the emitted current becomes dominated by thermal-assisted field emission due to laser-induced heating of the tip. From Equation 2.37, in the limit that $k_B T \ll (2\hbar\omega - \phi_{\text{eff}})$, the current due to two-photon emission is

$$I_{2-\text{ph}} \propto P^2 [2\hbar\omega - \phi + \sqrt{eF/(4\pi\epsilon_0)}]^2. \quad (3.15)$$

The dark solid lines in Figure 3.4 are fits of this model to the I_{2f} data (note that the condition $k_B T \ll (2\hbar\omega - \phi_{\text{eff}})$ may fail at very low bias voltages). The photon energy is left as a free parameter for the fit; the best-fit value (curves in Fig. 3.12) is 1.46 eV. This model neglects the width of the energy spectrum (a more precise model might

be obtained by taking a convolution over the energy spectrum), but the fitted 1.46 eV photon energy is reasonably close to the center energy of the spectrum. At a fixed tip voltage, the laser-induced current is proportional to the square of the laser power, as expected for a two-photon process (inset to Fig. 3.12).

The light solid curves are the predicted difference in thermal-assisted field emission between the elevated temperature and room temperature. They are determined numerically based on a fit to the measured DC emission I - V relation, as discussed in Section 2.1.4. From this, we infer that the temperature of the apex of the tip is 525 ± 50 K and 850 ± 50 K for 3.9 and 9 mW illumination, respectively.

In all of our measurements, we never saw evidence of significant transient thermal-assisted field emission. The I_{2f} at two values of laser power display a constant ratio over the entire range of tip-bias measured (Fig. 3.12). In contrast, thermal-assisted field emission has a complex dependence on temperature and bias field (Fig. 2.3) and would not maintain a constant current ratio as the tip-voltage varies.

The electron gas must be superheated for a short time following the absorption of the laser pulse, and this must lead to higher rates of thermal-induced emission. However, since the multiphoton emission theory perfectly matches the measured pulsed current I_{2f} , we must conclude that transient thermal-assisted field emission is negligible with respect to multiphoton emission over the explored parameter space. Note that this is true even where I_{laser} and I_{2f} diverge and the thermal-assisted field emission per pulse is much larger than I_{2f} . In this regime, average thermal-induced emission dominates multiphoton emission because, though the instantaneous current due to thermal-assisted field emission is smaller than the instantaneous multiphoton emission current, the former is non-zero for the entire duration of the time between successive laser pulses, which is nearly 6 orders of magnitude larger than the laser pulse duration.

In the multiphoton-emission-dominated regime, the emission pattern is more diffuse than for DC field emission and thermal-assisted field emission (Fig. 3.13). This occurs because multiphoton emission is less sensitive to differences in work function than field emission.

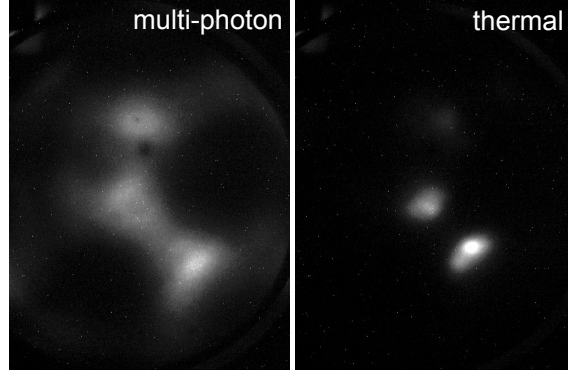


Figure 3.13: Emission pattern for multiphoton and thermal or DC field emission. Reproduced from [43] ©2012 APS.

Polarization dependence of the emission was studied. As for tungsten, the emission is maximized for polarization parallel to the tip, and the behavior is consistent with the discussion in Section 3.1.3, except that for HfC we expect the two-photon process to dominate. In Section 3.2.2, it will be shown that transient temperature rise is larger for parallel polarization than for perpendicular polarization, so that thermal-assisted field emission would also differ for the two polarizations. Figure 3.14(a) shows current as a function of bias field for polarization parallel and perpendicular to the tip shank. Note that I_{2f} maintains a constant ratio for parallel and perpendicular polarization, consistent with two-photon emission but inconsistent with thermal-assisted field emission.

As the laser is moved up the shank of the tip, the steady-state apex temperature initially increases as more energy is absorbed by the tip (Fig. 3.14). The result is that for bias fields above ≈ 0.5 GV/m, the average current is much larger when the laser is mis-aligned up the shank. Below 0.5 GV/m, the average current is largest when the beam is aligned to the apex, because here the average current is dominated by multiphoton emission. This gives a practical method to guarantee that the alignment is at the apex: regardless of the parameters of the experiment, the alignment is first optimized at low tip bias where multiphoton emission dominates.

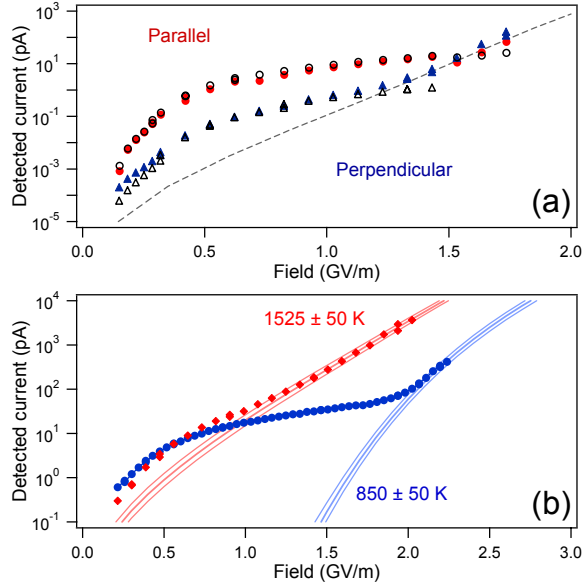


Figure 3.14: Influence of polarization and mis-alignment on multiphoton and thermal-assisted field emission. All data shown is measured with 9 mW average laser power. (a) Circles (triangles) represent current for polarization parallel (perpendicular) to the tip axis. Closed symbols are I_{laser} , and open symbols are I_{2f} . The dashed line is the calculated thermal-assisted field emission for this tip, assuming a temperature of 1100 K. (b) Aligning the laser 2–3 μm up the shank of the tip increases the apex temperature. Blue circles are I_{laser} with laser aligned to the tip apex. Red diamonds are measured under the same conditions, except that the laser has been aligned further up the shank. Light solid lines are DC TFE theory. Note that the data goes below the blue curve at low field; this is because emission there is dominated by multiphoton emission, which is maximized when the beam is aligned to the apex of the tip. Reproduced from [43] ©2012 APS.

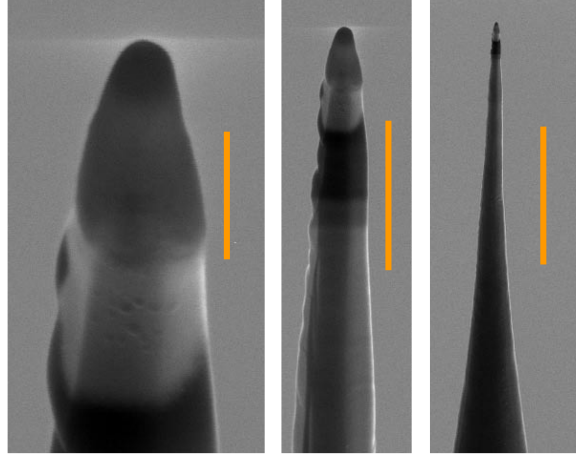


Figure 3.15: SEM images of HfC tip, viewed at a 45 degree angle. From left to right, the scale bars are 0.5, 2, and 10 μm . Reproduced from [43] ©2012 APS.

3.2.2 Model of heating and thermal conduction in the tip

A finite element model of heat deposition and thermal conduction in the tip was developed. The model predicts the transient temperature rise of the tip, and therefore lets us determine the relative magnitude of thermal emission and multiphoton emission outside the range of parameters that could be explored experimentally.

The model is broken into three parts that build on one another. The first part calculates the optical field enhancement at the tip apex and the energy density deposited in the tip by the laser pulse. The second part calculates the average temperature rise of the tip under continuous illumination, which approximates the average temperature of the tip under pulsed illumination. The final part calculates the temperature evolution immediately after the incident laser pulse, including thermal conduction and the equilibration of the electron and phonon temperatures. The initial temperature distribution in the tip is taken from the second part.

The tip geometry for the simulation is an approximation of the geometry of the Hafnium carbide tip studied in the previous section. SEM images of this tip are shown in Figure 3.15. The simulated tip has a radius of curvature of 120 nm. The initial opening angle is 10 degrees (half angle), decreasing to a 2.5 degree half angle,

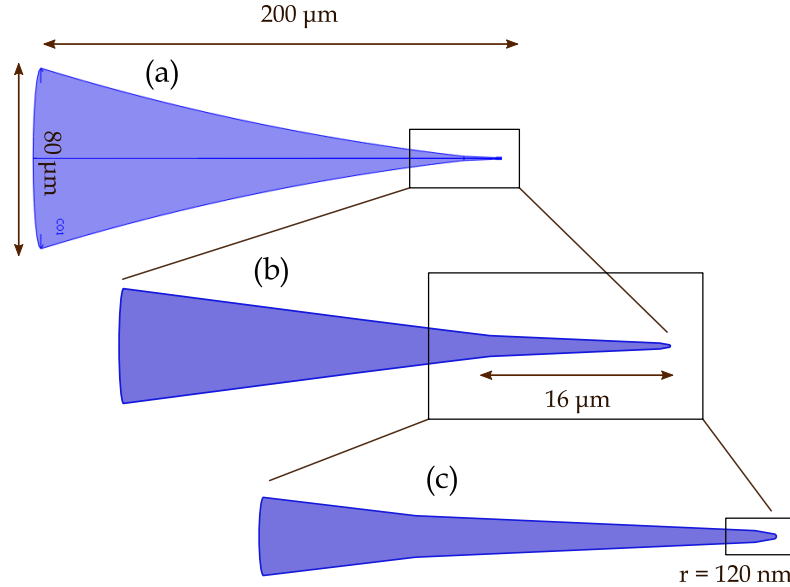


Figure 3.16: Geometry of tip in finite-element simulation. The final box (image (c)) indicates the part of the tip shown in the electromagnetic simulation results (Fig. 3.18).

as shown in Figure 3.16. At $16 \mu\text{m}$ from the apex, the cone begins to slowly flare out to a $500 \mu\text{m}$ cylinder. In the region of continuously increasing opening angle, the geometry is such that a cross section of the tip profile coincides with a circle of $250 \mu\text{m}$ radius.

Material parameters used for the simulations described in this Section are summarized in Table 3.1, reproduced from [43]. HfC material parameters are not tabulated as often as those of tungsten and gold, and in some cases the reported values were contradictory. The temperature-dependent electronic heat capacity of HfC was determined by integrating the density of states from Ref. [64]. Defining the electron energy in the metal as ε and the chemical potential as μ , the Fermi distribution function is

$$f(\varepsilon, \mu, T_{\text{el}}) = \frac{1}{\exp((\varepsilon - \mu)/k_B T_{\text{el}}) + 1}, \quad (3.16)$$

Table 3.1: Materials properties used for modeling (Adapted from [43] ©2012 APS)

	T (K)	HfC	W	Au
C (10^6 J/(m ³ K)) ^[61, 62, 63]	300	2.29	2.55	2.48
	1000	3.48	2.89	2.88
C_{el} (10^4 J/(m ³ K)) ^[64, 65]	300	3.81 ^a	3.46	2.02
	1000	8.42 ^a	9.88	6.73
κ (W/(m K)) ^[66, 67]	300	20.7	171	317
	1000	27.0	117	270
$\kappa_{\text{el},0}$ (W/(m K)) ^[67, 68]	— ^b	136 ^c	318	
$g_{\text{el-ph}}$ (10^{16} W/(m ³ K)) ^[65]		6.85 ^d	19.1	2.61
ϵ_r [69, 67, 70]	Re[]	9.49 ^e	5.2	-24
	Im[]	-8.48 ^e	-19.4	-1.5
β (\parallel polarization)		0.8	0.6	0.037
β (\perp polarization)		0.95	0.7	0.047

^a HfC $C_{\text{el}}(T)$ determined from the density of states in Ref. [64].

^b For HfC, κ_{el} and κ_{ph} were taken to be 12 W/(m K), half of κ at 630 K, the approximate initial temperature (see text).

^c W κ_{el} at 400 K determined by fitting electrical resistivity and thermal conductivity data in the 300-900 K range (Ref. [67]) using the Wiedemann-Franz law.

^d Example value used in HfC TTM model.

^e Determined by Drude model fit to reflectivity curves in Ref. [69] using two Lorentz oscillator terms.

and the electronic heat capacity is

$$C_{\text{el}}(T_{\text{el}}) = \int_{-\infty}^{\infty} \frac{\partial f(\varepsilon, \mu, T_{\text{el}})}{\partial T_{\text{el}}} g(\varepsilon) \varepsilon d\varepsilon, \quad (3.17)$$

where $g(\varepsilon)$ is the density of states. The chemical potential, μ depends on the electron temperature and is determined from the condition that the total number of electrons N_{el} is fixed:

$$N_{\text{el}} = \int_{-\infty}^{\infty} f(\varepsilon, \mu(T_{\text{el}}), T_{\text{el}}) g(\varepsilon) d\varepsilon. \quad (3.18)$$

The Drude-Lorentz model is often used as a phenomenological model for the dielectric constant of metal and semiconductor materials in the IR and visible range [71]. The Drude or free-electron part is due to intraband transitions, while one or more oscillator terms may be used to take into account inter-band transitions. The model takes the form

$$\epsilon_r(\omega) = \epsilon_{\text{Drude}}(\omega) + \sum_j \epsilon_{\text{Lorentz}, j}(\omega), \quad (3.19)$$

where

$$\epsilon_{\text{Drude}}(\omega) = \epsilon_{\infty} \left(1 - \frac{\omega_p^2}{\omega^2 + i(\omega\Gamma_0)} \right) \quad (3.20)$$

and

$$\epsilon_{\text{Lorentz}, j}(\omega) = \frac{\omega_{p,j}^2}{\omega_j^2 - \omega^2 - \Gamma_j}. \quad (3.21)$$

The parameters of the Drude component are ϵ_{∞} , ω_p , and Γ_0 are the asymptotic value of ϵ_r , the plasma frequency, and the relaxation rate. Each oscillator is described by three parameters: ω_j and Γ_j are the frequency and damping rate of the resonance, and $\omega_{p,j}$ is related to the oscillator strength.

Ref. [69] presents the reflectivity of HfC as a function of wavelength. We can find the parameters of the phenomenological model by fitting the reflectivity data, using the relation between the complex dielectric constant and permittivity. The real and imaginary parts of the complex index of refraction, n , and k , can be determined from the complex permittivity

$$n_c = n + ik = \sqrt{\epsilon_r}. \quad (3.22)$$

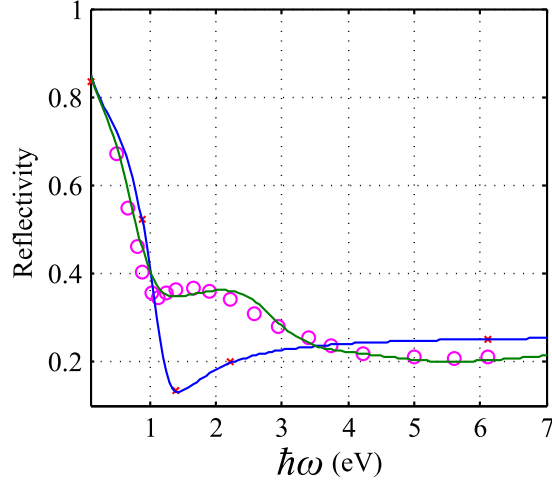


Figure 3.17: Magenta circles are reflectivity data for $\text{HfC}_{0.98}\text{N}_{0.02}$ from [69]. Red crosses are the fitted Drude model contribution to the reflectivity, also from [69]. Solid lines are my fit to the reflectivity data and the resulting Drude-only reflectivity.

ϵ_∞	10.2	$\hbar\omega_{p,1}$	5.9 eV	$\hbar\omega_{p,2}$	6.8 eV
$\hbar\omega_p$	1.22 eV	$\hbar\omega_1$	2.2 eV	$\hbar\omega_2$	4 eV
$1/\Gamma_0$	1.9 fs	$\hbar\Gamma_1$	4.4 eV	$\hbar\Gamma_2$	17.7 eV

Table 3.2: Fit parameters for HfC complex permittivity reconstructed from data in [69]

The reflectivity at normal incidence at the metal-vacuum interface is

$$R = \frac{(n - 1)^2 + k^2}{(n + 1)^2 + k^2}. \quad (3.23)$$

In this approach, a model with a rather large number of free parameters is used. However, its form is physically motivated, and the resulting complex permittivity satisfies physical constraints such as the Kramers-Kronig relations. Ref. [69] provides only some of the parameters of the fit. I fit the Drude-Lorentz model to their data to obtain the remainder of the parameters and determine the complex permittivity. Fig. 3.17 shows the reconstruction of their fit. The parameters are in Table 3.2.

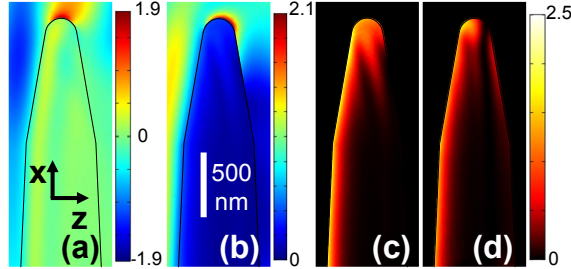


Figure 3.18: Finite element model of optical fields near tip. The amplitude of the incident wave is 1 V/m. The wavelength is 800 nm. (a) E_x at the phase that maximizes it. (b) Cycle-averaged magnitude of the electric field, x -polarization. (c), (d) Average power density deposited in the tip , for x - and y - polarized light, respectively. Electric field units are V/m and power density units are 10^4 W/m³. All plots are for the cross section given by the symmetry plane ($y = 0$) of the model. Reproduced from [43] ©2012 APS.

Electromagnetic fields

Figure 3.18 shows the calculated electric fields for parallel polarization, as well as the power density deposited in a HfC tip, for both parallel and perpendicular polarization. The model assumes continuous wave illumination at 800 nm. The calculation was repeated for 680 nm and 940 nm wavelengths, and the deposited power changed by less than 10%. Figure 3.19 compares the field enhancement and energy deposited in tips of three different materials, HfC, W, and Au, illuminated with light polarized parallel to the tip axis. Although the degree and distribution of field enhancement is similar for the three materials, the skin depth and total energy deposited are very different. The field distribution for parallel and perpendicular polarization are compared in Figure 3.7.

Continuous heating model

The electromagnetic model supplies a power density deposited in the tip as a function of position, $p_{\text{model}}(x, y, z)$. By computational necessity, the electromagnetic model is solved over a smaller region than is required for the full thermal model. We defined the heat source in the continuous heating model as a combination of the electromagnetic

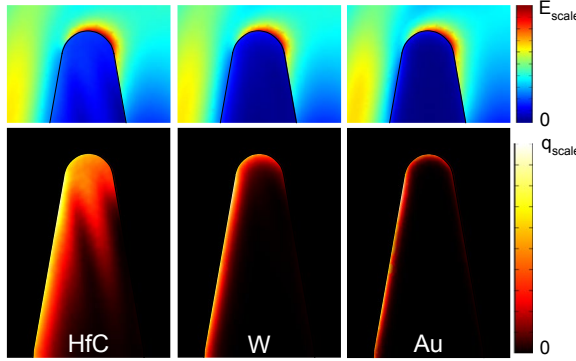


Figure 3.19: Comparison of electromagnetic model results for HfC, W, Au. Top: cycle-averaged electric field strength for 1 V/m incident plane wave at 800 nm. The optical field is polarized parallel to the axis of the tip. E_{scale} is 2.1, 2.2, and 2.4 V/m for HfC, W, Au respectively. Bottom: Energy density deposited by a single 30 pJ laser pulse focused to 2.7 μm (this corresponds to 4.6 mW average power at a 150 MHz repetition rate). $q_{\text{scale}} = 5.0, 8.5, \text{ and } 0.8 \times 10^7 \text{ J/m}^3$ for HfC, W, Au respectively. Reproduced from [43] ©2012 APS.

model result and an analytic approximation. The heat source term has the form

$$p(x, y, z) = \begin{cases} p_{\text{apex}}(x, y, z), & x < 1.5 \text{ } \mu\text{m} \\ p_{\text{shank}}(x), & x > 1.5 \text{ } \mu\text{m} \end{cases} \quad (3.24)$$

where

$$p_{\text{apex}}(x, y, z) = p_{\text{model}}(x, y, z) e^{-2(x/w_0)^2} \quad (3.25)$$

and

$$p_{\text{shank}}(x) = \frac{4\beta_p P_0}{\pi w_0^2 r(x)} e^{-2(x/w_0)^2}, \quad (3.26)$$

where $r(x)$ is the radius of the shank at the co-ordinate x (the x -axis is taken along the symmetry axis of the tip). As p_{model} was calculated for a plane wave, it has been multiplied by a gaussian envelope to simulate the 2.7 μm waist used in the experiment. The expression for p_{shank} is simply the power intercepeted by the tip cross section, modified by a single “fudge-factor”, β_p , that encompasses the material reflectivity and any diffraction or field enhancement effects [72]. The value of β_p is

determined by requiring the integrated power deposited in a slice of the tip at constant x to be continuous at $x = 1.5 \mu\text{m}$.

The data of Figure 3.12 show a temperature rise of $225 \pm 50 \text{ K}$ and $550 \pm 50 \text{ K}$ for average laser power of 3.9 mW and 9 mW , respectively. The continuous heating model predicts 260 K and 570 K , which is in good agreement. A simple analytic model for the temperature rise is given in [73]:

$$\Delta T \approx \frac{\sqrt{2}\beta_p P_0}{\pi^{3/2}\kappa w_0\theta}, \quad (3.27)$$

where P_0 is the incident laser power, κ is the thermal conductivity of the material, and θ is the half-angle of the tip cone (note that this assumes a simple conical geometry for the tip). Using $\theta = 2.5$ degrees and $\beta_p = 0.95$ (determined from the electromagnetic model) this simple model predicts temperature increases of 300 K and 700 K for the two example values of the laser power.

Transient two-temperature model

For the transient model, we must take into consideration the fact that energy from the laser is deposited only into the electron gas, not the phonon lattice [58]. The electron and lattice temperatures T_{el} and T_{ph} can be described by coupled equations

$$C_e \frac{dT_{\text{el}}}{dt} = \nabla \cdot (\kappa_{\text{el}} \nabla T_{\text{el}}) - g_{\text{el-ph}}(T_{\text{el}} - T_{\text{ph}}) + p(x, y, z)f(t) \quad (3.28)$$

$$C_{\text{ph}} \frac{dT_{\text{ph}}}{dt} = \nabla \cdot (\kappa_{\text{ph}} \nabla T_{\text{ph}}) + g_{\text{el-ph}}(T_{\text{el}} - T_{\text{ph}}). \quad (3.29)$$

The heat source has been multiplied by the temporal profile of the laser pulse, $f(t)$. Since the duration of the laser pulse is considerably shorter than the timescale of the temperature dynamics, the temporal profile used for the model is a square pulse with a constant value for $0 \leq t \leq 10 \text{ fs}$. $C_{\text{el,ph}}$ and $\kappa_{\text{el,ph}}$ are respectively the heat capacity and thermal conductivity of the electron and phonon gas. These can be functions of position and time due to their dependence on T_{el} and T_{ph} . The electron-phonon coupling constant, which governs the equilibration between the two heat reservoirs, is $g_{\text{el-ph}}$.

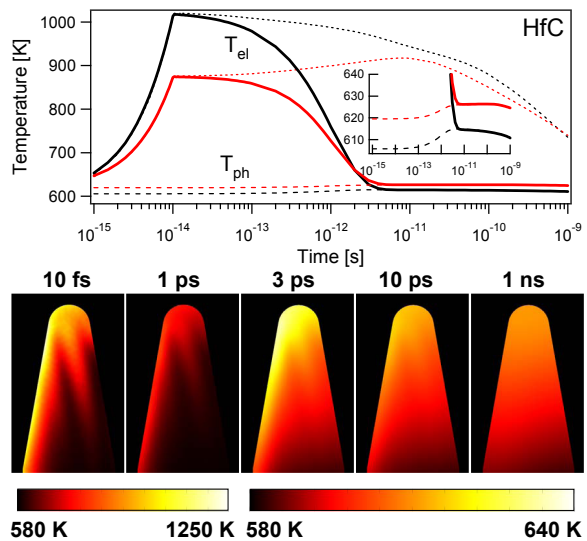


Figure 3.20: Two-temperature model results for Hafnium Carbide. Black curves are for parallel polarization, and red curves are for perpendicular polarization. Thick solid curves are the electron temperature, T_{el} , and thin dashed curves are T_{ph} . The thin dotted curves show the evolution of T_{el} with electron-phonon coupling turned off. The inset is rescaled to show the region where the two temperatures come to equilibrium. Lower plots: the electron temperature distribution in the cross-section where $y = 0$ at several times after the laser pulse. Reproduced from [43] ©2012 APS.

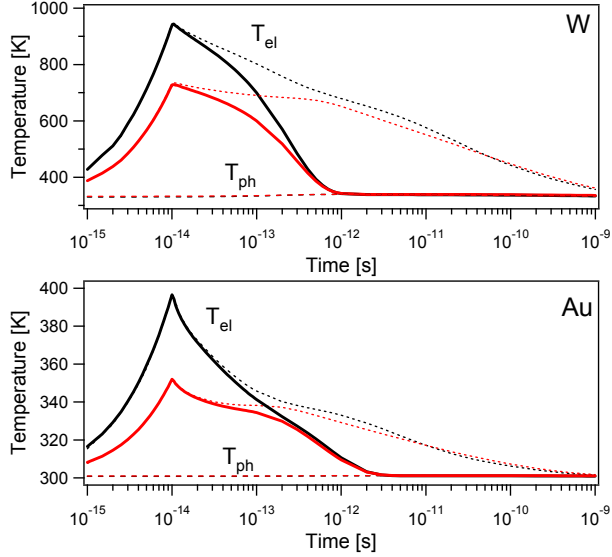


Figure 3.21: Two-temperature model results for Tungsten and Gold. The model geometry and laser parameters are the same as for the HfC model. Black curves are for parallel polarization, and red curves are for perpendicular polarization. Thick solid curves are the electron temperature, T_{el} , and thin dashed curves are T_{ph} . The thin dotted curves show the evolution of T_{el} with electron-phonon coupling turned off. Reproduced from [43] ©2012 APS.

Figure 3.20 shows the simulated temperature evolution for the Hafnium Carbide tip illuminated by 4.6 mW average power, 150 MHz repetition rate pulse train. As the initial condition, T_{el} and T_{ph} were taken to be equal to the result of the continuous heating model, with 4.6 mW incident power. As we were unable to find values of the electron thermal conductivity of Hafnium Carbide, we assumed that the electron thermal conductivity was half of the total thermal conductivity, which is the case for the similar material, TiC. We also could not determine an accurate value of the electron-phonon coupling constant, so we assumed $g_{\text{el-ph}} = 6.85 \times 10^{16} \text{ W/(K m}^3\text{)}$, independent of temperature. This corresponds to a coupling time $\tau_{\text{el-ph}} \sim C_{\text{el}}/g_{\text{el-ph}} \sim 1 \text{ ps}$, which is the expected order of magnitude (see [74]). The dotted curves show the evolution of T_{el} and T_{ph} in the absence of electron-phonon coupling. Cooling of the electron gas by conduction alone is orders of magnitude slower than reasonable electron-phonon coupling times; the electron-phonon coupling time therefore sets the time-scale of the thermal transient.

Figure 3.21 shows the analogous simulation for tungsten and gold tips. The laser parameters are the same as for the hafnium carbide model. The electron thermal conductivity of W and Au are expanded as [56]

$$\kappa_{\text{el}}(T_{\text{el}}, T_{\text{ph}}) = \kappa_{\text{el},0} \frac{T_{\text{el}}}{T_{\text{ph}}}, \quad (3.30)$$

with values for $\kappa_{\text{el},0}$ given in Table 3.1. The electron-phonon coupling constant is itself a function of the electron and lattice temperatures. For constant lattice temperature, the electron-phonon coupling constant can increase dramatically with T_{el} , and it is crucial to take this into account [65]. For the small pulse fluence modeled here, the temperature rise is not large enough to require this, and the values of $g_{\text{el},\text{ph}}$ in the table were obtained from the calculation of Ref. [65], averaged over the approximate temperature range of the simulation.

The tungsten κ_{el} was determined by fitting electrical resistivity and thermal conductivity data in the 300–900 K range (Ref. [67]) using the Wiedemann-Franz law.

3.2.3 Estimated transient thermal emission from HfC

In the current experiment, it is not possible to increase the laser power significantly above 12 mW, as the baseline temperature rise of the tip is so large that there is significant DC thermal-assisted field emission. This occurs at even a lower power than one might predict because at high power, even if multiphoton emission dominates for alignment to the tip apex, there is a risk of significant thermal emission if the beam alignment moves slightly up the shank of the tip.

In a hypothetical low repetition rate experiment, the maximum pulse fluence is limited instead at the point where transient thermal emission is more important than multiphoton emission. The energy density deposited at the tip apex is given by

$$Q = \beta_Q \mathcal{F}, \quad (3.31)$$

where \mathcal{F} is the pulse fluence and $\beta_Q = 220 \text{ J/m}^3 \text{ per nJ/cm}^2$ is determined from the electromagnetic model of the previous section. The initial temperature rise, T_{trans} ,

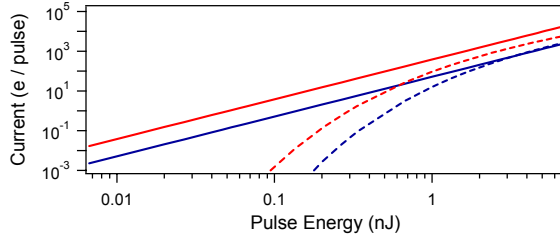


Figure 3.22: Predicted scaling of transient TFE and multiphoton emission for a 120 nm radius HfC tip. Solid lines are two-photon emission. Dashed lines are estimated transient thermal-assisted field emission, assuming an electron-phonon coupling time of 1 ps. The blue curves are for 0.5 GV/m bias field, and the red curves are for 1.5 GV/m bias field. The largest pulse energy corresponds to $\gamma_K \sim 1.5$. Adapted from [43] ©2012 APS.

can be obtained by solving

$$Q = \int_{T_{DC}}^{T_{trans}} C_{el}(T_{el}) dT_{el} \quad (3.32)$$

The total emitted charge is estimated as the thermal-assisted field emission current at T_{trans} multiplied by the electron-phonon coupling time τ_{el-ph} . Again assuming a 1 ps electron-phonon coupling time for HfC, Figure 3.22 compares the scaling of emission due to a thermal transient with the scaling of multiphoton emission in the low repetition rate limit for a tip like the one used experimentally. The pulse fluence where the two processes become comparable in size depends on the bias field applied to the tip. For reasonable bias values, transient thermal emission begins to overtake multiphoton emission as the Keldysh parameter gets close to 1. For large bias fields, it is possible to get to the few 10^4 electron per pulse regime before the transient thermal process dominates.

Chapter 4

Energy-domain streaking for direct emission-time measurement

This chapter describes a proposed method for direct measurement of the electron emission time from a laser-triggered field emission tip. In the previous chapter, it was shown that multiphoton emission and photo-assisted field emission are readily observed, and distinct from thermally-induced emission. Multiphoton emission and photofield emission are assumed to be prompt with respect to the laser trigger, but analysis of power scaling of emission does not exclude the possibility of emission from long-lived excited states or non-equilibrium electron distributions, as has been observed for metal surfaces illuminated at high pulse fluence [75]. Furthermore, simulations of the non-adiabatic tunnel regime and the work of Krüger et al. [10] on the variation of electron emission spectra with carrier-envelope phase show that sub-optical cycle emission can occur, and suggest that with arbitrary waveform generation, one might be able to create arbitrarily shaped electron pulses with sub-femtosecond features. If we wish to control the temporal waveform of the electron pulse with this degree of precision, we must first be able to measure it.



Our initial approach to this problem was to apply a rapidly time-varying voltage to the tip, mapping time of emission to electron kinetic energy, which is then analyzed. Our experiment is essentially a longitudinal streak camera; here, energy plays a role analogous to the deflection in a conventional, transverse streak camera. This is similar

to the concept of the atomic transient recorder, which uses infrared fields to streak photoelectrons generated by attosecond XUV pulses [76], but in a completely different frequency range . In this initial approach, we built what is effectively an ultrafast sampling oscilloscope—a device capable of measuring periodic voltage variations at the tip with the temporal resolution of the emission process, *a priori* less than 10 fs for multiphoton emission. With this proof-of-concept apparatus, we characterized the electron emission time with sub-picosecond resolution.

The second part of this chapter will discuss how the time-resolution of the measurement could be improved to the 10 fs or perhaps even fs level. In particular, we propose increasing the streaking slope by integrating the electron source into a microwave cavity, which can be used to build up large time-varying fields. Improvements in the synchronization of the microwaves and laser pulses will also be necessary.

4.1 Proof-of-concept: ultrafast oscilloscope and energy-domain streaking without an RF cavity

4.1.1 Experimental setup

The experimental setup of the “ultrafast oscilloscope” is shown in Figure 4.1. Sub-10 fs pulses from a Titanium:Sapphire oscillator (a) are used to trigger emission from a tungsten field emission tip (~ 120 nm radius of curvature at the apex—(b)) via multiphoton photoassisted field emission or multiphoton over-the-barrier emission, depending on central bias voltage. The electrons are collimated by an electrostatic lens, and travel in an ≈ 8 cm field-free region. We have analyzed the electron energy using both time-of-flight methods and a retarding potential method, where grids in front of the electron detector prevent electrons with insufficient kinetic energy from reaching the detector. Both methods measure the kinetic energy of the electrons after they leave the lens along the direction parallel to the tip axis. Both methods yielded similar energy resolutions, of 2 eV (FWHM) for average tip bias voltages of 20-50 V. The true energy distribution of the electrons is smaller than this, and either method could be optimized to obtain higher resolution.

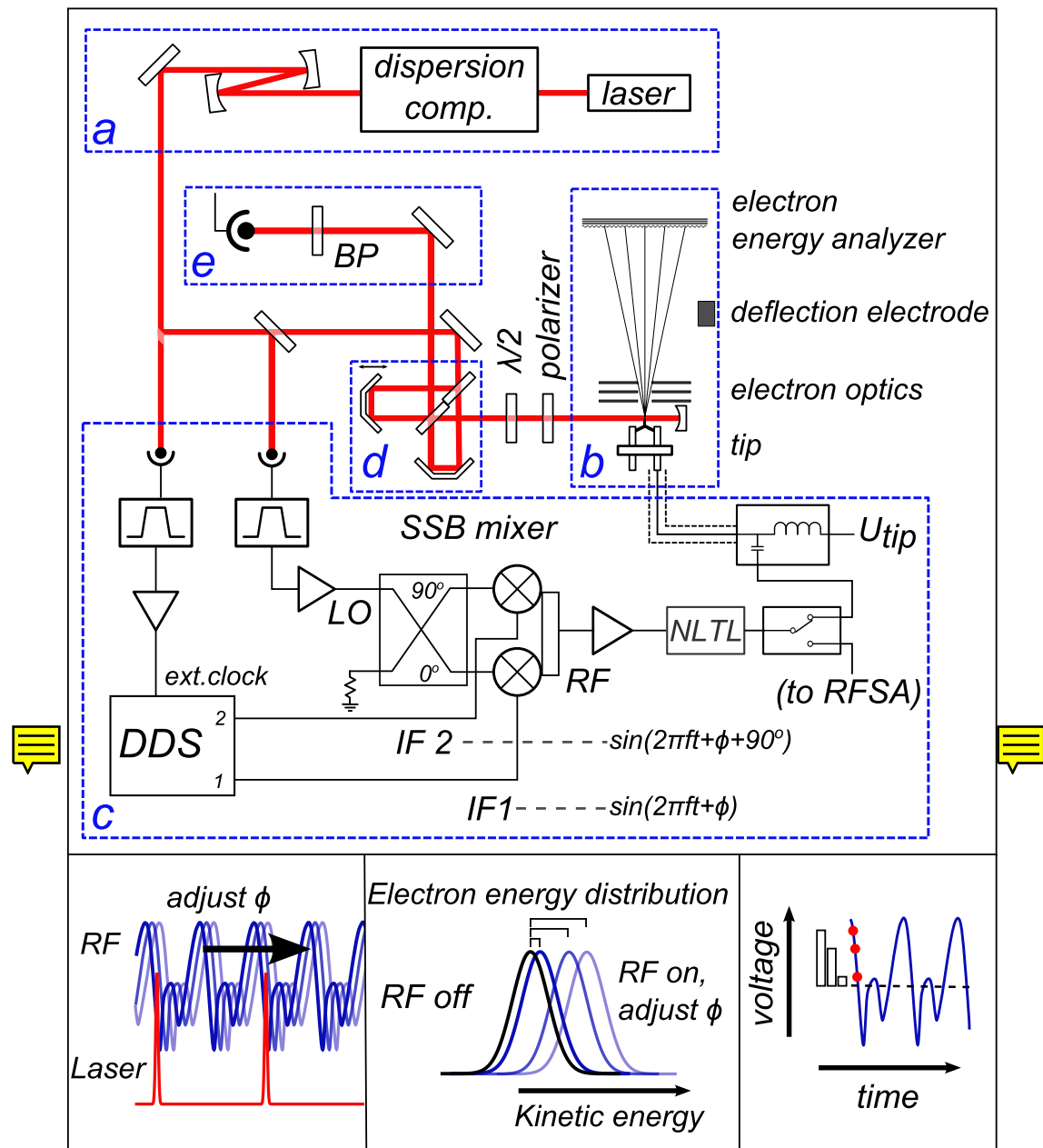


Figure 4.1: Experimental setup.

The number of electrons in a single pulse is not large enough to measure the center of the energy spectrum or its width with high precision. If the RF signal is synchronized with the laser, however, electrons from multiple pulses can be combined to measure an energy spectrum for a given time delay between the RF signal and the sampling laser pulse, as illustrated in the bottom part of Figure 4.1.

To achieve this synchronization, the RF signal in the experiment is derived from harmonics of the laser repetition frequency ($f = 150$ MHz), measured with a fast photodiode. A direct digital synthesizer acts as a programmable phase shift for a signal at the frequency f (also derived from a pick-off beam on a photodiode-(c)). We tested two different strategies to obtain rapid voltage sweeps. In the first strategy, the DDS output is mixed with a harmonic of f with frequency ≈ 600 MHz to generate a ≈ 750 MHz signal and passed through a non-linear transmission line (NLTL; Picosecond Pulse Labs LPN-7102). The wave traveling along an NLTL satisfies a non-linear wave equation, where the propagation speed is a function of voltage amplitude. The result is a steepening of the negative slope of the input sine wave as it propagates, with the output of the NLTL approximating a sawtooth wave with picosecond fall times [77]. Alternatively, the DDS output is upconverted using a single-sideband mixer to generate a signal at $62f \sim 9.28$ GHz with computer-controllable phase. In both cases, a broadband bias tee combines the RF with a DC tip bias voltage, and electrical connection to the tip is a semirigid coaxial cable with the shield grounded at the vacuum feedthrough.

4.1.2 Oscilloscope measurements

Non-linear transmission line

Figure 4.2 shows the waveform generated in a nonlinear transmission line (NLTL). The NLTL generates a comb-like RF spectrum of the harmonics of the 750 MHz input (which is itself a harmonic of the laser repetition rate). The oscilloscope trace is obtained by stepping the phase of the DDS (and therefore the 750 MHz driving the NLTL) and measuring spectra with RF alternately on and off. The difference between the center voltages of the spectra with RF on and off reflect the voltage due to the

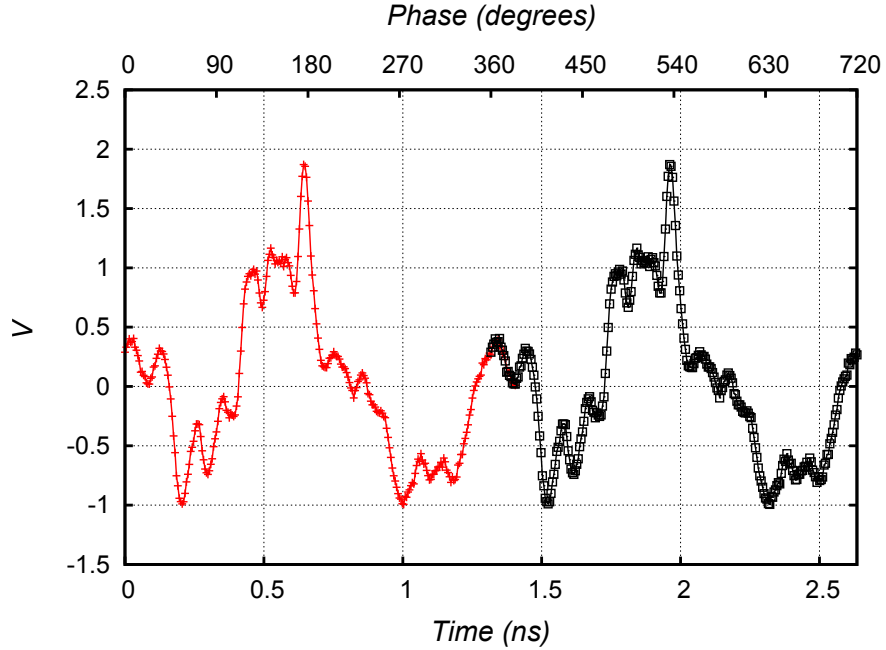


Figure 4.2: Measured oscilloscope trace for non-linear transmission line output.

RF signal at the time the electrons were emitted. The measured trace is not as close to a sawtooth wave as the trace from [77], which shows the output of a similar NLTL (PPL LPN-7113-110) measured with a commercial sampling scope. This might be due to the complicated frequency response of the bias tee, feedthrough, and coaxial cable connecting to the tip. In Ref. [77], the maximum derivative of voltage with respect to time is about 20 mV/ps. Even though our maximum voltage swing is about 6 times larger, the maximum slope is 50 mV/ps. As shown in the next section, we were able to achieve a higher streaking slope by simply amplifying a higher harmonic of the laser repetition rate.

9 GHz sine wave

The frequency response of the system from the bias tee onwards was characterized by running the experiment over the range of frequencies within the bandwidth of the microwave amplifiers. The repetition rate of the laser was not locked to the microwave frequency, so the measured spectra samples the voltage at the tip at a

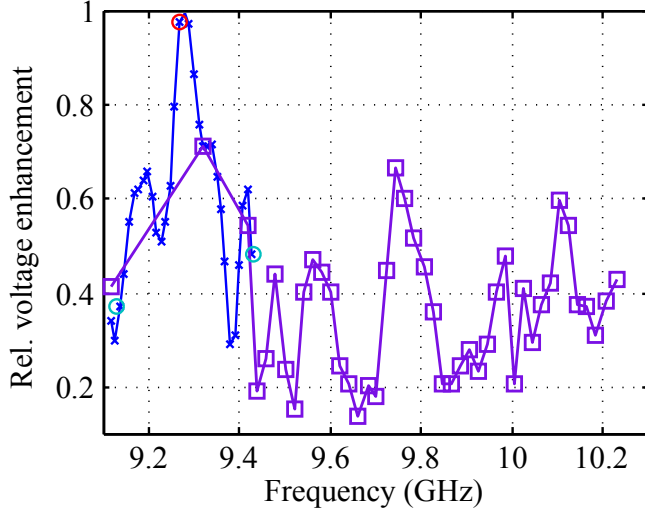


Figure 4.3: Frequency response of the tip. The amplitude of the response is measured by amplifying the output of a frequency synthesizer and recording time-of-flight spectra. Since the RF is not phase-locked to the laser, the time-of-flight spectrum is broadened by the RF and represents a convolution of the spectra for different tip voltages with the dwell-time of the sine wave at that voltage. Fitting the spectra yields the amplitude of the sine wave on the tip. The y -axis units are relative to the peak value of the amplitude response.

large and effectively random set of phases. The result is a highly broadened spectrum from the convolution of the spectra at different voltages with the dwell-time of the sine wave at that voltage. Fitting the spectra to this model, the amplitude of the sine wave applied to the tip can be determined as a function of frequency (Fig. 4.3).

The frequency response of the tip shows a maximum near 9.3 GHz; to maximize the streaking slope given the available microwave power, it is advantageous to work near this frequency. Figure 4.4 shows the oscilloscope trace recorded with a 9.28 GHz signal (62nd harmonic of the repetition rate). Data are measured for increasing ϕ , and the full data set (squares) is reproduced with a 360 degree offset (crosses); the overlap shows that the measurement is stable over the several hours required to measure this trace. The lower left hand plot shows a zoomed in portion of the oscilloscope trace, with phase steps of 0.075 degrees, corresponding to 22.4 fs.

A numerical fourier transform of the oscilloscope trace shows that it is not a pure

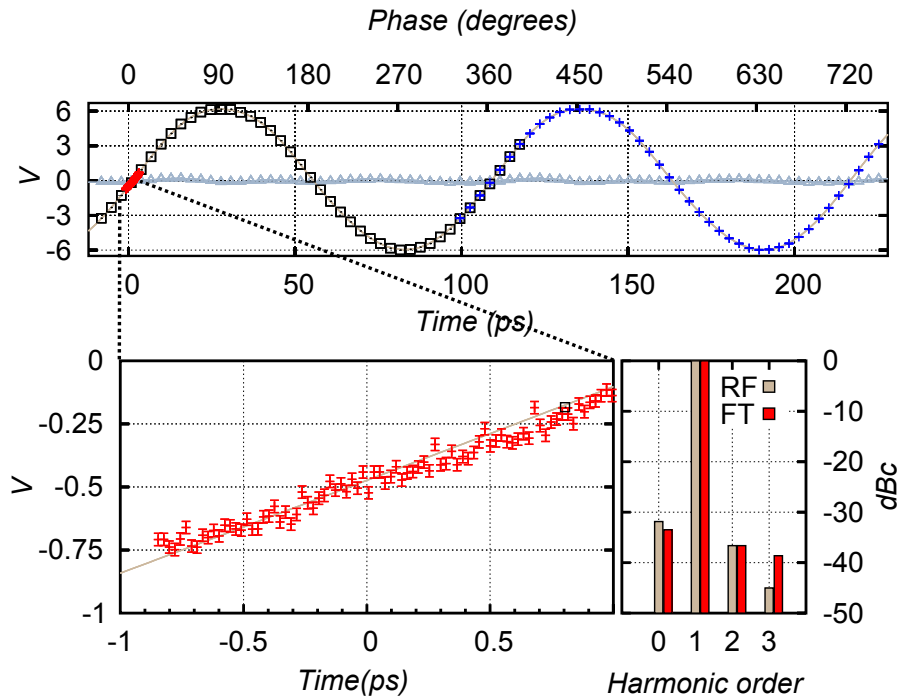


Figure 4.4: The top plot shows the measured oscilloscope trace for a 9.28 GHz sine wave ($62f$) applied to the tip. The data set (squares) is plotted again with a 360 degree phase offset (crosses). The voltage error bar at each point is 20 mV for a measurement time of ≈ 100 s per spectrum. “Residuals” (data with DC offset and 9.28 GHz fourier component subtracted) are plotted with triangles. The plot on the lower left is a zoomed-in portion of the oscilloscope trace, with phase steps of 0.075 degrees (22.4 fs). The plot on the lower right shows the fourier spectrum (FT) computed from the oscilloscope trace alongside the corresponding RF amplitudes applied to the tip (at the LO, LO+ f , LO+ $2f$, and LO− $3f$). The RF spectrum was measured before the bias tee, and then corrected for the frequency response of the tip and bias tee, which was independently measured.

sine wave: there is a small DC offset as well as higher order spectral components, and the magnitude of the slope at the two zero crossings differs. This could be due to small amounts of uncompensated drift during data taking. Another contribution is from spurious single-sideband mixer products whose phases increase by $n\phi$ as the phase ϕ of the 9.28 GHz signal is adjusted. The fourier spectrum of the measured trace is shown in the lower right hand plot. The $n = 0$ component is the equivalent power due to a sine wave with the amplitude of the DC offset of the trace. The residuals (measured data minus the DC offset and the 9.28 GHz component) are shown in the top plot. For comparison, the RF amplitudes of the corresponding mixer products are plotted alongside the fourier spectrum of the trace. The $n = 0$ component is due to the LO, and the $n = 2$ and $n = 3$ components are due to the $LO + 2f$ and $LO - 3f$, respectively. Thus the streaking slope estimated by differentiating the raw oscilloscope trace is only approximately correct. Using fourier analysis to determine the amplitude and phase of the actual RF fields on the tip, we can make a more accurate determination of the streaking slope as 0.4 V/ps at the zero crossing of the sine wave.

4.1.3 Streaking measurements

To illustrate the energy-domain streaking concept, the Michelson interferometer (part (d) of Fig. 4.1) is used to generate a copy of the pulse train offset in time by ~ 5 ps. Spectra with the double and single pulse trains were measured near the zero-crossings of the RF (streaking slope of 0.4 V/ps) and are shown in Figure 4.5 . The pulses are sufficiently separated in time that the temporal structure is clearly discernible in the energy spectra. The spectra are fit with one or two asymmetric gaussians to determine their relative emission times (the width and skew were constrained to be the same for the double pulse spectra as for the single pulse spectra).

There is some uncertainty (on the order of 100 fs) in the position of the peaks due to line pulling from the background, which was modeled as an additional gaussian peak. This is manifest as a difference in the time-delay inferred at the two zero crossings (4.85 ps and 4.75 ps for the positive and negative slopes, respectively) and

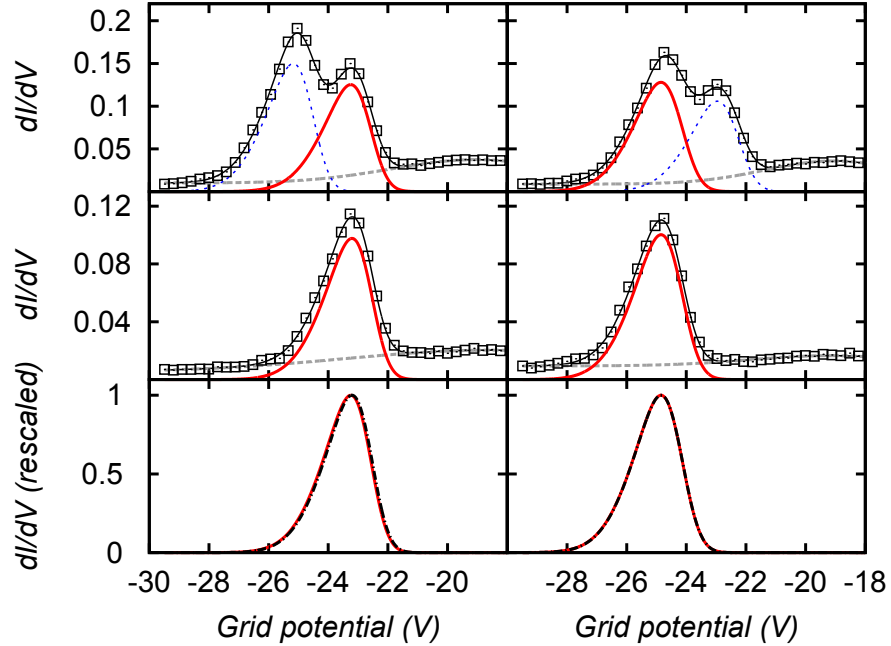


Figure 4.5: Energy-domain streaking. Spectra with one or a double pulse train incident on the tip near a zero-crossing of the RF. The plots on the left are for positive slope (V increases with time), and those on right are for negative slope. The top plots show the spectra for the double pulse train, and the middle plots show the spectra with the first pulse blocked. The spectra are fit with asymmetric gaussian distributions (for the main peaks—solid red and dotted blue lines), and the background from secondary and scattered electrons is fit with a gaussian (grey dashed line). The total fits are shown as solid black lines through the data points. The bottom plots show the red curves from the top and middle plots, normalized to their peak values (solid red line—double pulse spectra, black dash-dot—single pulse spectra); the difference in position between the two fits corresponds to 110 fs for the positive slope and 10 fs for the negative slope.

a spurious shift of the component of the spectrum due to the second pulse (solid red curve) between the top and middle plots. This shift is larger for the positive zero crossing, where the peaks in question are closer to the background “peak” (see bottom panel of Figure 4.5). Note also that the amplitudes of the main electron emission peaks vary slightly due to the instantaneous bias voltage (compare amplitudes of the dotted blue curves in the top panel) and differences in the temperature of the tip (compare solid red curves in the top panel vs. the middle panel, which is measured with half the average optical power).

At the zero-crossing of the RF signal, the tip voltage is (locally) a linear function of time. The streaked electron spectrum becomes a convolution of the temporal profile of electron emission and the electron energy spectrum measured with no RF. Figure 4.6(a) shows the numerically simulated increase in full-width half max (FWHM) when the measured energy spectrum is convolved with gaussian pulses of varying duration, assuming a streaking slope of 0.4 V/ps. Since the energy spectrum is asymmetric, the maximum of the streaked spectrum is shifted relative to that of the unstreaked spectrum (Fig. 4.6(b)). The optical pulse does not arrive exactly at the zero-crossing, and the time-delay between the optical pulse and the microwaves may drift slowly over the course of the measurement. This can be accounted for by measuring alternately at the two zero-crossings.

For typical oscilloscope-type measurements (Figures 4.2 and 4.4), the time to record a spectrum was around 100 s, and the measured center of the spectra have a standard deviation of ≈ 20 mV. Averaging for 10 hours (including time to measure a reference spectrum at each point), a precision of 1.5 mV can be obtained for spectral shifts, which constrains the emission time to less than 300 fs (Fig. 4.6).

4.2 The route to improving time-resolution of the streaking experiments

In our initial streaking experiment, we demonstrated an upper bound of 300 fs on emission time. To provide new information about the emission process, the resolution

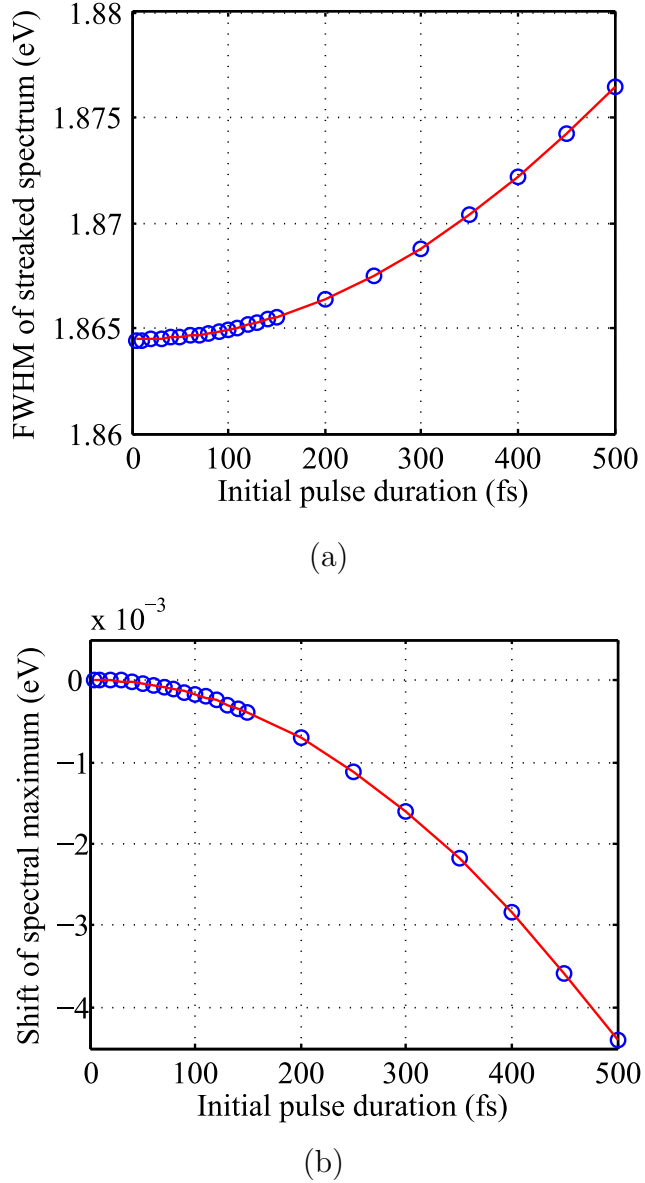


Figure 4.6: Simulated effect of energy streaking on the measured spectrum. Blue circles are numerical simulation, and the red curves are quadratic fits to the simulation results (see text). (a) Full-width at half-max (FWHM) of the electron energy spectrum after streaking. The shape of the un-streaked spectrum is taken from the data of Figure 4.5 and has a FWHM of 1.864 V. The temporal shape of the electron pulse is assumed to be gaussian. (b) Shift in position of the spectral maximum due to streaking. For both plots, the streaking slope was assumed to be 0.4 V/ps; for different streaking slopes, the x -axis will be re-scaled (i.e., if the streaking slope increases by a factor of 10, the x -axis labels should be divided by 10).

must be 10 fs or better. In this section, we consider the factors that restrict the temporal resolution so far, and propose a next generation version of the experiment to address them.

4.2.1 Technical limits to time-resolution

Resolution of temporal shifts and broadening

The streaking measurement implements a convolution between the energy spectrum and the temporal profile of the pulse. With 0.4 V/ps streaking, the 10 fs time differences we wish to observe become voltage widths of 4 mV. There is a basic mismatch between this number and the resolution of the electron energy analysis, which is on the order of 2 V. A large improvement could be obtained by making these numbers of the same order of magnitude.

This problem can be attacked from both sides: Electrostatic energy analyzers with an energy resolution of 40 meV FWHM, can be built relatively easily [78]. This is smaller than the intrinsic energy spread of the source, which is on the order of 0.3-0.5 eV and thus could give an improvement in time resolution of the experiment by a factor of 4 over the current value. On the other hand, one can try to improve the streaking slope: to achieve the goal of distinguishing sub-optical cycle structure (~ 2 fs) requires an increase in the amplitude of the RF waveform by 2 to 3 orders of magnitude. A better understanding of the background seen in Figure 4.5 could dramatically improve the time resolution, as it currently contributes systematic shifts that vary from one data set to the next, resulting in approximately 40 mV uncertainty in measurements of the center of the spectrum.

Count-rate limitations

In the original experiment, 10 hours of averaging were required to obtain 1.5 mV error bars on the position of the center of the spectrum. An estimate of the fundamental limits on the error bars due to counting statistic yields a surprise—with an energy resolution of 1.85 V and a laser repetition rate of 150 MHz, if the experiment is operated so that the tip generates on average one electron per laser pulse, it should

be possible to obtain a precision of 1.5 mV in only 10 ms! This highlights the fact that the energy analysis methods used are unable to take advantage of the high count-rates available from the electron source. In the time-of-flight method, dead time in the pulse detection electronics severely limits the practical count rate to far below 150 MHz. On the other hand, the retarding potential method requires scanning of the potential on the retarding grid, so that the spectral information is measured sequentially and based on numerically differentiating the data. An energy analysis method such as a Wien filter, which spatially disperses the electrons, should allow the spectrum to be recorded in parallel at high count-rates.

Phase noise

Microwave phase noise degrades the temporal resolution of the oscilloscope and streaking measurements, as it is equivalent to introducing time-jitter in the arrival of the optical pulses on the tip. Synchronization of the laser pulse train and a microwave signal at the femtosecond level is an ongoing area of research, in part as it is a prerequisite for using microwave pulse compression to reach 10 fs pulses in ultrafast electron diffraction experiments [2, 31].

Our passive system, where the microwave signal is directly derived from a photodiode signal, performs quite well. The phase noise in the generation of the ≈ 9 GHz microwave signal applied to the tip was measured by mixing the final microwave signal with the photodiode signal (after the first amplifier stage), with a low-pass filter to isolate the DC mixer product (see Fig. 4.7). When the phase between the two mixer inputs is chosen to zero the DC output, the voltage fluctuations in the DC output are linearly proportional to the phase fluctuations. This permits a measurement of the phase noise introduced by most of the electronics—in particular, the phase noise of the 150 MHz signals used to drive the IF ports of the SSB mixer, which was expected to be the major source of phase noise in the upconverted signal at high frequencies. The measurement excludes the phase noise of the photodetector for the LO and its first amplifier, since this is the signal used as a reference.

The measured jitter spectral density is shown in Figure 4.8. Integrating from 1 Hz to 100 kHz yields a total of 47 fs rms timing jitter. The noise is expected to cut

off at ~ 6 MHz due to the narrow tunable cavity filter.

The signal-to-noise of the photodetection process that generates the microwave signal is often the largest contributor to the phase noise, with noise at high frequencies due to shot noise and Johnson noise, and noise at low frequencies from processes like amplitude-to-phase conversion. The latter can lead easily to rms jitter on the order of a few fs or larger in a 100 kHz bandwidth. By carefully adjusting operating points (adjusting pulse energy and/or microwave frequency), the amplitude-to-phase conversion coefficient can be effectively nulled, reducing this effect below the noise floor set by shot noise and Johnson noise [79]. Feedback can be used to further reduce the phase noise; McFerran et al. [80] demonstrated sub-fs rms jitter at 10 GHz using microwave interferometry techniques.

4.2.2 Energy streaking of electrons emitted in a microwave cavity

Improved energy analysis and locking of the microwave signal to the laser repetition rate are more or less standard techniques. Some increase in the streaking slope can be obtained by adding bigger microwave amplifiers, but at some point this becomes impractical. We can obtain an even larger increase in the streaking field by building up the microwave field in a cavity. This idea is the subject of the remainder of the chapter.

Ultrafast electron pulses and microwave cavities

The integration of ultrafast electron sources with RF cavities has been proposed in several different contexts. Since RF breakdown voltages are typically higher than DC breakdown voltages, placing a planar photocathode source in an RF cavity can allow larger acceleration and reduce kinematic broadening of the pulse as well as create some temporal focusing [20]. Several groups are pursuing pulse compression with RF cavities with the goal of generating non-relativistic, sub-100 fs pulses at a target with enough electrons per pulse for single-shot imaging [30, 31, 32]. With a timed source and time-varying fields, the Scherzer theorem (which states that spherical and

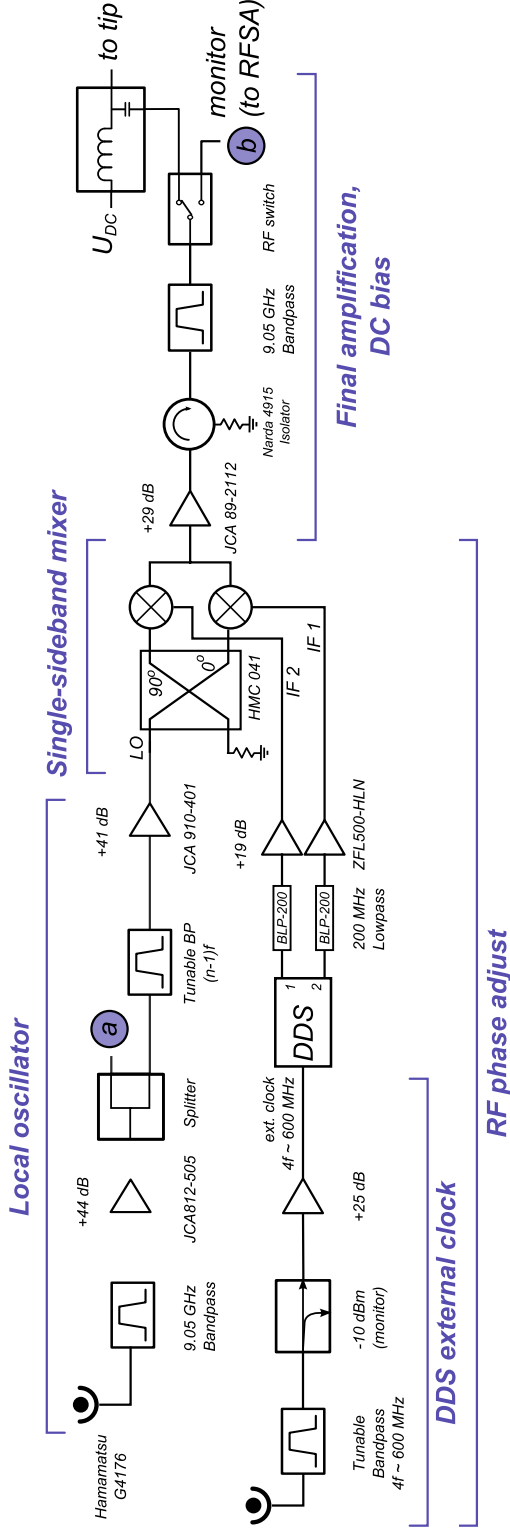


Figure 4.7: Detailed ultrafast oscilloscope/ energy streaking experimental setup with phase noise measurement. The combination of the direct digital synthesis (DDS) frequency synthesizer and single-sideband mixer permit computer control of the RF phase of the microwaves applied to the tip with low phase-noise. The local oscillator (LO) for the mixer and clock input for the DDS are harmonics of the laser repetition rate, f , and are derived from the filtered and amplified output of two fast photodiodes illuminated by the laser pulse train. The phases of IF_1 and IF_2 are controlled by the DDS. The mixer output is amplified again. A bias tee combines the DC voltage applied to the tip with the microwave signal. A computer-controlled switch allows the microwave signal to be applied to the tip or monitored at (b). The phase-noise introduced by the mixer and amplifier chain is measured by mixing the monitor signal at (b) against the signal at (a).

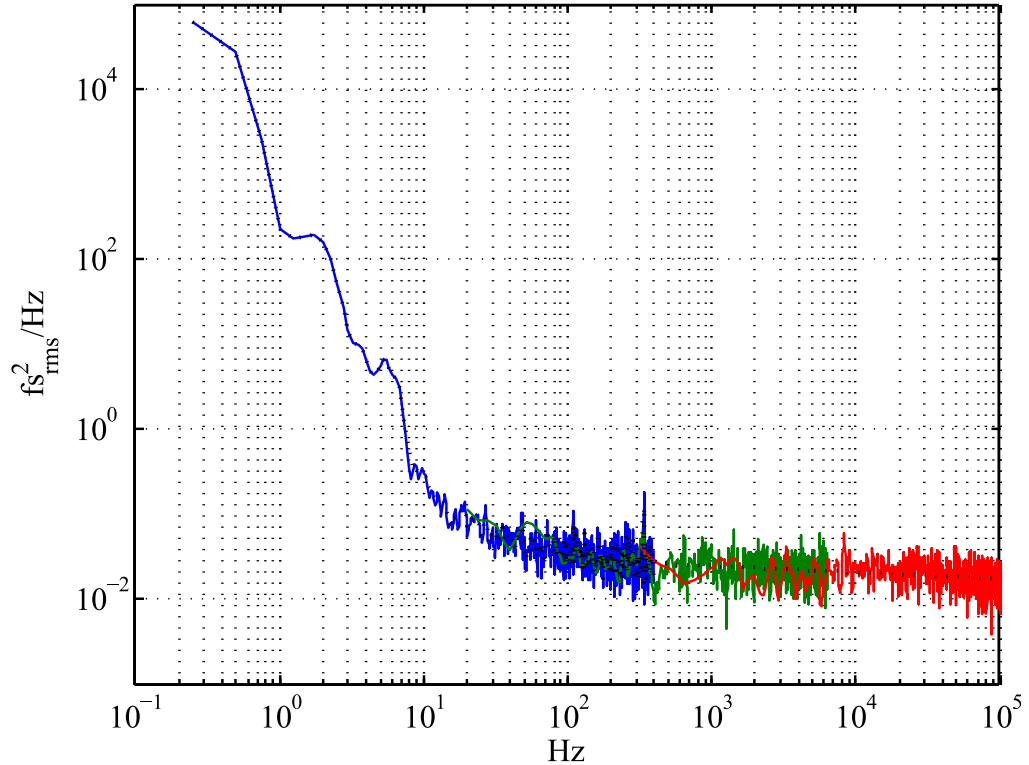
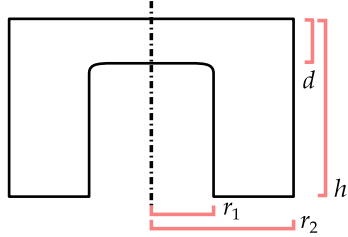


Figure 4.8: Jitter spectral density for amplified 9 GHz repetition rate harmonic applied to tip. The experimental setup is as shown in Figure 4.7: the signal at (b) is attenuated and mixed with the signal at (a) (amplified photodiode output near 9 GHz), and the result is low-pass filtered to isolate the DC component. This permits the measurement of the phase-noise introduced by the phase-adjustment electronics and amplifier chain, excluding the first (JCA 505-812) amplifier and the LO photodiode itself, but including noise from the photodetector, amplifiers, and DDS used to generate the IF inputs to the SSB mixer.



Dimension	Value
Total height	h 19.5 mm
Gap	d 5 mm
Inner radius	r_1 7 mm
Outer radius	r_2 16 mm

Figure 4.9: Dimensions of un-modified re-entrant cavity. The dash-dotted line is an axis of rotational symmetry of the cavity prior to adding the tip, coupling antenna, laser entrance/ exit apertures, etc.

chromatic aberrations in an electron optical system cannot be compensated using only cylindrically symmetric fields) no longer applies; thus, RF cavities have been proposed as aberration-free lenses for ultrafast electron pulses [81]. The development of laser-driven dielectric accelerator structures could allow the extension of these techniques to sub-femtosecond electron pulses controlled by optical fields [34].

Cavity design and realization

The TM0n0 modes of a cylindrical pillbox cavity have zero transverse electric fields, and the longitudinal field is independent of z [82]. This is the microwave analogue to the DC fields normally applied to the tip if we place the tip on the symmetry axis of the cavity and emit electrons towards a small aperture in the far wall.

Modifying the cylindrical pillbox to a re-entrant design (Fig. 4.9) increases the electric field in the narrow “gap” region of the cavity [83]. With the tip protruding through a small aperture, the electrons will be emitted in this region and accelerated towards the far wall of the cavity, where another aperture allows them to escape. Additional apertures are necessary for laser access. We chose to work with the TM020 mode instead of the fundamental mode, which allows the cavity dimensions to be increased slightly, relaxing machining requirements and making it easier to place the antenna used to couple power into the cavity. The cavity mode was modeled using finite element analysis [84]. The model includes the tip, laser entrance/ exit apertures, and electron exit aperture. The addition of these apertures in general decreases the quality factor, Q , of the cavity, resulting in a tradeoff between the Q and the numerical

Aperture	Diameter	Thickness of cavity wall at aperture
Laser entrance	2.00 mm	0.76 mm
Laser exit	1.50 mm	0.76 mm
Tip	1.59 mm	0.36 mm
Electron exit	2.00 mm	1.59 mm

Table 4.1: Final dimensions of additional apertures required for the microwave cavity. The gap between the posts of the tip mount and the cavity at the closest point is approximately 0.9 mm.

x	h	d	r_1	r_2
df_0/dx (kHz/ μm)	-345	155	-83	-160

Table 4.2: Sensitivity of the resonance frequency to modifications of the cavity parameters in the vicinity of the parameter values in Figure 4.9. The unperturbed resonance frequency is 9.08 GHz.

aperture for illuminating the tip. The dimensions of the final design are given in Table 4.1 , and a drawing of the cavity with tip loaded and simulated fields of the TM020 mode are shown in Figure 4.10. The resonance frequency of the TM020 mode is calculated to be 9.08 GHz, with a Q of 2400 for copper. The presence of a coupling antenna also alters the Q of the cavity, and modeling was used to estimate placement and length of the coupling antenna that maximizes the electric field in the gap region of the cavity for a given amplitude of RF excitation.

The modeled sensitivity of the cavity to changes in its main dimensions is shown in Table 4.2. Given that the linear thermal-expansion coefficient of copper at room temperature is $16.6 \times 10^{-6} \text{ K}^{-1}$, linearly adding these contributions yields a frequency shift of 24 kHz for a 10°C change in temperature.

The cavity was machined from OFHC copper, and its Q outside of vacuum (and without the tip) is 2000 (Fig. 4.12). In the design, the tip is mounted so that it is electrically isolated from the cavity walls, permitting it to be operated with both DC and microwave “bias” .

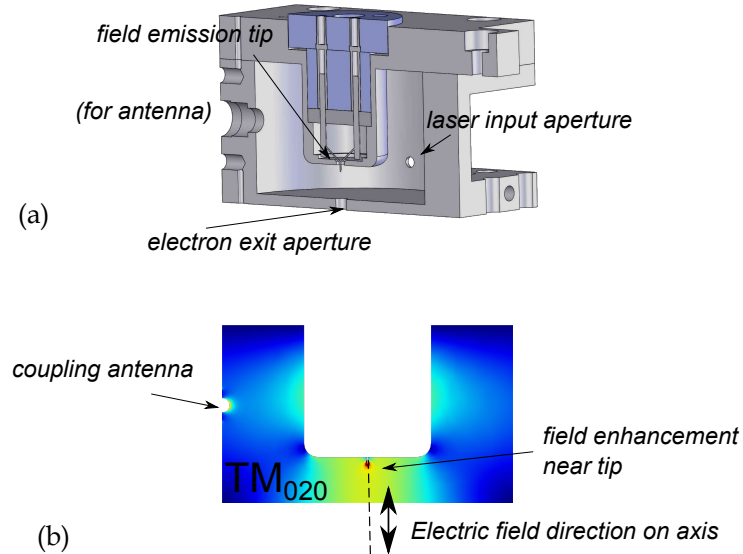


Figure 4.10: (a) CAD model of the cavity with tip and apertures for the laser beam and electrons, as well as for the antenna. (b) Finite element model of electric fields for the TM_{020} mode. The fields are on-axis in the center of the cavity.



Figure 4.11: Photograph of the finished cavity.

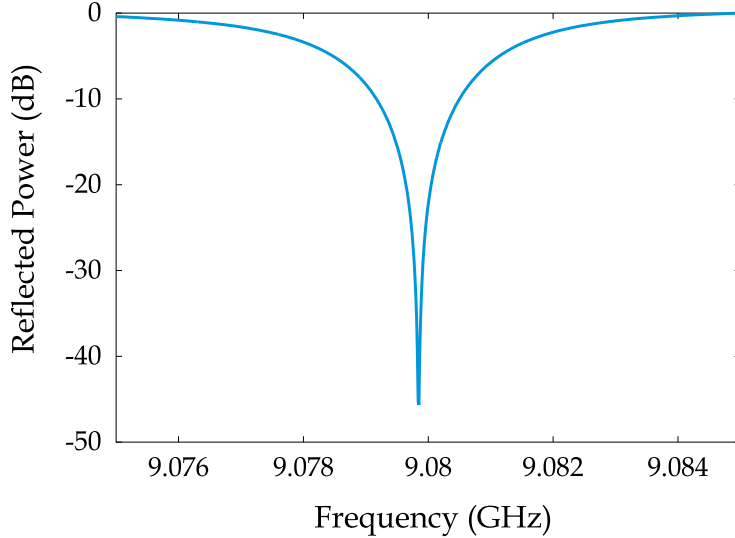


Figure 4.12: Cavity resonance measured in air, without the field emission tip. From the width of the resonance, $Q = 2000$.

4.2.3 Simulated electron trajectories

The electrons propagate 4.25 mm from their point of emission to the exit of the cavity. During this time, the electric field in the cavity changes since it is oscillating near 9 GHz. The picture is complicated by the fact that the microwave fields are enhanced near the tip and the electrons are strongly accelerated by both DC and microwave fields as they leave the tip; thus we expect the RF phase to modulate the electrons' final kinetic energy more than if the source launched the electrons from outside the cavity.

To calculate the final kinetic energy of the electrons as a function of the DC and microwave fields applied, the on-axis trajectories are integrated using the 4th-order Runge-Kutta method. The electric fields are determined using a DC model for both the DC and microwave fields solved by the finite element method [85]. The geometry is of a capacitor with the tip extending through a central aperture in one plate; to simulate the DC field, a negative voltage is applied to the tip relative to the two plates of the capacitor, which is at ground, and to simulate the RF fields, a DC model is solved with a non-zero voltage on the far plate relative to the tip and plate with

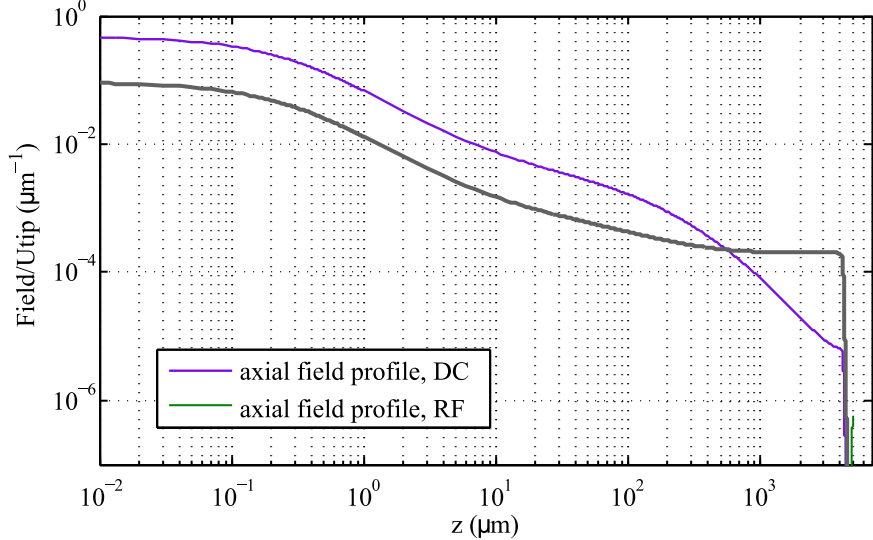


Figure 4.13: Field profiles used for determining the electron trajectories. Both the DC field profiles and the “RF” field profiles are actually DC solutions (see text). Note that the fields drop sharply at the exit aperture of the cavity ($z = 4.25$ mm).

aperture. The DC solution for the RF fields is then multiplied by a time-dependent factor of the form $\cos(\omega t + \phi)$. It was verified that this solution matches full RF field models for large tip radii. The field profiles used are shown in Figure 4.13.

Figure 4.17(a) shows the simulated energy gain as a function of RF phase for a few DC tip voltages, assuming a peak-to-peak microwave field amplitude of 1120 V, which is the estimated voltage amplitude for 2 W input to the cavity (assuming $50\ \Omega$ coupling and factor of 40 gain in amplitude estimated from cavity simulations discussed previously). The maximum slope (rate of change of final kinetic energy with phase) determines the temporal resolution that can be obtained in an energy-streaking experiment. This is plotted vs. tip voltage, and it is clear that there is a strong modulation depending on how many half cycles of the microwave field the electron sees as it passes through the cavity. Example trajectories of electron kinetic energy vs. time are shown in Fig. 4.15, where it can be seen that the RF phase dependence of the electron energy gain is suppressed near $U_{\text{tip}} = 1350$ V because it takes roughly two RF periods for the electrons to traverse the 4.25 mm of the cavity. At optimally chosen tip voltages, the maximum slope is about a factor of 3 smaller

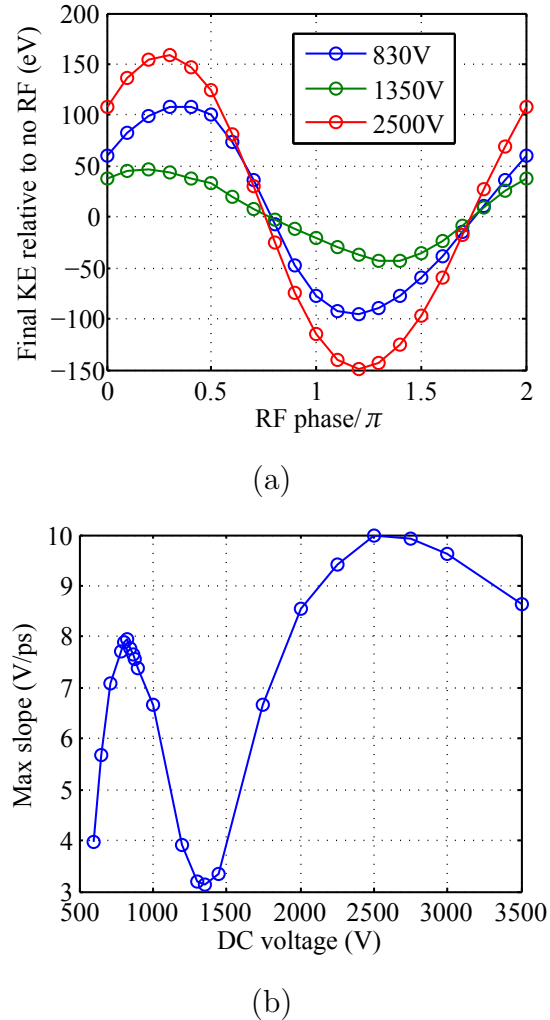


Figure 4.14: Simulated energy-domain streaking with a microwave cavity. For these simulations, the RF excitation amplitude is 14 V with a buildup factor of 40, and the tip radius is 500 nm. (a) Energy gain (relative to no RF) vs. RF phase at different values of U_{tip} . (b) Maximum streaking slope vs. DC tip voltage.

than the 32 V/ps that would be expected if the electron energy gain were completely dominated by initial acceleration near the tip. The initial acceleration, however, is significant; if we call “energy modulation” the difference between the maximum and minimum energies that can be obtained at any given time by varying the initial RF phase, this quantity always exceeds zero as the electrons propagate through the cavity (Fig. 4.16), which would not be the case for uniform fields.

The same calculations may be repeated assuming a 20 W microwave amplifier. Here, the fields were calculated assuming a larger tip radius of 2.5 μm to increase the voltage threshold for field emission, and the maximum streaking slope is greater than 50% of the naive value.

Initial energy spread vs. emission time spread

Under some circumstances, initial differences in electron energy can also be “streaked”. In a toy model, consider an ultrafast electron source located outside a cavity (so that field enhancement effects can be neglected). Assuming a weak modulation of the trajectory by the RF field, and linearizing the equations near the zero crossing, the change in velocity at the exit of the cavity for a shift in emission time, δt is

$$\delta v_f \approx \frac{qE_0}{m} \delta t. \quad (4.1)$$

For a change in the initial velocity, δv_0 , we have

$$\delta v_f \approx \frac{qE_0}{m} \frac{L\delta v_0}{v_0^2}. \quad (4.2)$$

In the above equations, E_0 is the field amplitude, L is the cavity length, q and m are the charge and mass of the electron, and v_0 is the velocity of the electron as it enters the cavity. In order to distinguish between the emission time profile and the initial energy profile of the electrons, we require that

$$\delta t \gg \frac{L\delta v_0}{v_0^2}, \quad (4.3)$$

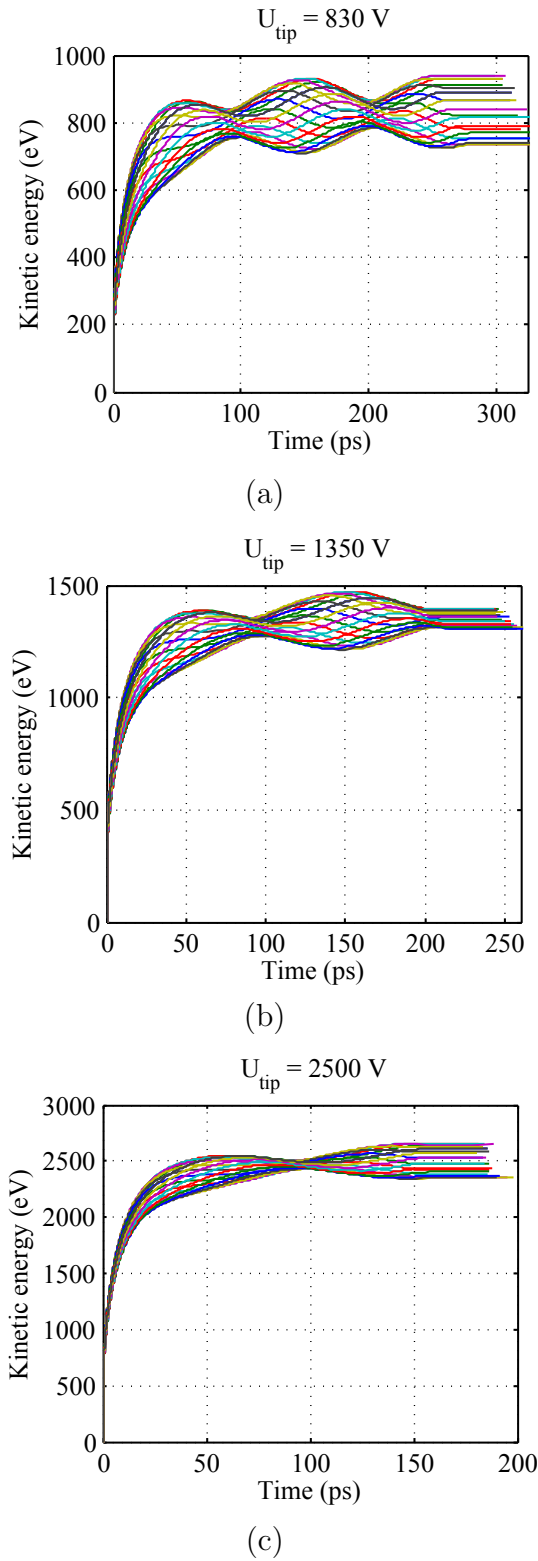


Figure 4.15: Ensemble of electron trajectories in the microwave cavity obtained for the different RF phases, at $U_{\text{tip}} = 830$, 1350 , and 2500 V. The RF phase dependence of the electron energy gain is suppressed near $U_{\text{tip}} = 1350$ V because it takes roughly two RF periods for the electrons to traverse the 4.25 mm of the cavity.

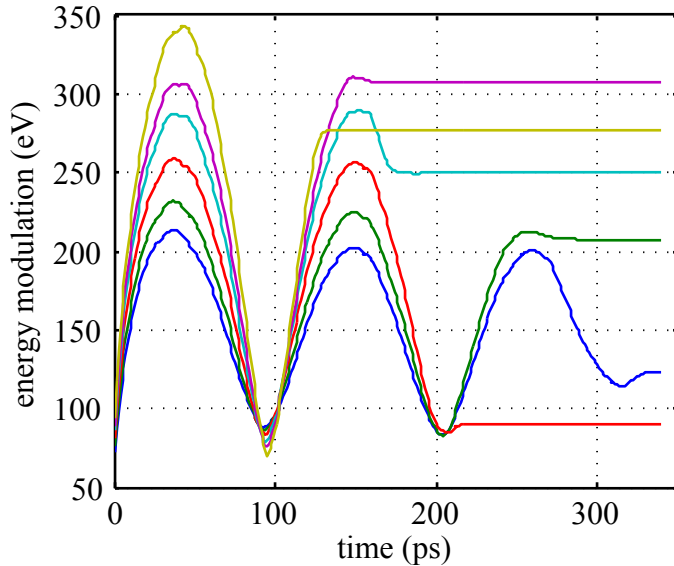


Figure 4.16: Energy modulation vs. time. The energy modulation is the difference between maximum and minimum energy at a given time, for the ensemble of trajectories. The RF excitation is 14 V, with a build-up factor of 40. The DC tip voltage is varied. Note that a certain energy modulation as a function of RF phase is acquired in the initial acceleration of the electrons in the strong electric fields near the tip, so that even when the RF field has completed a full cycle, the energy modulation does not go to zero. However, this modulation is about a factor of 10 smaller than the peak-to-peak amplitude of the RF field. A greater modulation is obtained if the electrons are timed to exit the cavity after $n + 1/2$ RF periods, where n is an integer.

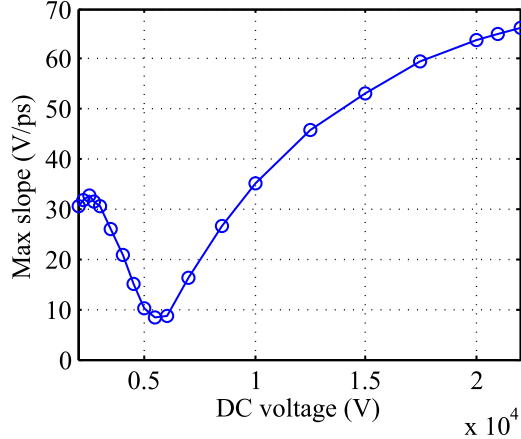


Figure 4.17: Maximum streaking slope vs. DC tip voltage with RF excitation amplitude of 45 V and a buildup factor of 40. The tip radius in the model is $2.5 \mu\text{m}$ to increase the voltage threshold for field emission.

where δt now refers to the desired time resolution. For the 4.25 mm propagation length and an energy of 20 kV of the experiment proposed above, and assuming a 0.3 eV energy spread, this condition is $\delta t \gg 1.3 \text{ fs}$. Clearly, there are advantages to decreasing L and increasing v_0 .

4.3 Summary

This chapter has focused on a microwave energy-domain streaking technique to characterize the temporal profile of electron emission. With the microwave signal applied directly to the tip, we demonstrate statistical error bars of 1.5 mV in determining the center energy of the spectrum after 10 hours of averaging, placing an upper bound of 300 fs on emission timescale. Emission time characterization with hundreds of femtosecond resolution could be useful for studying thermal emission processes. However, 10 femtosecond down to 1 femtosecond time-resolution is necessary to directly measure emission features of the multi-photon and non-adiabatic tunnel regimes and push forward our time-domain understanding of how these processes operate in solids.

We propose improvements to the original experimental design that would allow the energy-domain streaking technique to reach sub-fs levels. First, phase-noise in

the microwave generation must be reduced so that the integrated jitter is less than the desired time-resolution. Second, a proper electron spectrometer could improve energy resolution as well as vastly increase the effective count rate in the experiment, reducing the statistical error bars in determining pulse duration for a fixed streaking field. Finally, the streaking slope can be increased by building up the microwave signal in a cavity containing the tip.

The first two of these proposed improvements are standard techniques. However, the incorporation of the tip in the microwave cavity is slightly unusual in that the tip generates strong DC and microwave field enhancement and the electrons propagating in the cavity are non-relativistic. The second part of this chapter simulates electron trajectories in the cavity under the conditions of the proposed experiment, showing that the streaking slope can be increased by approximately two orders of magnitude for a given RF power.

Chapter 5

Laser-electron cross-correlation using electron acceleration in an evanescent field

The preceding chapter discussed an experiment to directly measure the temporal profile of electron emission from a tip. Methods to characterize electron pulses at some distance away from the source are also crucial. As an ultrafast electron pulse propagates in an experimental apparatus, the pulse may broaden temporally due to (a) its initial longitudinal energy spread, (b) Coulomb repulsion (unless the pulse contains only a single electron), and (c) aberrations of the electron optics. Many proposals for achieving sub-fs electron pulses rely on temporal focusing of the pulse [33, 32] such that the electron pulse may only be short for a small range of axial co-ordinates. These considerations make electron pulse characterization using streak cameras challenging, as the electron pulse parameters may evolve as it passes through the deflection plates of the streak camera [86].

Electron-optical cross correlation techniques are promising in that the interaction region is localized (in comparison with a streak camera), there are excellent techniques for characterizing optical pulses, and with light we can implement a mathematically simple interaction that can be inverted to obtain the electron pulse duration. The drawback is that electrons interact only weakly with light in free space. Hebeisen

et al. demonstrate a cross-correlation technique based on deflection of electrons by the ponderomotive potential of a pulsed standing wave [86]. Their demonstration uses 200 fs, 135 μ J pulses from a chirped pulse amplifier system. For comparison, the Ti:Sapph oscillator used in our lab has a pulse energy at its output—before any losses due to optics in the beam path—of 5 nJ in a 10 fs pulse). Freimund et al. observed Kapitza-Dirac scattering of electrons by a standing wave (an effect that could also be used as a coherent amplitude beamsplitter for electrons) using peak intensities of 5×10^{14} W/m² in a 125 μ m focus [14], which corresponds to more than an order of magnitude more power than could be produced by our laser system.

A way around this difficulty is to work with an evanescent optical field. Although an electron in free space cannot absorb a free space photon, an electron can absorb photons in an exponentially decaying evanescent field [87]. This effect was demonstrated in an electron microscope and used to measure a cross-correlation of a 200 fs optical pulse with a 400 fs electron pulse at 200 keV [88]. We propose to modify this technique to directly characterize the electron pulses emitted from one of our laser-triggered field emitters at a small distance from the tip.

5.1 Electron energy gain spectroscopy

In the technique of electron energy loss spectroscopy (EELS), electrons passing through a sample lose energy by a variety of processes including exciting plasmons in nanostructures. In an electron microscope, an image can be formed with the inelastically scattered electrons associated with a particular excitation, mapping its profile [89]. Electron energy gain spectroscopy (EEGS) was proposed as the inverse of this process [87]: a nanostructure is illuminated, and an electron passing nearby can absorb photons in the scattered field. The technique requires high optical intensities; it has been implemented with ultrafast pulses, allowing peak intensities of 10-100 GW/cm² [90]. So that the signal is not overwhelmed by a background of electrons that did not interact, it becomes necessary to also use an ultrafast pulsed electron source [90]. As an electron microscopy technique, EEGS provides new imaging modalities ranging from the ability to resolve plasmonic fields evolving in time [88] to enhanced contrast

in imaging biological samples, which impart only a small phase shift to the electron [90].

In the perturbative limit, the probability of photon absorption is given by [87]

$$P_{\text{EEG}} = \left| \frac{ev \int_{-\infty}^{\infty} E_z(z(t), t) dt}{\hbar\omega} \right|^2, \quad (5.1)$$

where v is the velocity of the electron, $E_z(z(t), t)$ the complex amplitude of the z -component of electric field experienced by the electron along its trajectory, $z(t)$, and $\hbar\omega$ is the photon energy (see Appendix B). The real part of the expression inside the norm has a simple interpretation: it is the ratio of the classical energy gain of the electron in the laser field to the photon energy. The complex amplitude washes out the phase dependence, making the probability a function of the laser intensity envelope and not the electric field [87].

As expected, P_{EEG} is zero for a plane wave. The key prerequisite for photon absorption is not that the light excite a surface plasmon, but rather the existence of sub-wavelength structure in the scattered field, such as an evanescent decay, which allows phase matching between the electron and light [90]. With this in mind, we designed a nanostructured target to optimize the interaction between electrons and light in a cross-correlation geometry, which will be described in the next section.

5.2 Experimental design

5.2.1 Apparatus

A sketch of the laser-electron cross-correlation experiment is shown in Figure 5.1. An optical pulse triggers electron emission from the tip. The electrons are accelerated by a DC electric field and pass through the nanohole target, which is maintained at ≈ 16 kV relative to the tip. They are subsequently decelerated in a long (≈ 8 cm) drift region until they reach the energy analyzer with a kinetic energy of ≈ 50 eV. The energy analyzer consists of a microchannel plate detector (MCP) with two mesh grids in front of it—the grid closest to the MCP has a variable retarding potential

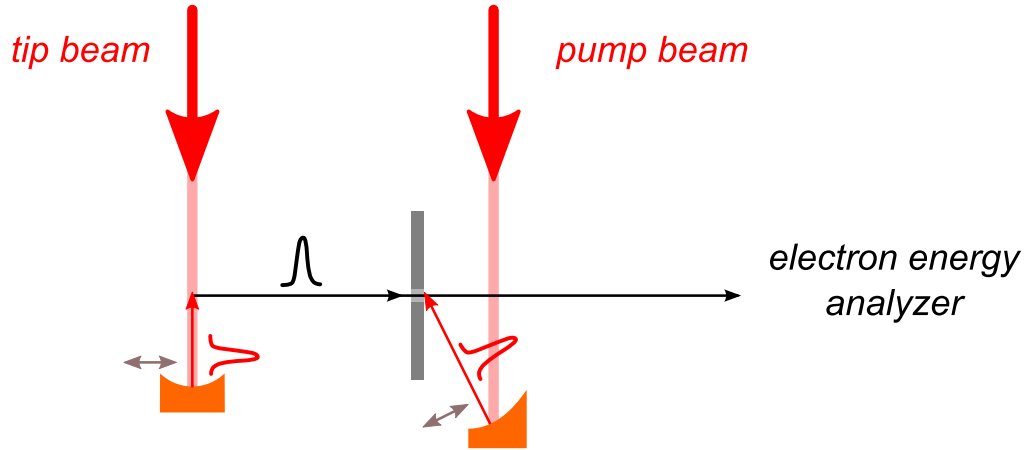


Figure 5.1: Electron-optical cross correlation setup.

applied to it, which blocks electrons with insufficient kinetic energy from reaching the detector. This potential is varied in order to analyze the energy of the electrons. The front grid is grounded so that the electron trajectories in the “drift” region are unaffected by changes in the retarding potential. Magnetic coils outside the chamber are used to approximately zero transverse magnetic fields inside the chamber.

The optical pump pulse is focused on to the back side of the target at an incident angle of 60° . When the pump pulse and the probe (electron) pulse overlap at the nanohole sample, the electrons have a finite probability of absorbing a photon, thus increasing their kinetic energy when they reach the analyzer. The photon absorption probability varies with the time delay between the pump and probe pulse (as will be calculated in detail below), so that scanning the time-delay between the two pulses while measuring the proportion of electrons that absorb a photon results in a cross-correlation measurement.

The tip and pump beam are derived from the same 150 MHz repetition rate Ti:Sapphire laser; the maximum power available in the tip beam and pump beam, respectively, is ~ 70 mW and ~ 260 mW. Both beams are dispersion compensated to deliver < 10 fs pulses inside the chamber. The time-delay between the two pulses is computer-controlled with a Newport picomotor. Due to the small desired optical

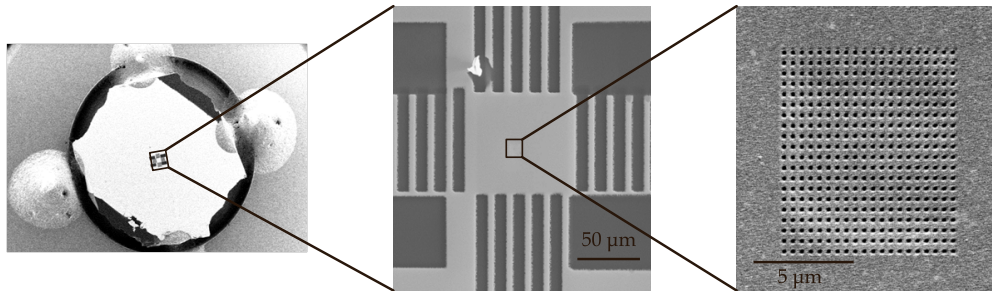


Figure 5.2: SEM image of nanohole target.

beam waist at the tip and nanohole target, the two optical beams must be focused by mirrors inside the vacuum chamber. The tip mirror is spherical, with 4.5 mm focal length. A 30 degree off-axis paraboloid (Edmund optics, 27 mm effective focal length) is used to focus onto the nanohole target, to obtain a spot size of $\sim 30 \mu\text{m}$.

The nanohole target is adhered to a 5.1 mm wide \times 0.6 mm thick stainless steel plate using conductive epoxy. The tip and target are then mounted separately on home-built UHV manipulators, allowing the target to be positioned relative to the electron beam with ~ 10 micron precision. The target can also be removed from the beam so that emission from the tip can be characterized directly.

A scanning electron micrograph of the nanohole target is shown in Figure 5.2. The target is manufactured from a 50 nm thick silicon nitride TEM window (Protochips DuraSiN), which is on a 3.05 mm diameter silicon frame so that it fits in a standard TEM holder. First, a Ga^+ focused ion beam (FIB) is used to mill the nanoholes, which are a 20×20 array of square nanoholes 205 nm on a side, with 425 nm period. Next, a 300 nm thick gold film is evaporated onto the TEM window. SEM images following gold evaporation indicate that the holes are not significantly filled in during evaporation. Finally, a large pattern was milled around the edges of the TEM window (> 25 microns away from the nanohole array on all sides) to assist in visually aligning the pump beam to the nanohole target.

Laser-induced emission in this geometry has been obtained with a 4 keV bias voltage between the tip and nanohole target. We hope to operate the system at 16 keV with a $2.5 \mu\text{m}$ radius of curvature tip, which would increase the interaction

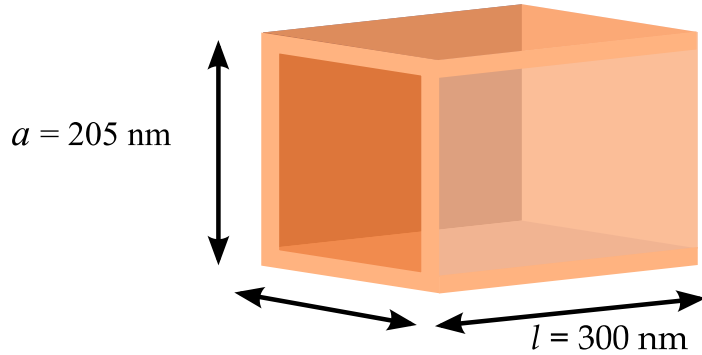


Figure 5.3: Nanohole as waveguide.

probability between the laser and the electrons.

5.2.2 Optical fields in the nanohole target

An individual nanohole is equivalent to a rectangular waveguide of dimensions $a = b = 205 \text{ nm}$ and length $l = 300 \text{ nm}$ (Fig. 5.3). Since we work with light of a free space wavelength around 800 nm, it is immediately clear that the incident light is significantly larger than twice the transverse waveguide dimension, so it cannot propagate in the mode. Instead, the resulting fields are evanescent in the waveguide.

The modes of a perfectly conducting waveguide are derived in electromagnetism textbooks, and we summarize the relevant results here. Solutions to Maxwell's equations in the waveguide can be written as an expansion of transverse magnetic (TM) and transverse electric (TE) mode solutions. The TM modes are the modes for which the longitudinal magnetic field (along the axis of the waveguide) is zero. In this case, the electric field has a longitudinal component.

Conversely, the TE modes have a non-zero longitudinal magnetic field but no longitudinal electric field. Consider the waveguide shown in Figure 5.3. The z -axis is taken in the longitudinal direction, and we allow $a \neq b$ for the time being. The

modes are assumed to be of the form

$$\begin{aligned}\mathbf{E}(x, y, z, t) &= \mathbf{E}(x, y) \exp(i(kz - \omega t)) \\ \mathbf{B}(x, y, z, t) &= \mathbf{B}(x, y) \exp(i(kz - \omega t)).\end{aligned}\quad (5.2)$$

It can be shown that the E_z and B_z must satisfy the wave equations

$$\begin{aligned}\left[\frac{\partial^2}{\partial x^2} + \frac{\partial^2}{\partial y^2} + \left(\frac{\omega}{c}\right)^2 - k^2 \right] E_z &= 0 \\ \left[\frac{\partial^2}{\partial x^2} + \frac{\partial^2}{\partial y^2} + \left(\frac{\omega}{c}\right)^2 - k^2 \right] B_z &= 0\end{aligned}\quad (5.3)$$

The electric field in the TM modes is given by

$$E_z = E_0 \sin\left(\frac{m\pi x}{a}\right) \sin\left(\frac{n\pi y}{b}\right) \quad (5.4a)$$

$$E_x = \frac{ik}{(\omega/c)^2 - k^2} \frac{\partial E_z}{\partial x} \quad (5.4b)$$

$$E_y = \frac{ik}{(\omega/c)^2 - k^2} \frac{\partial E_z}{\partial y}, \quad (5.4c)$$

with m and n non-negative integers (and at least one of them non-zero). The longitudinal magnetic field of the TE modes is

$$B_z = B_0 \cos\left(\frac{m\pi x}{a}\right) \cos\left(\frac{n\pi y}{b}\right), \quad (5.5)$$

and the electric field is

$$E_z = 0 \quad (5.6a)$$

$$E_x = \frac{i\omega}{(\omega/c)^2 - k^2} \frac{\partial B_z}{\partial y} \quad (5.6b)$$

$$E_y = \frac{i\omega}{(\omega/c)^2 - k^2} \frac{\partial B_z}{\partial x}. \quad (5.6c)$$

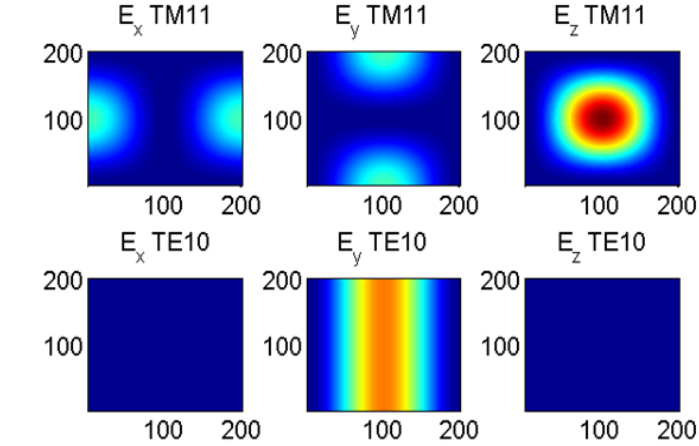


Figure 5.4: Transverse profiles of the two lowest nanohole modes.

Substituting equations 5.4a and 5.5 into equation 5.3 shows that, for a given mode and a given value of ω , k must satisfy

$$k = k_{mn} \equiv \sqrt{k_0^2 - \pi^2 \left(\left(\frac{m}{a} \right)^2 + \left(\frac{n}{b} \right)^2 \right)} \quad (5.7)$$

where k_0 is the free space wave vector, $k_0 = 2\pi/\lambda_0 = \omega/c$. For our purposes, we will always have $a = b < \lambda/2$, so that k inside the waveguide is always imaginary, and the amplitude of the field in a particular mode decays exponentially in z . Corrections due to the finite skin depth of gold might reduce the decay length, which actually increases the probability that the electron can absorb a photon.

5.2.3 Probability of photon absorption

We can use the explicit form of the fields in the previous section to compute the probability of photon absorption in the perturbative regime. If we define an effective interaction length,

$$l_{\text{eff}}(\Delta t) \equiv v \left| \int_{-\infty}^{\infty} \frac{E_z(z(t), t)}{E_p} dt \right|, \quad (5.8)$$

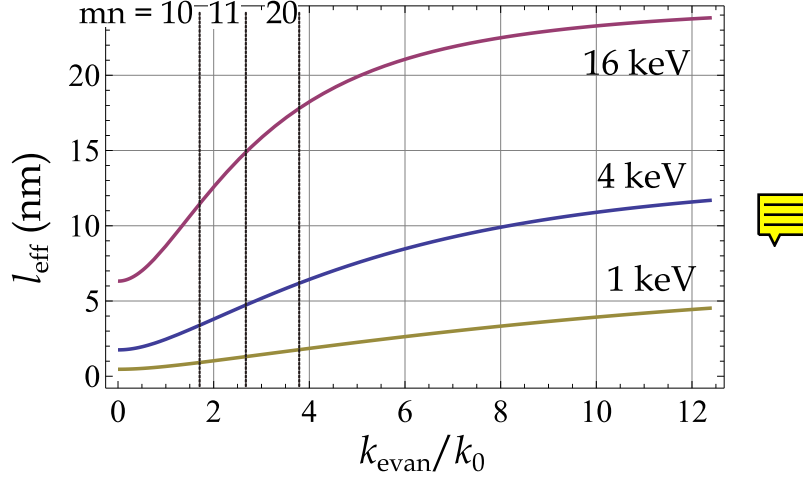


Figure 5.5: Maximum interaction length for electron energy gain (calculated for a gaussian optical pulse with 10 fs FWHM), as a function of the ratio of the norm of the evanescent wavevector k_{evan} and the free space wavevector k_0 . k_{evan}/k_0 of the three lowest modes of the 205 nm square nanohole are shown. Curves are plotted for initial electron energies of 1, 4, and 16 keV.

then Eq. 5.1 can be rewritten as

$$P_{\text{EEG}}(\Delta t) = \left(\frac{eE_p l_{\text{eff}}(\Delta t)}{\hbar\omega} \right)^2. \quad (5.9)$$

E_p is the peak laser electric field. Dependence on Δt , the time delay between the electron and optical pulse, enters through the expression for the electron trajectory, $z(t)$ and the laser electric field, $E_z(z, t)$. Figure 5.5 shows a plot of this effective interaction length at optimal temporal overlap with a 10 fs FWHM optical pulse, for a few values of initial electron kinetic energy.

The simulated probability of photon absorption vs. Δt is shown in Fig. 5.6. The calculation is done for a 4 keV trajectory at the center of the nanohole, assuming a 1.7 nJ pulse focused to 300 μm exciting the lowest order mode of the nanohole with 100% efficiency.

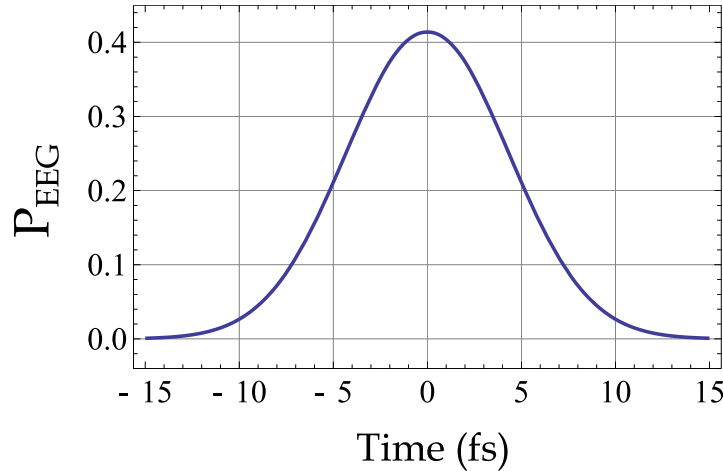


Figure 5.6: Probability of electron absorption vs. time delay between the electron and the optical pulse at the center of the nanohole, calculated assuming 100% coupling efficiency into the lowest order for reasonable experimental parameters: electron energy of 4 keV, and a 1.7 nJ, 10 fs FWHM pulse focused to a 30 μm waist. The cross-correlation is the convolution of this curve with the electron pulse profile.

Table 5.1: Contributions to pulse broadening at the target

Electron pulse	
Initial pulse	10 fs
On-axis kinematic broadening	1.3 fs
Geometrical broadening (5 mrad, 16 keV)	0.9 fs
Power supply fluctuations (16 keV)	0.7 fs/V

Optical pulse	
Pulse duration	10 fs
Propagation delay across target	25 fs



5.2.4 Pulse duration at the interaction region

The dispersion of the material elements in the beam-line (vacuum window, half wave plates, polarizers, air) is compensated using double-chirped mirrors to ensure short optical pulses at the tip and nanohole target. Table 5.1 summarizes contributions to the electron and optical pulse duration at the target. For the electrons, kinematic broadening was calculated numerically, integrating axial trajectories for 16 kV applied to a 2.5 μm tip and assuming an initial energy spread of 0.3 eV. Geometrical broadening was calculated for straight-line trajectories of 16 keV electrons with an opening angle of 5 mrad set by the 8 μm target size and the 1.5 mm distance from tip to the target. Broadening due to the propagation time of the laser across the target could be eliminated with tilted pulse fronts.

5.2.5 Signal to noise considerations

The energy spectrum is a convolution of the true electron spectrum with the instrument response. Assume (for ease of calculation) a gaussian spectral shape, with FWHM ΔE . The number of electrons arriving with energies between E and $E + \delta E$ is

$$g(E)\delta E = N f\left(\frac{E}{\Delta E}\right) \frac{\delta E}{\Delta E}, \quad (5.10)$$

where

$$f(x) \equiv 2\sqrt{\frac{\log 2}{\pi}} \exp(-4\log(2)x^2) \quad \text{█} \quad (5.11)$$

The function f has been normalized so that N is the total number of electrons in the spectrum. The signal we are looking for is a copy of this spectrum shifted by the photon energy, $\hbar\omega$. If the fraction of electrons that absorb a photon is α , then the expected signal is

$$\alpha g(E - \hbar\omega)\delta E. \quad (5.12)$$

This signal sits on top of a background of electrons that did not interact. The shot noise from this signal is approximately

$$\sqrt{g(E)\delta E} \quad \text{█} \quad (5.13)$$

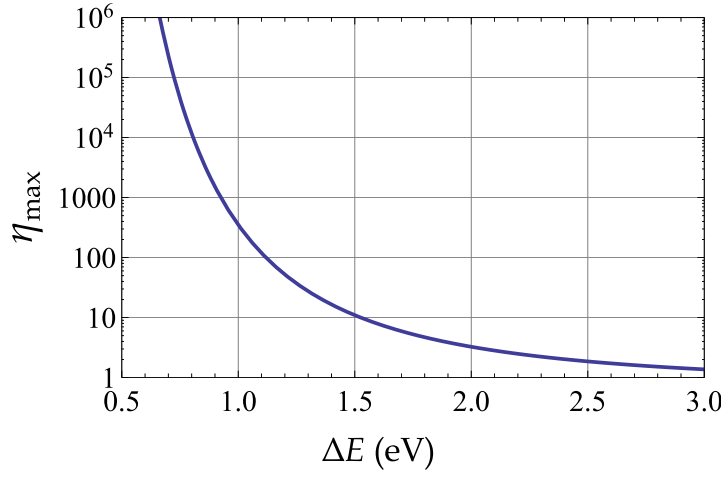


Figure 5.7: Energy resolution and signal-to-noise. η_{\max} is a dimensionless number related to the signal-to-noise for detecting the electron energy gain signal (see text). Here, it is plotted vs. energy resolution assuming a photon energy of 1.5 eV.

The signal-to-noise ratio is

$$S/N \approx \left[\frac{N\delta E}{\Delta E} \right]^{1/2} \frac{f((E - \hbar\omega)/\Delta E)}{[f(E/\Delta E)]^{1/2}} \equiv \left[\frac{N\delta E}{\Delta E} \right]^{1/2} \eta(E, \Delta E, \hbar\omega). \quad (5.14)$$

The factor of $(\delta E/\Delta E)^{1/2}$ gives the reduction in signal to noise if one reduces the bin size relative to ΔE . The second term shows, not too surprisingly, that it is advantageous to make the width of the spectrum smaller than the shift that we want to measure. Assuming that we always measure at the value of E that maximizes η , we have

$$S/N \approx \left[\frac{N\delta E}{\Delta E} \right]^{1/2} \eta_{\max}(\Delta E, \hbar\omega). \quad (5.15)$$

Figure 5.7 shows η_{\max} as a function of ΔE for a 1.5 eV photon energy. The energy resolution of the energy analysis we have used so far is optimistically 1.5 eV; if this were improved even to 1 eV, the signal-to-noise due to shot noise of the primary electron beam would improve by nearly three orders of magnitude.



Appendix A

Annealing procedure

The annealing procedure is shown in Table A.1. The temperature of the tip as a function of current through the support loop varies slightly from one tip assembly to the next; we normally calibrate this initially using optical pyrometry to determine the tip temperature, and subsequently anneal by monitoring the support loop current, without directly measuring the temperature. This is less accurate, since it requires some time for the tip to reach its equilibrium temperature for a given current. To improve the accuracy with which we hit the desired anneal temperature, each time the tip is flashed, the current is initially held at 2.5 A ($T \lesssim 1000$ K) until the temperature (as determined by the resistance of the support loop) stabilizes.

Sugata and Tamaki have performed a systematic field ion microscope study of the

Approximate temperature	Current through support loop	Time
1750 K	2.9 A	2 s
1350 K	2.75 A	4 s
1200 K	2.65 A	4 s

Table A.1: Anneal procedure. The values of the current through the support loop are given for a specific tip—the value required to achieve the specified temperatures varies slightly from one tip assembly to another and must be calibrated. The tip is flashed three times, with the support loop current raised initially to about 2.5 A (≈ 1000 K once the temperature has stabilized) before increasing the current to the set value, as described in the text.

effects of different anneal temperatures on the atomic structure of the tungsten surface [91]. They found that between 1800 and 2200 K, annealing led to blunting of the tip and the introduction of disorder in the atomic layers nearest to the surface, especially for (111)-oriented crystal planes. Furthermore, they found that between 1200 K and 1800 K, the surface obtained by simple annealing was indistinguishable from that obtained by field evaporation followed by annealing at the same temperature [91]. Thus the initial 1750 K anneal is designed to desorb as many contaminants as possible without introducing additional disorder to the tungsten surface. The lower temperature anneals came from the observation that we obtained more consistent start voltages and symmetric emission patterns after annealing at low temperatures. The start voltage measured immediately after annealing can stay constant over months of daily operation of the experiment indicating that the surface can be repeatably brought to the same state of cleanliness and that the anneal procedure and laser illumination do not significantly change the tip geometry.

Oxygen etching of (111)-oriented field emitters. (111)-oriented tungsten field emitters can be sharpened *in situ* by oxygen etching. Heating the tungsten in the presence of oxygen at low pressure forms oxides on the tungsten surface that sublime at comparatively low (1200 K-2000 K) temperatures [92]. The etching process happens at different rates for different crystal orientations, such that a (111)-oriented field emitter is etched symmetrically and can be controllably sharpened. Kim et al. find a tungsten removal rate of 1.3 nm/min working at an oxygen pressure of $4 \times 10^{-5} \text{ torr}$ and a temperature of 1650 K and, evidently, the etching rate increases with increasing temperature and/or oxygen pressure. In our vacuum system, the oxygen pressure measured by the ion gauge (applying the correct sensitivity factor), which is near the tip, and the RGA, which is far away, were different by over an order of magnitude. We found a reasonable working pressure by alternating oxygen etching with annealing under vacuum and re-checking the start voltage of the tip to monitor whether the tip radius had changed appreciably.

Appendix B

Probability of photon absorption by an electron in the perturbative limit

B.1 Monochromatic field

See review article, F. J. Garcia de Abajo, “Optical excitations in electron microscopy” (Rev. Mod. Phys. Vol. 82, No. 1 p. 248) [93] as well as [87]. This section will summarize the problem for a monochromatic optical field, with photon energy $\hbar\omega$, following the derivation in [93]. In the next section, we’ll try to generalize the argument to come up with an analogous solution for an optical pulse.

Using first-order perturbation theory, look for a solution of the form

$$\psi_{\parallel}(z, t) = \frac{1}{L^{1/2}} e^{ip_i z} e^{-i\epsilon_i t} + \delta\psi_{\parallel}(z) e^{-i\epsilon_f t}. \quad (\text{B.1})$$

The incoming wave is a plane wave with momentum p_i , energy $\hbar\epsilon_i$. The first term is normalized so that

$$\int_{z_0-L/2}^{z_0+L/2} |\psi|^2 dz = \frac{1}{L} \int_{z_0-L/2}^{z_0+L/2} |\exp(i(p_i z - \epsilon_i t))|^2 dz = 1. \quad (\text{B.2})$$

The energy of the final state is $\hbar\epsilon_f = \hbar\epsilon_i + \hbar\omega$. Following reference [93],

$$\delta\psi_{\parallel} = \int dz' G_f(z - z') H_{\omega}(z') \frac{e^{ip_i z'}}{L^{1/2}}, \quad (\text{B.3})$$

where

$$H_{\omega}(z) = \frac{-e\hbar}{m_e\omega} E_z(\mathbf{R}_0, z) \partial_z \quad (\text{B.4})$$

is the relevant part of the electron-light interaction term in the Hamiltonian, and

$$G_f(z - z') = \int \frac{dp}{2\pi} \frac{e^{ip(z-z')}}{\hbar\epsilon_f - (\hbar^2 p^2/2m_e) + i0^+} = -\frac{im_e}{p_f\hbar^2} e^{ip_f|z-z'|} \quad (\text{B.5})$$

is the non-relativistic Green's function of the free electron propagating along the z direction with final energy $\hbar\epsilon_f$. Making these substitutions, we obtain

$$\delta\psi_{\parallel}(z) e^{-i\epsilon_f t} = -\frac{e}{\hbar\omega} \frac{p_i}{p_f} \frac{e^{-i\epsilon_f t}}{L^{1/2}} \int dz' \exp(i(p_i - p_f)z') \exp(ip_f z) E_z(\mathbf{R}_0, z'; \omega), \quad (\text{B.6})$$

which becomes

$$\delta\psi_{\parallel}(z) e^{-i\epsilon_f t} = -\frac{e}{\hbar\omega} \frac{p_i}{p_f} \frac{e^{-i\epsilon_f t} e^{ip_f z}}{L^{1/2}} \int dz' \exp(i\omega z'/v) E_z(\mathbf{R}_0, z'; \omega). \quad (\text{B.7})$$

with the approximations $p_i \approx p_f$ and $p_f - p_i \approx \omega/v$. In deriving Eq. B.6, the absolute value of $z - z'$ in the Green's function was dropped by assuming that $z > z'$. This is the case because we evaluate $\delta\psi_{\parallel}(z)$ far away from the scatterer, where the scattered field has gone to zero so that the integrand ~ 0 everywhere that the condition $z > z'$ doesn't hold. We are interested in the coefficient A where

$$\delta\psi_{\parallel}(z) e^{-i\epsilon_f t} = A\phi(z, t) \quad (\text{B.8})$$

and $\phi(z, t)$ satisfies the normalization condition B.2. In this case, $|A|^2$ is the probability that the electron absorbed a photon. By inspection, we should take

$$\phi(z, t) = \frac{1}{L^{1/2}} e^{-i(\epsilon_f t + p_f z)}, \quad (\text{B.9})$$

and the transition probability is

$$P_{\text{EEG}} = |A|^2 = \left(\frac{e}{\hbar\omega} \right)^2 \left| \int dz' e^{-i\omega z'/v} E_z(\mathbf{R}_0, z'; \omega) \right|^2, \quad (\text{B.10})$$

which is Eq. 67 of reference [93].

B.2 Time-domain expression

Proceeding in the same manner, we allow the optical field to be broadband. We want

$$\psi_{\parallel}(z, t) = \frac{1}{L^{1/2}} e^{ip_i z} e^{-i\epsilon_i t} + A\phi(z, t) \quad (\text{B.11})$$

with $\phi(z, t)$ normalized. Since the source is now broadband, and since the perturbation theory argument is completely linear in the optical field, we now have

$$A\phi(z, t) = \delta\psi_{\parallel}(z, t) = e^{-i\epsilon_i t} \int_0^{\infty} d\omega e^{-i\omega t} \int dz' G_f(z - z') H_{\omega}(z') \frac{e^{ip_i z'}}{L^{1/2}}. \quad (\text{B.12})$$

Making the same substitutions and approximations as before, and assuming a narrow enough spectrum that ω_0 , the center frequency of the pulse, can be factored out of the integral,

$$A\phi(z, t) = \frac{-e}{\hbar\omega_0} \frac{1}{L^{1/2}} \int d\omega \int_0^{\infty} dz' E_z(\mathbf{R}_0, z'; \omega) \exp(-i\omega(t + \frac{z' - z}{v})). \quad (\text{B.13})$$

Switching the order of integration,

$$A\phi(z, t) = -\frac{e}{\hbar\omega_0} \frac{1}{L^{1/2}} e^{ip_i z} \int dz' \int_0^{\infty} d\omega E_z(\mathbf{R}_0, z'; \omega) \exp(-i\omega(t + \frac{z' - z}{v})). \quad (\text{B.14})$$

However, the quantity in the second integral is simply an inverse Fourier transform over positive frequencies, i.e. it is equal to

$$E_z^+(\mathbf{R}_0, z'; t') = E_z(\mathbf{R}_0, z'; t') + E'_z(\mathbf{R}_0, z'; t') \quad (\text{B.15})$$

with $t' = t + (z' - z)/v$ and E'_z the Hilbert transform of E_z . As a result,

$$A\phi(z, t) = -\frac{e}{\hbar\omega_0} \frac{1}{L^{1/2}} e^{ip_i z} \int dz' E_z^+(\mathbf{R}_0, z'; t + (z' - z)/v) \quad (\text{B.16})$$

and

$$P_{\text{EEG}}(t) = |A|^2 = \left(\frac{e}{\hbar\omega}\right)^2 \frac{1}{L} \int_{z_0-L/2}^{z_0+L/2} dz \left| \int dz' E_z^+(\mathbf{R}_0, z'; t + (z' - z)/v) \right|^2. \quad (\text{B.17})$$

B.2.1 Classical energy increase

The change in momentum is given by

$$\Delta p = \int \frac{e}{v} E_z \left(\mathbf{R}_0, z'; t + \frac{z'}{v} \right) dz'. \quad (\text{B.18})$$

And the energy increase is simply $v\Delta p$ (as long as $\Delta p \ll p$), so that the energy gained by the electron is simply

$$\Delta E = e \int E_z \left(\mathbf{R}_0, z'; t + \frac{z'}{v} \right) dz'. \quad (\text{B.19})$$

This means that P_{EEG} has an extremely simple relationship to the classical energy gain:

$$P_{\text{EEG}} = \left(\frac{\Delta E_{cl}}{\hbar\omega} \right)^2, \quad (\text{B.20})$$

where ΔE_{cl} is interpreted as the envelope of ΔE .

$$P(t) = \left(\frac{e}{\hbar\omega} \right)^2 \left| \int_{\substack{\text{along} \\ \text{trajectory}}} dz [E_z(\mathbf{r}, z, t) + iE'_z(\mathbf{r}, z, t)] \right|^2. \quad (\text{B.21})$$

Bibliography

- [1] G. Mourou and S. Williamson, “Picosecond electron diffraction,” *Appl. Phys. Lett.*, vol. 41, no. 1, pp. 44–45, 1982.
- [2] G. Sciaiani and R. J. D. Miller, “Femtosecond electron diffraction: heralding the era of atomically resolved dynamics,” *Rep. Prog. Phys.*, vol. 74, no. 9, p. 096101, 2011.
- [3] A. H. Zewail, “4D ultrafast electron diffraction, crystallography, and microscopy,” *Annu. Rev. Phys. Chem.*, vol. 57, pp. 65–103, 2006.
- [4] M. J. G. Lee, “Field emission of hot electrons from tungsten,” *Phys. Rev. Lett.*, vol. 30, no. 24, p. 1193, 1973.
- [5] D. Venus and M. J. Lee, “Photofield emission spectroscopy of surface electronic states of tungsten,” *Surf. Sci.*, vol. 172, no. 2, pp. 477–495, 1986.
- [6] P. Hommelhoff, Y. Sortais, A. Aghajani-Talesh, and M. A. Kasevich, “Field emission tip as a nanometer source of free electron femtosecond pulses,” *Phys. Rev. Lett.*, vol. 96, p. 077401, 2006.
- [7] C. Ropers, D. R. Solli, C. P. Schulz, C. Lienau, and T. Elsaesser, “Localized multiphoton emission of femtosecond electron pulses from metal nanotips,” *Phys. Rev. Lett.*, vol. 98, p. 043907, 2007.
- [8] F. Hasselbach, “Progress in electron- and ion-interferometry,” *Reports on Progress in Physics*, vol. 73, no. 1, p. 016101, 2010.

- [9] P. Hommelhoff, C. Kealhofer, and M. A. Kasevich, "Ultrafast electron pulses from a tungsten tip triggered by low-power femtosecond laser pulses," *Phys. Rev. Lett.*, vol. 97, p. 247402, 2006.
- [10] M. Kruger, M. Schenk, and P. Hommelhoff, "Attosecond control of electrons emitted from a nanoscale metal tip," *Nature*, vol. 475, no. 7354, pp. 78–81, 2011.
- [11] T. Plettner, R. L. Byer, C. McGuinness, and P. Hommelhoff, "Photonic-based laser driven electron beam deflection and focusing structures," *Phys. Rev. ST Accel. Beams*, vol. 12, p. 101302, Oct 2009.
- [12] S. M. Foreman, C. Kealhofer, G. E. Skulason, B. B. Klopfer, and M. A. Kasevich, "Ultrafast microfocus x-ray source based on a femtosecond laser-triggered tip," *Annalen der Physik*, vol. 525, no. 1-2, pp. L19–L22, 2013.
- [13] A. Caprez, B. Barwick, and H. Batelaan, "Macroscopic test of the Aharonov-Bohm effect," *Phys. Rev. Lett.*, vol. 99, no. 21, p. 210401, 2007.
- [14] D. L. Freimund, K. Aflatooni, and H. Batelaan, "Observation of the Kapitza-Dirac effect," *Nature*, vol. 413, pp. 142–143, 2001.
- [15] R. Bormann, M. Gulde, A. Weismann, S. V. Yalunin, and C. Ropers, "Tip-enhanced strong-field photoemission," *Phys. Rev. Lett.*, vol. 105, no. 14, p. 147601, 2010.
- [16] P. Hommelhoff Private communication., 2011.
- [17] J. Humphries, Stanley, *Charged Particle Beams*. 1990.
- [18] K.-J. Kim, "Characteristics of synchrotron radiation," *AIP Conference Proceedings*, vol. 184, no. 1, pp. 565–632, 1989.
- [19] M. Schenk, M. Krüger, and P. Hommelhoff, "Strong-field above-threshold photoemission from sharp metal tips," *Phys. Rev. Lett.*, vol. 105, no. 25, p. 257601, 2010.

- [20] E. Fill, L. Veisz, A. Apolonski, and F. Krausz, “Sub-fs electron pulses for ultrafast electron diffraction,” *New Journal of Physics*, vol. 8, no. 11, p. 272, 2006.
- [21] P. W. Hawkes and E. Kasper, *Principles of Electron Optics*, vol. 2, ch. 44-45. Academic Press, 1989.
- [22] A. Gahlmann, S. T. Park, and A. H. Zewail, “Ultrashort electron pulses for diffraction, crystallography and microscopy: theoretical and experimental resolutions,” *Phys. Chem. Chem. Phys.*, vol. 10, pp. 2894–2909, 2008.
- [23] R. Ernstorfer, M. Harb, C. T. Hebeisen, G. Sciaiani, T. Dartigalongue, and R. J. D. Miller, “The formation of warm dense matter: experimental evidence for electronic bond hardening in gold,” *Science*, vol. 323, no. 5917, pp. 1033–1037, 2009.
- [24] R. Ganter, R. Bakker, C. Gough, S. C. Leemann, M. Paraliev, M. Pedrozzi, F. Le Pimpec, V. Schlott, L. Rivkin, and A. Wrulich, “Laser-photofield emission from needle cathodes for low-emittance electron beams,” *Phys. Rev. Lett.*, vol. 100, no. 6, pp. 064801–4, 2008.
- [25] K. L. Jensen, P. G. O’Shea, D. W. Feldman, and J. L. Shaw, “Emittance of a field emission electron source,” *J. Appl. Phys.*, vol. 107, p. 014903, 2010.
- [26] B. Cook, T. Verduin, C. W. Hagen, and P. Kruit, “Brightness limitations of cold field emitters caused by coulomb interactions,” in *J. Vac. Sci. Tech. B, Papers from the 54th International Conference on Electron, Ion, and Photon Beam Technology and Nanofabrication*, vol. 28, pp. C6C74–C6C79, AVS, 2010.
- [27] B. Cho, T. Ichimura, R. Shimizu, and C. Oshima, “Quantitative evaluation of spatial coherence of the electron beam from low temperature field emitters,” *Phys. Rev. Lett.*, vol. 92, no. 24, p. 246103, 2004.
- [28] C. Brau, “High-brightness photoelectric field-emission cathodes for free-electron laser applications,” *Nucl. Instrum. Meth. A*, vol. 393, pp. 426 – 429, 1997.

- [29] J. D. Jarvis, H. L. Andrews, B. Ivanov, C. L. Stewart, N. de Jonge, E. C. Heeres, W.-P. Kang, Y.-M. Wong, J. L. Davidson, and C. A. Brau, “Resonant tunneling and extreme brightness from diamond field emitters and carbon nanotubes,” *J. Appl. Phys.*, vol. 108, no. 9, p. 094322, 2010.
- [30] T. van Oudheusden, E. F. de Jong, S. B. van der Geer, W. P. E. M. O. ’t Root, O. J. Luiten, and B. J. Siwick, “Electron source concept for single-shot sub-100 fs electron diffraction in the 100 keV range,” *J. Appl. Phys.*, vol. 102, no. 9, p. 093501, 2007.
- [31] T. van Oudheusden, P. L. E. M. Pasmans, S. B. van der Geer, M. J. de Loos, M. J. van der Wiel, and O. J. Luiten, “Compression of subrelativistic space-charge-dominated electron bunches for single-shot femtosecond electron diffraction,” *Phys. Rev. Lett.*, vol. 105, p. 264801, 2010.
- [32] A. Gliserin, A. Apolonski, F. Krausz, and P. Baum, “Compression of single-electron pulses with a microwave cavity,” *New J. Phys.*, vol. 14, no. 7, p. 073055, 2012.
- [33] P. Baum and A. H. Zewail, “4D attosecond imaging with free electrons: Diffraction methods and potential applications,” *Chemical Physics*, vol. 366, no. 13, pp. 2–8, 2009.
- [34] E. A. Peralta, K. Soong, R. J. England, E. R. Colby, B. Montazeri, Z. Wu, C. McGuinness, J. McNeur, and R. L. Byer, “High-gradient (beyond 250 MeV/m) acceleration of electrons in a laser-driven dielectric micro-structure.” 2013.
- [35] B. J. Siwick, J. R. Dwyer, R. E. Jordan, and R. J. D. Miller, “Ultrafast electron optics: Propagation dynamics of femtosecond electron packets,” *J. Appl. Phys.*, vol. 92, no. 3, pp. 1643–1648, 2002.
- [36] C. Herring and M. H. Nichols, “Thermionic emission,” *Rev. Mod. Phys.*, vol. 21, pp. 185–270, 1949.

- [37] K. L. Jensen, P. G. O'Shea, and D. W. Feldman, "Generalized electron emission model for field, thermal, and photoemission," *Appl. Phys. Lett.*, vol. 81, no. 20, pp. 3867–3869, 2002.
- [38] R. Gomer, *Field Emission and Field Ionization*. No. 9 in Harvard monographs in applied science, Cambridge: Harvard University Press, 1961.
- [39] E. L. Murphy and R. H. Good, "Thermionic emission, field emission, and the transition region," *Phys. Rev.*, vol. 102, no. 6, pp. 1464–1473, 1956.
- [40] R. Smoluchowski, "Anisotropy of the electronic work function of metals," *Phys. Rev.*, vol. 60, pp. 661–674, 1941.
- [41] T. C. Leung, C. L. Kao, W. S. Su, Y. J. Feng, and C. T. Chan, "Relationship between surface dipole, work function and charge transfer: Some exceptions to an established rule," *Phys. Rev. B*, vol. 68, p. 195408, 2003.
- [42] R. G. Forbes and J. H. B. Deane, "Reformulation of the standard theory of Fowler-Nordheim tunnelling and cold field electron emission," *Proc. R. Soc. A*, vol. 463, pp. 2907–2927, 2007.
- [43] C. Kealhofer, S. M. Foreman, S. Gerlich, and M. A. Kasevich, "Ultrafast laser-triggered emission from hafnium carbide tips," *Phys. Rev. B*, vol. 86, p. 035405, 2012.
- [44] D. Venus and M. Lee, "Polarization dependence of photoexcitation in photofield emission," *Surf. Sci.*, vol. 125, no. 2, pp. 452–472, 1983.
- [45] H. Yanagisawa, M. Hengsberger, D. Leuenberger, M. Klöckner, C. Hafner, T. Greber, and J. Osterwalder, "Energy distribution curves of ultrafast laser-induced field emission and their implications for electron dynamics," *Phys. Rev. Lett.*, vol. 107, no. 8, p. 087601, 2011.
- [46] P. Hommelhoff, C. Kealhofer, A. Aghajani-Talesh, Y. R. Sortais, S. M. Foreman, and M. A. Kasevich, "Extreme localization of electrons in space and time,"

- Ultramicroscopy*, vol. 109, no. 5, pp. 423–429, 2009. IFES 2008 Proceedings of the 51th International Field Emission Symposium.
- [47] J. P. Girardeau-Montaut and C. Girardeau-Montaut, “Theory of ultrashort nonlinear multiphoton photoelectric emission from metals,” *Phys. Rev. B*, vol. 51, no. 19, pp. 13560–13567, 1995.
 - [48] Y. C. Martin, H. F. Hamann, and H. K. Wickramasinghe, “Strength of the electric field in apertureless near-field optical microscopy,” *J. Appl. Phys.*, vol. 89, no. 10, p. 5774, 2001.
 - [49] H. Yanagisawa, C. Hafner, P. Doná, M. Klöckner, D. Leuenberger, T. Greber, J. Osterwalder, and M. Hengsberger, “Laser-induced field emission from a tungsten tip: Optical control of emission sites and the emission process,” *Phys. Rev. B*, vol. 81, no. 11, p. 115429, 2010.
 - [50] L. Xu, C. Spielmann, A. Poppe, T. Brabec, F. Krausz, and T. W. Hänsch, “Route to phase control of ultrashort light pulses,” *Opt. Lett.*, vol. 21, no. 24, pp. 2008–2010, 1996.
 - [51] P. Dombi, F. Krausz, and G. Farkas, “Ultrafast dynamics of multiphoton photoemission from gold and carrier-envelope phase sensitivity,” in *Advanced Solid-State Photonics*, p. WB28, Optical Society of America, 2005.
 - [52] using the software package Comsol version 3.5a, Comsol AB, Sweden, 2009.
 - [53] H. Yanagisawa, C. Hafner, P. Doná, M. Klöckner, D. Leuenberger, T. Greber, M. Hengsberger, and J. Osterwalder, “Optical control of field-emission sites by femtosecond laser pulses,” *Phys. Rev. Lett.*, vol. 103, no. 25, p. 257603, 2009.
 - [54] P. Hommelhoff, C. Kealhofer, and M. Kasevich, “Femtosecond laser meets field emission tip—a sensor for the carrier envelope phase,” in *2006 IEEE International Frequency Control Symposium and Exposition*, pp. 470–474, 2006.
 - [55] G. L. Yudin and M. Y. Ivanov, “Nonadiabatic tunnel ionization: Looking inside a laser cycle,” *Phys. Rev. A*, vol. 64, no. 1, p. 013409, 2001.

- [56] K. Vestentoft and P. Balling, “Formation of an extended nanostructured metal surface by ultra-short laser pulses: single-pulse ablation in the high-fluence limit,” *Appl. Phys. A: Mater. Sci. Process.*, vol. 84, pp. 207–213, 2006.
- [57] H.-S. Rhie, H. A. Dürr, and W. Eberhardt, “Femtosecond electron and spin dynamics in Ni/W(110) films,” *Phys. Rev. Lett.*, vol. 90, p. 247201, 2003.
- [58] S. I. Anisimov, B. L. Kapeliovich, and T. L. Perel’man, “Electron emission from metal surfaces exposed to ultrashort laser pulses,” *Sov. Phys. - JETP*, vol. 39, pp. 375–377, 1974.
- [59] B. Rethfeld, A. Kaiser, M. Vicanek, and G. Simon, “Ultrafast dynamics of nonequilibrium electrons in metals under femtosecond laser irradiation,” *Phys. Rev. B*, vol. 65, 2002.
- [60] S. Zaima, H. Adachi, and Y. Shibata, “Promising cathode materials for high brightness electron beams,” *J. Vac. Sci. Technol. B*, vol. 2, no. 1, pp. 73–78, 1984.
- [61] H. O. Pierson, *Handbook of Refractory Carbides and Nitrides*. Westwood, N. J.: Noyes Publications, 1996.
- [62] P. J. Linstrom and W. G. Mallard, eds., *NIST Chemistry WebBook, NIST Standard Reference Database Number 69*. Gaithersburg, MD: National Institute of Standards and Technology, 2011.
- [63] Y. Takahashi and H. Akiyama, “Heat capacity of gold from 80 to 1000 K,” *Thermochim. Acta*, vol. 109, no. 1, pp. 105 – 109, 1986.
- [64] H. Ihara, M. Hirabayashi, and H. Nakagawa, “Electronic band structures and x-ray photoelectron spectra of ZrC, HfC, and TaC,” *Phys. Rev. B*, vol. 14, no. 4, pp. 1707–1714, 1976.
- [65] Z. Lin, L. V. Zhigilei, and V. Celli, “Electron-phonon coupling and electron heat capacity of metals under conditions of strong electron-phonon nonequilibrium,” *Phys. Rev. B*, vol. 77, no. 7, p. 075133, 2008.

- [66] E. Wuchina, M. Opeka, S. Causey, K. Buesking, J. Spain, A. Cull, J. Routbort, and F. Guitierrez-Mora, “Designing for ultrahigh-temperature applications: The mechanical and thermal properties of HfB_2 , HfC_x , HfN_x and $\alpha\text{Hf}(\text{N})$,” *J. Mater. Sci.*, vol. 39, pp. 5939–5949, 2004.
- [67] W. M. Haynes and D. R. Lide, eds., *CRC Handbook of Chemistry and Physics*. Boca Raton, FL: CRC Press, 92 ed., 2011.
- [68] B. Christensen, K. Vestentoft, and P. Balling, “Short-pulse ablation rates and the two-temperature model,” *Appl. Surf. Sci.*, vol. 253, no. 15, pp. 6347–6352, 2007. Proceedings of the Fifth International Conference on Photo-Excited Processes and Applications.
- [69] F. W. Flück, H. P. Geserich, and C. Politis, “Optical investigations on $\text{HfC}_x\text{N}_{(1-x)}$ compounds,” *Phys. Status Solidi B*, vol. 112, pp. 193–200, 1982.
- [70] P. B. Johnson and R. W. Christy, “Optical constants of the noble metals,” *Phys. Rev. B*, vol. 6, pp. 4370–4379, 1972.
- [71] A. D. Rakic, A. B. Djurišić, J. M. Elazar, and M. L. Majewski, “Optical properties of metallic films for vertical-cavity optoelectronic devices,” *Appl. Opt.*, vol. 37, no. 22, pp. 5271–5283, 1998.
- [72] M. J. G. Lee, R. Reifenberger, E. S. Robins, and H. G. Lindenmayr, “Thermally enhanced field emission from a laser-illuminated tungsten tip: temperature rise of tip,” *J. Appl. Phys.*, vol. 51, no. 9, p. 4996, 1980.
- [73] M. J. G. Lee and E. S. Robins, “Thermal relaxation of a laser illuminated field emitter,” *J. Appl. Phys.*, vol. 65, no. 4, pp. 1699–1706, 1989.
- [74] B. M. Klein and D. A. Papaconstantopoulos, “Electron-phonon interaction and superconductivity in transition metals and transition-metal carbides,” *Phys. Rev. Lett.*, vol. 32, pp. 1193–1195, 1974.

- [75] W. S. Fann, R. Storz, H. W. K. Tom, and J. Bokor, “Direct measurement of nonequilibrium electron-energy distributions in subpicosecond laser-heated gold films,” *Phys. Rev. Lett.*, vol. 68, no. 18, 1992.
- [76] R. Kienberger, E. Goulielmakis, M. Uiberacker, A. Baltuska, V. Yakovlev, F. Bammer, A. Scrinzi, T. Westerwalbesloh, U. Kleineberg, U. Heinzmann, M. Drescher, and F. Krausz, “Atomic transient recorder,” *Nature*, vol. 427, pp. 817–821, 2004.
- [77] D. M. S. Johnson, J. M. Hogan, S.-W. Chiow, and M. A. Kasevich, “Picosecond optical switching using RF nonlinear transmission lines,” *J. Lightwave Technol.*, vol. 29, pp. 666–669, Mar 2011.
- [78] M. van der Heijden, “Energy spread measurement of the nano-aperture ion source,” Master’s thesis, Delft University of Technology, 2011.
- [79] W. Zhang, T. Li, M. Lours, S. Seidelin, G. Santarelli, and Y. Coq, “Amplitude to phase conversion of InGaAs PIN photo-diodes for femtosecond lasers microwave signal generation,” *Applied Physics B*, vol. 106, no. 2, pp. 301–308, 2012.
- [80] J. J. McFerran, E. N. Ivanov, A. Bartels, G. Wilpers, C. W. Oates, S. did-dams, and L. Hollberg, “Low-noise synthesis of microwave signals from an optical source,” *Electronics Letters*, vol. 41, pp. 650–651, 2005.
- [81] P. Pasmans, G. van den Ham, S. D. Conte, S. van der Geer, and O. Luiten, “Microwave TM010 cavities as versatile 4D electron optical elements,” *Ultramicroscopy*, vol. 127, no. 0, pp. 19–24, 2013.
- [82] J. D. Jackson, *Classical Electrodynamics*, 3rd ed., ch. 8, pp. 368–371. John Wiley & Sons, Ltd., 1999.
- [83] J. J. Barroso, P. J. Castro, J. P. Leite Neto, and O. D. Aguiar, “Analysis and simulation of reentrant cylindrical cavities,” *Int. J. Infrared Milli.*, vol. 26, pp. 1071–1083, 2005.
- [84] using the software package Comsol version 4.1, Comsol AB, Sweden, 2010.

- [85] using the software package Comsol version 4.3a, Comsol AB, Sweden, 2012.
- [86] C. T. Hebeisen, G. Sciaiani, M. Harb, R. Ernstorfer, T. Dartigalongue, S. Kruglik, and R. J. D. Miller, “Grating enhanced ponderomotive scattering for visualization and full characterization of femtosecond electron pulses,” *Opt. Express*, vol. 16, no. 5, 2008.
- [87] F. J. García de Abajo and M. Kociak, “Electron energy-gain spectroscopy,” *New Journal of Physics*, vol. 10, no. 7, p. 073035, 2008.
- [88] B. Barwick, D. J. Flannigan, and A. H. Zewail, “Photon-induced near-field electron microscopy,” *Nature*, vol. 462, pp. 902–906, 2009.
- [89] M. Bosman, V. J. Keast, M. Watanabe, A. I. Maaroof, and M. B. Cortie, “Mapping surface plasmons at the nanometre scale with an electron beam,” *Nanotechnology*, vol. 18, no. 16, p. 165505, 2007.
- [90] S. T. Park, M. Lin, and A. H. Zewail, “Photon-induced near-field electron microscopy (PINEM): theoretical and experimental,” *New Journal of Physics*, vol. 12, no. 12, p. 123028, 2010.
- [91] E. Sugata and S. Tamaki, “Field ion microscopic research of flashing effect on tungsten and molybdenum tip cathodes before and after field-evaporation,” *J. Electron Microsc. (Tokyo)*, vol. 21, no. 1, pp. 13–21, 1972.
- [92] H. S. Kim, M. L. Yu, U. Staufer, L. P. Muray, D. P. Kern, and T. H. P. Chang, “Oxygen processed field emission tips for microcolumn applications,” *Journal of Vacuum Science Technology B*, vol. 11, no. 6, pp. 2327–2331, 1993. Proceedings of the 16th international symposium on electron, ion, and photon beams.
- [93] F. J. García de Abajo, “Optical excitations in electron microscopy,” *Rev. Mod. Phys.*, vol. 82, no. 1, pp. 209–275, 2010.